# *DEVELOPMENT OF A MULTISCALE TWO-FLUID APPROACH WITH APPLICATION TO DROPLET DYNAMICS*

*Thesis submitted for the fulfilment of the requirements*

*for the Degree of Doctor of Philosophy*

*by*


***Georgia Nykteri***

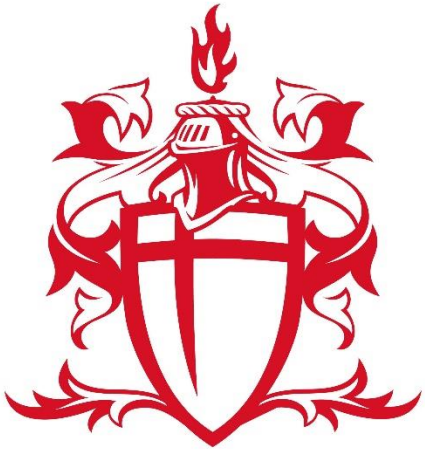

*CITY, UNIVERSITY OF LONDON*

*School of Mathematics, Computer Science & Engineering*

*Department of Mechanical Engineering & Aeronautics*


*July 2021*

*"'Ο,τι επιθυμείς να το φωνάζεις δυνατά...*

*Δεν ταιριάζει η μετριότητα με τη λαχτάρα"*

*Ν. Καζαντζάκης*

# ACKNOWLEDGEMENTS

Reaching the end of my PhD journey, I would like to thank all the people that helped and supported me during these years.

Firstly, I would like to thank my supervisor, Prof Manolis Gavaises, for always believing in me and my efforts through this journey and for giving me the opportunity to conduct this interesting research by adapting my project towards novel applications. With his vision and guidance, I had the unique opportunity to get involved into exciting scientific projects, to challenge myself in new environments, and collaborate with exceptional researchers from international universities.

Secondly, I would like to thank my second supervisor, Dr Phoevos Koukouvinis, for his help during the development of my solver. With his remarkable experience in CFD, he always had valuable comments for the progress of my work.

Additionally, I would like to thank each and every colleague of the A306 office. During my PhD years, many people started working in our group, others visited for a few months, others left. I will always keep in my memories all these great moments we all spent together, in the office, in the pub, in the conferences. You all made my PhD experience more special.

My PhD years in London were truly unforgettable for me thanks to my close friends Homa, Konstantina, Giovanni, and Daniel. I would like to thank them for always being by my side during the happiest and more stressful moments of this journey. London wouldn't have meant the same to me if I haven't met these beautiful people.

Finally, I would like to thank my beloved family for always supporting me even in my craziest dreams. My parents, Dimitris and Tonia, my brother Vasilis and my grandmother Georgia are always my inspiration and my safest place. Special thanks to Raymond for everything; nothing would have been the same without him.

Georgia Nykteri

Athens, July 2021

# ABSTRACT

The present thesis introduces a novel numerical methodology for multiscale flows with application to complex droplet fragmentation cases. The proposed methodology concerns a compressible two-fluid model developed in OpenFOAM® and provides the flexibility of dealing with the multiscale character of flow fields: the interface scales greater than the grid size are resolved using the sharp interface (VOF) methodology, while the smaller ones, representing the diffused phase, are resolved by solving an additional transport equation of the generated surface area density ($\Sigma$) of the dispersed droplet cloud. The solver switches automatically between the sharp and the diffuse interface within the Eulerian-Eulerian framework in segregated and dispersed flow regions, respectively, by employing a dynamic interface sharpening based on a flow topology detection algorithm.

Validation cases against a two-fluid shock tube and a rising bubble depict the accuracy of the numerical methodology to deal with highly compressible flows and fast changing interfaces. Initially, the functionality of the multiscale framework is demonstrated for high-speed droplet impact cases with Weber numbers above $10^5$ and compared with new experimental data. At the investigated impact conditions, compressibility effects dominate the early stages of droplet splashing with shock waves to form and propagate inside the droplet and local Mach numbers up to 2.5 to be observed for the expelled surrounding gas outside the droplet. At the later stages of splashing, the dispersion of the dense cloud of fragments dominates and an insight into the fragments dynamics and the evolving sizes is presented. Subsequently, the droplet aerobreakup imposed by three different intensity shock waves, with Mach numbers of 1.21, 1.46 and 2.64, is investigated. The major features and physical mechanisms of breakup, including the incident shock wave dynamics and the vortices development, are accurately captured. Additionally, the dense mist development and the evolution of the underlying secondary droplets is examined under different post-shock conditions, based on the sub-grid scale modelling. Finally, the laser-induced fragmentation of a liquid droplet for different laser pulses that correspond to resulting droplet propulsion velocity values between 1.76m/s and 5.09m/s is investigated. Both the early- and later-time droplet dynamics are accurately captured and the influence of the laser energy on the droplet deformation and subsequent fragmentation is highlighted. The evolution of the produced fragments due to the rim breakup is quantified with respect to the different expansion rates and aerodynamic conditions.

# PRESENT CONTRIBUTION

The major contributions of the present thesis can be summarized in the following points:

- **Development of a multiscale framework**

The novel methodology employs the compressible Navier-Stokes equations of two interpenetrating fluid media using the two-fluid formulation and operates between two different interface formulations, namely the sharp and the diffuse interface approach. Within the sharp interface approach the examined interfaces are resolved by the local mesh resolution, while in the diffuse interface approach sub-grid scale modelling is applied for the unresolved flow structures, incorporating an additional transport equation for the interface surface area density ($\Sigma$). Additionally, the implemented flow topology detection algorithm allows for a physically consistent switching between the two interface formulations with respect to the local flow regimes.

- **Modelling of high-speed droplet impact**

The high-speed impact of a water droplet onto a solid wall with Weber numbers above $10^5$ is simulated for the first time in the literature using the developed multiscale framework and validated against new experimental data. Additionally, the multiscale framework allows for the consideration of all scales involved and the quantification of the produced fragments.

- **Modeling of droplet aerobreakup**

The aerodynamic breakup of a water-like droplet imposed by three different intensity shock waves, with Mach numbers of 1.21, 1.46 and 2.64, is investigated using the developed multiscale framework. The numerical simulations focused on the later-stages of fragmentation in which the produced dense mist dominates. Two stripping mechanisms are identified and analysed dependent on the Mach number. An insight into the flow development, the secondary droplet interactions, and the evolution of sizes inside the polydisperse mist is obtained for the first time in the literature.

- **Modelling of laser-induced droplet fragmentation**

The response of a liquid droplet to different laser pulses that correspond to subsequent droplet propulsion velocity values between 1.76m/s and 5.09m/s, is examined, using the developed multiscale framework. Both the early- and the late-time dynamics are simulated for the first time in the literature and the influence of the laser energy on the macroscopic deformation and expansion rate of the droplet is demonstrated in consistence with the experimental observations. The physical mechanisms that determine the fragments dynamics, including the effects of the surrounding air, are captured. For the first time in the literature, the evolution of the fragments and the sizes in the course of fragmentation are obtained based on the sub-grid scale analysis.

# DECLARATION

I hereby declare that the content of this dissertation is original and has not been submitted in whole or in part for consideration for any other degree or qualification in this, or any other university. This dissertation is my own work, except where specific reference is made to a joint effort in the text and acknowledged accordingly.

I grant powers of discretion to the University Librarian to allow the thesis to be copied in whole or in part without further reference to me. This permission covers only single copies made for study purposes, subject to normal conditions of acknowledgement.

Georgia Nykteri

Athens, July 2021

# TABLE OF CONTENTS

# LIST OF FIGURES

**Figure 3.13** Volume concentration of the dispersed region over the total volume of the water phase for a mesh resolution of 100 (red solid line) and 200 (blue solid line) cells per initial droplet diameter. The green vertical lines correspond to a decrease for the width of the deforming droplet by 10%, 25% and 50%.

**Figure 4.1** Separation of timescales in the laser-induced droplet rim fragmentation problem. (i) A nanosecond laser pulse impacts onto the left side of the dyed droplet. (ii) The vaporized liquid mass on the superficial layer is ejected backwards. As a result, the droplet accelerates until it reaches a constant propulsion velocity on the vapour expulsion time $\tau_e$. (iii) The droplet propels and deforms on the inertial time $\tau_i$. (iv) The surface tension and the extended fragmentation restrict the droplet lateral expansion on the capillary time $\tau_c$.

**Figure 4.2** Problem configuration and simulation set-up. (i) For $t < \tau_e$, the axisymmetric pressure pulse $p(\theta)$ is applied on the droplet surface. (ii) At $t = \tau e$, the initial pressure and velocity fields inside the droplet are obtained. (iii) The initial fields are mapped into the wedge geometry. For $t > \tau_e$, the droplet fragmentation is simulated using the multiscale two-fluid approach.

**Figure 4.3** Laser-induced droplet deformation and early-stage rim fragmentation at We=90 . Qualitative comparison of the droplet shape evolution for three different initialization sets, i.e. (i) $\tau_e$=1μs, $p_e$=4.26bar, (ii) $\tau_e$=0.8μs, $p_e$=5.32bar (iii) $\tau_e$=0.8μs, $p_e$=8.51bar, for the same propulsion velocity U=1.76m/s, as calculated from equation (4.10).

**Figure 4.4** Evolution of the laser-induced droplet deformation at We = 90, 170, 330, 460, 750. (i) Droplet radius expansion and (ii) droplet width reduction for three different initialization sets for each examined condition, i.e., different individual $p_e$, $\tau_e$ values for the same propulsion velocity, as calculated from equation (4.10).

**Figure 4.5** Laser-induced droplet rim fragmentation at We=330. (i) Comparison between the experimental visualizations of Klein et al. [6] in sideview and the isoline of the liquid volume fraction at $10^{-3}$, obtained with the multiscale two-fluid approach. (ii) 3D reconstructed results in sideview and 30$^o$ angle, using the multiscale two-fluid approach. The expanding liquid sheet is captured by the sharp interface formulation (in grey the isosurface for liquid volume fraction at 0.5) and the detached fragments are captured by the diffuse interface formulation (in red the isosurface for fragments larger than 0.09μm). Zoomed-in view for the dimensions of the produced fragments after the rim breakup . (iii) 3D reconstructed results in sideview and 30$^o$ angle, using the VOF method. Iso-surface of the liquid volume faction at 0.5.

**Figure 4.6** Laser-induced droplet rim fragmentation at We=330. (i) Experimental visualizations of Klein et al. [6] in front view. (ii) 3D reconstructed results in front view, using the multiscale two-fluid approach. The expanding liquid sheet, captured by the sharp interface formulation, is illustrated as the iso-surface of the liquid volume faction at 0.5 with a mesh resolution of 200 (left) and 250 (right) cells per initial droplet diameter. (iii) 3D reconstructed results in front view, using the VOF method. Iso-surface of the liquid volume faction at 0.5 with a mesh resolution of 200 cells per initial droplet diameter. The red circle defines the borders of the liquid sheet rim in the experimental results. The calculated thickness of the thin liquid sheet on the central line (in purple) and on the initial droplet radius (in yellow) is illustrated on the simulation results**.**

**Figure 4.7** Laser-induced droplet rim fragmentation at We=90. Initial pressure and velocity fields inside the droplet, obtained for U=1.76m/s and $\tau_e$=1μs. Liquid sheet expansion velocity in the lateral direction, radial velocity (top) and dimensions (bottom) of the detached fragments for three time-instances that correspond to a liquid sheet with thickness 50%, 20% and 10% of the initial droplet diameter. The air velocity field around the rim and the developed vortex are depicted on the side panels. The minimum captured thickness is illustrated at 0.83ms.

**Figure 4.8** Laser-induced droplet rim fragmentation at We=170. Initial pressure and velocity fields inside the droplet, obtained for U=2.42m/s and $\tau_e$=0.5μs. Liquid sheet expansion velocity in the lateral direction, radial velocity (top) and

dimensions (bottom) of the detached fragments for three time-instances that correspond to a liquid sheet with thickness 50%, 20% and 10% of the initial droplet diameter The air velocity field around the rim and the developed vortex are depicted on the side panels. The minimum captured thickness is illustrated at 0.6ms

**Figure 4.9** Laser-induced droplet rim fragmentation at We=330. Initial pressure and velocity fields inside the droplet, obtained for U=3.37m/s and $\tau_e$=0.3μs. Liquid sheet expansion velocity in the lateral direction, radial velocity (top) and dimensions (bottom) of the detached fragments for three time-instances that correspond to a liquid sheet with thickness 50%, 20% and 10% of the initial droplet diameter. The air velocity field around the rim and the developed vortex are depicted on the side panels. The minimum captured thickness is illustrated at 0.43ms.

**Figure 4.10** Laser-induced droplet rim fragmentation at We=750. Initial pressure and velocity fields inside the droplet, obtained for U=5.09m/s and $\tau_e$=0.2μs. Liquid sheet expansion velocity in the lateral direction, radial velocity (top) and dimensions (bottom) of the detached fragments for three time-instances that correspond to a liquid sheet with thickness 50%, 20% and 10% of the initial droplet diameter. The air velocity field around the rim and the developed vortex are depicted on the side panels. The minimum captured thickness is illustrated at 0.3ms. The arrows point to the minor low-pressure region and the very few created droplets after collapse.

**Figure 4.11** Expansion of the liquid sheet radius, as a result of the laser-induced droplet deformation at We = 90, 170, 330, 750. Comparisons between the experimental observations of Klein et al. [6], the analytical model of Villermaux & Bossa [7] and the simulation results using the VOF method and the multiscale two-fluid approach until a liquid sheet with thickness 10% of the initial droplet diameter is formed.

**Figure 4.12** Volume concentration of the dispersed region over the total volume of the liquid phase for the laser-induced droplet fragmentation at We = 90, 170, 330, 750.

**Figure 4.13** Droplets distribution inside the cloud of fragments at We=90. (i) Volume concentration of the fragments with diameters above 1 μm (in grey) and below 1 μm (in orange) over the total volume of the dispersed region. Probability density function of the fragments sizes for liquid sheet thickness (ii) 35% and (iii) 10% of the initial droplet diameter.

**Figure 4.14** Droplets distribution inside the cloud of fragments at We=170. (i) Volume concentration of the fragments with diameters above 1 μm (in grey) and below 1 μm (in orange) over the total volume of the dispersed region. Probability density function of the fragments sizes for liquid sheet thickness (ii) 35% and (iii) 10% of the initial droplet diameter.

**Figure 4.15** Droplets distribution inside the cloud of fragments at We=330. (i) Volume concentration of the fragments with diameters above 1 μm (in grey) and below 1 μm (in orange) over the total volume of the dispersed region. Probability density function of the fragments sizes for liquid sheet thickness (ii) 35% and (iii) 10% of the initial droplet diameter.

**Figure 4.16** Droplets distribution inside the cloud of fragments at We=750. (i) Volume concentration of the fragments with diameters above 1 μm (in grey) and below 1 μm (in orange) over the total volume of the dispersed region. Probability density function of the fragments sizes for liquid sheet thickness (ii) 35% and (iii) 10% of the initial droplet diameter.

# LIST OF TABLES

# NOMENCLATURE

Latin symbols

| | | | |
|---|---|---|---|
| A | surface area [$m^2$] | $u_r$ | relative velocity field [m/s] |
| $C_\alpha$ | interface compression coefficient | V | volume [$m^3$] |
| $C_D$ | drag coefficient | We | Weber number |
| $C_{SGS}$ | SGS mechanisms constant coefficient | $y^+$ | dimensionless wall distance |
| d | diameter [m] | | |
| e | specific internal energy [kJ/kg] | | |
| E | interfacial energy source term [W/m2] | | |
| $F_D$ | drag force [N] | | |
| $F_{D\alpha}$ | artificial drag force [N] | | |
| $F_s$ | surface tension force [N] | | |
| g | acceleration of gravity [$m/s^2$] | | |
| k | specific kinetic energy [kJ/kg] | | |
| M | interfacial momentum source term [Pa/m] | | |
| $M_s$ | shock wave Mach number | | |
| Oh | Ohnesorge number | | |
| p | pressure [Pa] | | |
| $\mathbf{q}^{\mathbf{eff}}$ | effective heat flux vector [W/m] | | |
| R | radius [m] | | |
| $R_{al}$ | turbulent liquid flux | | |
| $R_\Sigma$ | turbulent flux of interface surface area density | | |
| Re | Reynolds number | | |
| Sc | Schmidt number | | |
| T | temperature [K] | | |
| u | velocity field [m/s] | | |
| $u_c$ | artificial compression velocity field [m/s] | | |

Greek symbols

| | |
|---|---|
| $\alpha$ | volume fraction |
| $\Delta t$ | computational time step [s] |
| $\kappa$ | interface curvature [1/m] |
| $\lambda$ | wavelength [m] |
| $\mu$ | dynamic viscosity [Pa·s] |
| $\nu$ | kinematic viscosity [$m^2/s$] |
| $\nu_{topo}$ | topological parameter |
| $\rho$ | density [$kg/m^3$] |
| $\sigma$ | surface tension coefficient [$kg/s^2$] |
| $\Sigma$ | liquid gas interface surface area density [1/m] |
| $\Sigma^*$ | equilibrium liquid gas interface surface area density [1/m] |
| $\Sigma_{min}$ | minimum liquid gas interface surface area density [1/m] |
| $\boldsymbol{\tau}^{\mathbf{eff}}$ | effective stress tensor [Pa] |
| $\tau_r$ | artificial drag force relaxation factor |
| $\tau_{SGS}$ | SGS mechanisms timescale [s] |
| $\psi$ | compressibility [s/m] |

Subscripts

| | |
|---|---|
| 0 | initial condition |
| g | gaseous phase |
| l | liquid phase |
| m | liquid and gaseous mixture |
| SGS | sub-grid scale component |
| s | post-shock flow |
| t | turbulent component |

| | |
|---|---|
| 2D | Two-dimensional |
| 3D | Three-dimensional |
| AMR | Adaptive mesh refinement |
| BI | Boundary integral |
| CFD | Computational fluid dynamics |
| CFL | Courant–Friedrichs–Lewy number |
| DDM | Discrete droplet method |
| DNS | Direct numerical simulations |
| EUV | Extreme ultraviolet |
| MEK | Methyl-ethyl-ketone |
| RANS | Reynolds-averaged Navier–Stokes equations |
| RDF | Probability density function |
| RHS | Right-hand side |
| RTP | Rayleigh-Taylor piercing |
| SIE | Shear-induced entrainment |
| SPH | Smooth particle hydrodynamics |
| TBP | Tri-butyl phosphate |
| VOF | Volume of Fluid |

# 1 INTRODUCTION

In this chapter, the scientific background and the motivation for the present work are presented, along with the objectives and the outline of the thesis.

## 1.1 Background and Motivation

Droplet fragmentation is a fundamental multiscale problem that consists of the violent breakup of a large-scaled droplet into a polydisperse cloud of small-scaled fragments with a broad distribution of sizes. The widespread droplet fragmentation can be imposed by the breakup of previously formed ligaments or liquid sheets under the developed surface instabilities and the relative velocity between the liquid droplet and the surrounding air and additionally, by significant topological changes in the flow field, including the droplet interactions with solid surfaces, shock waves, laser pulses or other droplets [8]. Overall, fragmentation is found in multiple state-of-the-art technologies under various flow conditions. In the automotive industry, high-speed droplet impact [9] is observed inside the fuel combustion chamber of internal combustion engines, which influences the secondary fuel spray atomization and the resulting air-fuel mixture combustion, while in supersonic combustion (scramjet) engines the secondary liquid atomization is significantly affected by the shock wave induced breakup [10] of the produced secondary droplets under the underlying supersonic flow conditions. At the same time, the novel industry of semiconductors aims to the reduce the sizes of microchips using advanced manufacturing techniques, such as extreme ultraviolet (EUV) nanolithography [11], [12], which involves complex processes of laser-induced droplet fragmentation [13].

Focusing on the energy industry, despite the inevitable environmental cost and the non-infinite natural resources, oil is expected to remain the world's primary energy source up to 2040, meeting about one-third of global energy demand. In the transportation sector, oil will continue to cover about 95% of global energy needs [14], due to widespread availability, economic advances and high energy density. Global transportation energy demand is about to grow 25% between 2015 and 2040 with the demands in heavy-duty vehicles to have the largest growth in volume, while marine and aviation will face the largest percentage growth [14]. Given the increasing global energy demands, the challenge for the next decades is to provide the needed energy supplies and at the same time to reduce energy-related greenhouse emissions. Specifically, regarding the transportation sector, which is responsible for about 20% of global $CO_2$ emissions, heavy-duty trucks and buses already account for nearly a quarter of Europe's road transport $CO_2$ discharges with a trend to increase up to 10% until 2030, while globally their contribution in $CO_2$ emissions rises to almost 50%. In an attempt to reduce global $CO_2$ emissions in order to meet the goals set in the 2015 Paris climate agreement, the global emission standards for both light and heavy-duty vehicles are becoming more stringent over the years [15].

Key factor in achieving the demanding energy and environmental goals is the development of new technologies, aiming to more efficient engines and improved fuel economy for cars and commercial vehicles. Thanks to recent technical advances, the emissions from diesel engines have been reduced by around 99% and modern diesel cars emit about 98% less $NO_x$ comparing to vehicles of the early 1990s [16]. Current scientific research focuses on the development of advanced fuel injectors**,** which will operate under higher injection pressure, providing improved conditions for the atomization process, better air-fuel mixture and finally, an optimal combustion without formation of soot.

Aiming to the design of more efficient fuel injection systems, a deep understanding, and an accurate modelling of the complex multiscale, multiphase phenomena, taking place in the in-nozzle flow and further ahead in the spray formation and atomization region before combustion, is required. Due to the high complexity and the usually non-feasible computational cost, liquid fuel penetration and atomization have not been studied extensively over the years with most of the currently used numerical models being based on empirical correlations and experimental studies which have been held under non-realistic operating conditions [17], [18]. Therefore, there is a high demand in the industry for more accurate atomization models that can reveal all the complicated phenomena and flow features, being present under realistic operating conditions in order to improve the designed fuel injection systems.

HAoS ITN project focused on bridging the gap between up-to-date scientific knowledge and the industrial interests through the development of new experimental and numerical techniques to capture the complex phenomena during liquid spray atomization. Advanced combustion engines are operating under different fluid regimes in high pressures and temperatures during their operating cycle [19], introducing significant complexities in any modelling attempt of the atomization process. In the classical spray regime [19], governed by the classical theory of atomization mechanisms under subcritical conditions, surface tension forces play a significant role and a well-defined molecular interface is present to separate the liquid and gaseous phases. Based on morphological characteristics of a classical atomizing spray, two distinct spray regions have been identified. The primary atomization region, where under the action of surface tension and turbulence effects the initial liquid column breaks down and forms small ligaments, and the secondary atomization region, in which the dominant aerodynamic forces cause further break down of the formed ligaments into small droplets. The formation and breakup of a disintegrating liquid spray is influenced by numerous factors, like the thermo-physical states of both liquid and ambient gas, the nozzle geometry, the internal flow features, the turbulence at nozzle exit, the viscosity effects and the aerodynamic forces between liquid structures and gas, among others [20].

However, even within the classical spray regime, multiscale phenomena, involving a broad range of spatial and temporal scales, are dominant, influencing not only the atomizing liquid spray, but also the individual droplets forming inside the spray. Specifically, the secondary droplets inside the combustion chamber are subject to high velocities and extreme thermodynamic conditions, which are related to a vast range of complicated multiscale phenomena, including the mechanical impact of the produced secondary droplets onto the wall; all the underlying small-scale phenomena significantly affect the overall spray behaviour. Therefore, a thorough understanding of the liquid fuel atomization concerns the investigation of all the multiscale process, related with the secondary droplets inside the spray.

Similarly, the challenge of manufacturing more efficient scramjet engines involves the deep understanding of all the complex processes that influence the supersonic combustion. In the absence of a compressor, the supersonic conditions and the created shock waves are responsible for the incoming air flow compression, the effective air-fuel mixing before ignition and the subsequent combustion efficiency [21], [22]. Therefore, the quality of the produced air-fuel mixture is significantly influenced by the developed liquid fuel droplet dynamics, including the shock wave induced breakup and vaporization of large-scale liquid fuel droplets [23]; both processes result in the formation of smaller-scaled liquid fuel droplets that allow for a more

effective mixing with the supersonic air flow. Following the significantly demanding aerodynamic conditions and the formation of a polydisperse mist of secondary droplets with a vast range of scales involved, the numerical studies in the literature that investigated the droplet aerobreakup are restitched to incidence shock wave Mach numbers close to 1, see indicatively the works of [24] and [10]. Therefore, further research is required in order to reveal information about the produced structures inside the dense mist after the droplet aerobreakup, the interactions between the secondary droplets and the surrounding air and the final size distributions of the small-scaled droplets that characterize the air-fuel mixing properties.

Finally, focusing on the technological breakthrough in electronics, the exponentially increasing demand in faster access to information and higher storage capacity leads the semiconductors industry to invest in novel manufacturing technologies of microchips. As described by Moore's law [25], at modern times, the number of transistor integrated in a microchip per unit area grows exponentially in order to meet the rapidly increasing technological demand. Therefore, the semiconductor manufacturers focus on reducing the size of the microchip components by using state-of-the-art technology of EUV nanolithography [11], [12]. In the EUV nanolithography, the critical dimension, which defines the minimum size features that can be printed on a surface with the photolithography method, is reduced to nanoscales and the respective illumination wavelength is decreased to $\lambda$=13.5nm [26]. However, a complete redesign of the ordinary photolithography machines is required in order to apply the EUV nanolithography method. Therefore, the investigation of the parameters that affect the EUV light creation and absorption is necessary for the design of efficient EUV nanolithography equipment. Specifically, ASML designed a EUV light source, imposed by the plasma emission of a liquid tin droplet after the impact with a high-energy laser pulse [13]. Subsequently, the produced EUV radiation is directed to the target with a collection of mirrors. The laser-induced liquid droplet fragmentation, which initiates the nanolithography process, consists of complex physical mechanisms, which remain unrevealed due to the demanding high energy conditions that introduce significant complexities in the numerical modelling. As a result, the thorough investigation of the liquid droplet response to different laser energies can provide significant information for the design of efficient EUV nanolithography machines.

## 1.2 Objectives

The aim of the present thesis is to develop a physically consistent multiscale approach in order to accurately capture the uninvestigated droplet dynamics with a viable computational cost. Thus, the novel numerically methodology allows for the simulation of complicated flows and elucidate aspects and mechanisms that are not visible in the experiments due to limitation in the diagnostic method and at the same time, are not deeply investigated in the up-to-date numerical studies in the literature because of the significantly high computational cost of a full-scale analysis.

The main objectives of the present thesis are summarized as follows:

1. Develop a numerically stable multiscale framework based on the two-fluid approximation that solves the compressible N-S equations considering the slip velocity effects. The developed multiscale framework allows for a dynamic and physically consistent switching between the sharp and the diffuse interface approach based on the local flow topology. Within the sharp interface approach, the examined interfaces are resolved by the local mesh resolution, while in the diffuse interface approach sub-grid scale modelling is applied for the unresolved flow structures.

2. Implement the Σ-Y transport equation for the diffuse flow regions and utilize relations for the various terms; these include the sub-grid scale mechanisms of flow turbulence, droplet collision and coalescence and secondary breakup effects. The Σ-Y transport equation provides an insight into to the evolution and sizes of the unresolved sub-grid scale structures.

3. Demonstrate the applicability of the model to a wide range of conditions that addressed in the open literature for the first time and covering a wide range of applications:
   - the high-speed droplet impact onto a solid wall and predict the dynamics of the produced fragments; this is relevant to internal combustion engines.
   - the shock wave-imposed droplet aerodynamic breakup and predict the dynamics inside the produced dense mist; this is relevant to supersonic combustion (scramjet) engines.
   - the droplet response to a laser pulse impact and capture the evolution of the rim breakup; this is relevant to microchips manufacturing using the EUV nanolithography method.

## 1.3 Thesis Outline

The main body of the present thesis is organised, as described below:

*Chapter 2* introduces the developed multiscale two-fluid approach, the governing equations, and the implementation of the new numerical methodology in OpenFOAM®. Validation cases are provided. The advantages of the proposed multiscale two-fluid approach are demonstrated in a high-speed water droplet impact case and evaluated against new experimental data.

*Chapter 3* examines the aerodynamic breakup of a water-like droplet under high Mach and Weber numbers, using the developed multiscale two-fluid approach. The capabilities of the numerical methodology to capture dominant compressibility effects is displayed and information regarding the structures inside the produced cloud of fragments are revealed.

*Chapter 4* employs the developed multiscale two-fluid approach to simulate the laser-induced droplet fragmentation, dominated by the rim breakup. The numerical methodology captures the early- and later time droplet response to the laser energy. An insight into the produced fragments and the evolving flow field both inside the droplet and in the surrounding air is provided.

*Chapter 5* highlights the major conclusions of the present work and presents recommendations for future studies and applications.

*Chapter 6* summarizes the peer-review journal and conference proceedings publications produced from the present work.

# 2 HIGH-SPEED DROPLET IMPACT

In the present chapter, the newly developed numerical methodology for multiscale flows is presented. The methodology employs the compressible Navier-Stokes equations of two interpenetrating fluid media using the two-fluid formulation; this allows for compressibility and slip velocity effects to be considered. On-the-fly criteria switching between a sharp and a diffuse interface within the Eulerian-Eulerian framework along with dynamic interface sharpening is developed, based on an advanced local flow topology detection algorithm. The sharp interface regimes with dimensions larger than the grid size are resolved using the VOF method. For the dispersed flow regime, the methodology incorporates an additional transport equation for the surface-mass fraction (Σ-Y) for estimating the interface surface area between the two phases. To depict the advantages of the proposed multiscale two-fluid approach, a high-speed water droplet impact case has been examined and evaluated against new experimental data; these refer to a millimetre size droplet impacting a solid dry smooth surface at a velocity as high as 150m/s, which corresponds to a Weber number of $7.6\times10^5$.

---

*Published as:

G. Nykteri, P. Koukouvinis, R. S. Gonzalez Avila, C.-D. Ohl, and M. Gavaises, “A Σ-Y two-fluid model with dynamic local topology detection : Application to high-speed droplet impact,” *Journal of Computational. Physics*, vol. 408, p. 109225, 2020.

## 2.1 Introduction

Multiscale complexities are realised in numerous multiphase flow fields of both industrial and more theoretical interest due to the temporal and spatial geometric diversity of the flow patterns formed by the interacting phases. The different flow structures are characterized by a broad range of scales which as a result, impose the coexistence and dynamic transition between different flow regimes [27]. Examples from the plethora of multidisciplinary applications include fuel spray injection in internal combustion engines, droplet aerodynamic-induced breakup occurring in all type of liquid-fuel combustors [5], droplet splashing [9], bubble column bioreactors for chemical processes [28] and even the Rayleigh–Taylor instability in a supernova explosion [29]. With regards to the two-phase flow of a liquid and a gaseous phase, macroscales dominate the free surface regions, where the two phases are separated with a well-defined interface in the presence of a segregated regime [30], while flow regions with an intense fluid dispersity due to the dominance of fluid microparticles indicate a dispersed regime [30]. Adding to the complexities imposed by the scale heterogeneity of the flow field, the simultaneous presence of different regimes comes with additional limitations arising from the different physical factors influencing them; surface tension effects dominate the segregated flow, while aerodynamic forces play the dominant role in the dispersed flow regions. Thus, under the scope of a mathematical modelling, it remains challenging and computationally demanding to deal with such multiscale flow systems and simultaneously account for different scaled structures, governed by different physical scales that cannot be captured by the grid resolution available.

Several numerical approaches have been proposed in the literature over the years, regarding the modelling of multiphase flows in engineering applications. Among the most classic models is the Discrete Droplet Method (DDM), developed by Dukowicz [31], in which the dispersed phase is considered as a number of similar physical droplets within a stochastic Lagrangian framework; the conservation equations are solved for the Eulerian continuous phase. Even though the DDM method has been widely utilised in different applications (see selectively the numerical studies of Berlemont et al. [32], Boileau et al. [33] and Gorokhovski & Saveliev [34]), it is generally valid only when the liquid volume fraction is relatively small and the droplets are homogeneously distributed, introducing remarkable limitations in many simulations. In the context of an exclusively Eulerian approach, the homogeneous mixture model, proposed by Drew [35], is based on the assumption of a single velocity field for both the dispersed and the continuous phases. Due to the simple mathematical formulation and the computational feasibility in liquid fuel spray

injection applications under realistic geometries and operating conditions, as demonstrated in the numerical simulations of Koukouvinis et al. [36] and Pei et al. [37], the homogeneous mixture model has been implemented and extensively used in both open-source and commercial software. However, the deficiencies regarding the two-phase mixture assumption, the interface diffusivity, and the absence of physical sub-grid scale models, often restrict the physical consistency of the obtained results. Under a fully Eulerian formulation, the inhomogeneous mixture model, introduced by Ishii & Mishima [38], often referred to as the multifluid model, is another alternative approach in which each of the interpenetrating phases is considered separately with a different set of conservation equations; numerical modelling of the mass, momentum and energy exchange mechanisms is required for simulating the interactions between them. Nevertheless, the Eulerian-Eulerian approach provides more accurate results mainly under highly dispersed conditions away from regimes where a dispersed phase cannot be distinguished, as highlighted by Rusche [39].

In an attempt to overcome the limitations of the previous models and improve the accuracy of multiphase flow simulations, Direct Numerical Simulations (DNS), which correspond to a full-scale analysis of the local variable topology without any assumptions or additional numerical models introduced, are the optimum numerical tool. However, very few DNS or unresolved-DNS studies can be found in the literature (selectively the numerical studies of Rossinelli et al. [40], Gorokhovski & Herrmann [41], Hermann [42] and Shinjo & Umemura [43], [44]), particularly for industrial applications; this is due to the prohibitive computational cost with the current computational capabilities. Focusing specifically on improving the representation of the liquid gas interface, several interface capturing and interface tracking methods have been proposed with the volume of fluid (VOF) method [45], [46], the level-set method [47], [48], the ghost-fluid method [49] and the front-tracking method [50], [51] to be commonly used. A sharp interface approach can be applicable in segregated flows, where large-scale flow features are dominant, and the local interfacial structures can be well resolved under the requirement of a sufficiently fine computational mesh. Thus, an interface sharpening formulation in dispersed flow regions with occurring micro- or even nanoparticles is not computationally feasible.

Recently, more advanced numerical models have been developed in order to overcome the dependency on local flow regimes in specific multiphase flow applications. The ELSA model, introduced by Vallet et al. [52], is based on the principles of the Σ-Y model, developed by Vallet and Borghi [53], which was initially proposed for simulating the flame surface area evolution in combustion simulations in the study of Marble & Broadwell [54]; it provides a dynamic transition

between a Eulerian and a Lagrangian framework in the primary and secondary liquid spray atomization regions, respectively. The additional transport equation for the liquid gas interface surface area density (Σ) allows for representation of unresolvable sub-grid scale structures with a viable computational cost, ought to the physical modelling of the mechanisms responsible for the interface surface area density formation, as discussed in detail in the study of Lebas et al. [55]. Several variations and improvements of the original ELSA model have been proposed so far, including vaporisation [55] and slip-velocity effects [56], as well as a sharp interface formulation in the Eulerian part of an atomizing spray [57]. A further insight into the sub-grid scale phenomena can be gained with the implementation of a probability density function (PDF) so as to obtain secondary droplet size distributions and other stochastic properties of the dilute spray using the Method of Moments, developed by Marchisio et al. [58]. In one of the most recent formulations presented by Navarro-Martinez [59], a joint sub-grid scale volume surface PDF is introduced for the liquid surface and volume dependence to predict in more detail the interface surface area density production and destruction at sub-grid level within the ELSA model [52]. With respect to commercial CFD codes, a complete atomization model for liquid fuel spray simulations has been integrated in AVL FIRE® [60], using a fully Eulerian formulation. The interacting phases are resolved with the incorporation of a specific number of Eulerian droplet classes, which share the same properties, as demonstrated by Vujanović et al. [61]. Moreover, in the recent versions of OpenFOAM®, a hybrid fully Eulerian incompressible solver has been implemented, namely multiphaseEulerFoam [62] and used in multiscale vertical plunging jets in the work of Shonibare & Wardle [63], supporting a dynamic switching between a diffuse and a sharp interface approach within the same multifluid framework. However, the advantages of the state-of-the-art numerical models over the more classic approaches are restricted to the needs of the specific applications for which they were developed. Therefore, there is a gap in the literature for a holistic numerical approach, which can be applicable in any flow field governed by a multiscale character and complex physical phenomena, including high compressibility and slip velocity effects, regardless of the limitations of local flow characteristics.

The above methodologies can be applied to the case of a droplet impacting on solid surfaces, which represents a fundamental multiscale flow problem, that still attracts the scientific interest, due to its relevance in many engineering applications, such as cooling, coating, inkjet printing, fuel injection in internal combustion engines, as it is stated in the review works of Kandlikar & Bapat [64] and Moreira et al. [9]. The droplet deformation and potential fragmentation after impact is very sensitive to several parameters regarding the impact and target conditions; namely

the impact velocity, the droplet initial diameter and physical properties, target wettability, roughness and surface temperature, as it has been investigated in numerous experimental studies (see selectively the experiments of Pan et al. [65], Visser et al. [66], Antonini et al. [67], Roisman et al. [68] and Liang & Mudawar [69]). The post-impact outcomes are subject to different regimes, ranging from spreading or even sticking on the surface to rebounding and splashing and they have been comprehensively presented in the literature by Rein [70], Yarin [71] and Josserand & Thoroddsen [72] and illustrated on regime maps as a function of dimensionless impact parameters by Ma et al. [73] and Bertola et al. [74]. Several correlations to define the splashing regime threshold have been established by Yarin & Weiss [75] and Range & Feuillebois [76], while the most widely used criterion for the transition between the deposition and splashing regimes under large impact velocities is the parameter of Mundo [77], which is based on the Weber and Ohnesorge numbers. Additionally, conducted experimental studies have been utilised for the development of empirical models, corresponding to the droplet post-impact characteristics under the influence of different impact regimes, as it is thoroughly described in the review work of Cossali et al. [78], in order to provide numerical models for spray impingement simulations.

Even though the single droplet impact onto solid surfaces has been extensively investigated with experimental studies of Worthington [79] since 1877, the mechanisms of the prompt and violent splashing under high impact velocities, which correspond to the massive spatial dispersion of the produced secondary droplets far away from the solid surface and the dominance of compressibility phenomena with strong propagating shock waves inside the deforming droplet, have not been precisely revealed yet. Due to the limitation of the high speeds and small structures involved, recent advancements in imaging technologies by Thoroddsen et al. [80] have contributed to the performance of new experiments under higher impact velocities. In the experiments of Xu et al. [81], the corona splashing of an ethanol droplet on a dry and smooth surface with impact Weber number equal to 1685 was examined; the created lamella reached a maximum spreading velocity of 30m/s. In the study of Visser et al. [82], experiments with water microdroplets have been conducted, impacting on both hydrophilic and hydrophobic surfaces with velocities up to 50m/s and Weber numbers that do not exceed the value of 1770. However, despite the high-speed conditions, no splash but only spreading of the droplet on the surface was observed, due to the influence of the surrounding air. One of the few and most recent experiments in which a prompt splashing was illustrated is the work of Thoroddsen et al. [83], in which a water droplet was subject to an impact with a smooth and solid surface at Weber numbers up to 2480, followed by the creation of water microdroplets with maximum spreading velocity of 100m/s.

Finally, in the study of Field et al. [84], an experiment of high-speed droplet impact at 110m/s was performed, with emphasis put on capturing the propagating shock wave inside the droplet at the early stages of the impact with the target, without examining the later splashing effects. Thus, it is noticeable from the literature that high-speed droplet impact experiments are limited; available studies do not exceed Weber number values of 2500 and they mainly focus on the early stages of the droplet and wall interaction.

Regarding the numerical investigation of droplet impact cases, most recent studies examine the impact on solid surfaces under the spreading, as examined by Malgarinos et al. [85] and Visser et al. [82] or the corona splashing regimes, demonstrated in the numerical simulations of Guo et al. [86] and Wu & Cao [87]; they utilise an interface capturing method for the conducted simulations. With the VOF method to be the most commonly used approach, the droplet deformation and spreading on the target can be captured in detail with a sufficiently fine mesh. However, in the case of higher impact velocities, which result to splashing and fragmentation of the droplet into secondary microscale structures, the performed simulations are restricted to the early stages of the phenomena, since the later stages of droplet fragmentation are dominated by computationally prohibitive scales for a VOF simulation. Thus, a more advanced numerical modelling is required to deal simultaneously with the early and later stages of the splashing droplet evolution. Moreover, other studies, conducted by Haller et al. [88], Niu & Wang [89], Kyriazis et al. [90] and Wu et al. [91], perform high-speed droplet impact simulations with the focus on capturing the occurring compressibility phenomena, namely the strong shock waves inside the droplet and the produced cavitation regions, which are formed and dominate during the early stages of the impact, excluding in this manner the secondary droplet dispersion from the scope of their numerical investigation.

Following the limitations of the currently used numerical methodologies in multiscale flow applications, the present study proposes a new numerical framework which has been developed in OpenFOAM®, utilising the two-fluid formulation [38]; this allows for both compressibility and slip velocity effects to be taken into account. The model solves for an additional transport equation for the interface surface area density; the previously developed Σ-Y model [53] for incompressible flows is coupled here for the first time with a compressible two-fluid framework. This provides significant information for the unresolved sub-grid scale phenomena, which are related to the interface formation during the flow development. The Σ-Y two-fluid model is also combined with a dynamic switching between the sharp and the diffuse interface approaches that co-exist during the numerical solution at different parts of the computational domain. Thus, it is

possible to deal simultaneously with the segregated and the dispersed flow regions; the two-fluid model formulation has been coupled with the VOF method to operate under the segregated flow regime. The dynamic switching is performed with an advanced topology detection algorithm relative to criteria available in the literature [57], [62]. However, apart from the numerical limitations of the VOF and the diffuse interface approaches with respect to the computational mesh, which correspond to the commonly used switching criteria, the proposed flow topology detection algorithm also evaluates the local flow characteristics. The developed methodology is initially validated against a shock tube problem in §2.3.1 and a rising bubble in §2.3.2. Following, validation is performed against the challenging case of a high-speed droplet impact in §2.3.3, using new experimental data obtained specifically for this case. These refer to impact Weber number of the order of $10^5$, which is much higher than the available up-to-date literature. Finally, emphasis from the numerical perspective is given on providing an insight into the dispersed regions of the flow field at the later stages of the droplet fragmentation evolution, where even the experimental investigation cannot contribute with sufficient information due to limitations in diagnostic methods for high Mach number flows consisting of a large number of droplets with sizes less than 1μm.

## 2.2 Multiscale Two-Fluid Approach

The Σ-Y two-fluid model with dynamic local topology detection has been implemented in OpenFOAM® with further developments on twoPhaseEulerFoam solver, an available compressible Eulerian pressure-based solver. In principle, the numerical model consists of the same set of governing equations for both multiscale formulations, namely the sharp and the diffuse interface approach, with specific source terms to be activated and deactivated depending on the currently operating formulation of the solver, as it is described in detail below.

### 2.2.1 Two-Fluid Model Governing Equations

In the context of a two-fluid approach, as introduced by Ishii & Mishima [38], the volume averaged conservation equations governing the balance of mass, momentum and energy are solved separately for each phase k:

$$\frac{\partial}{\partial t}(a_k\rho_k) + \nabla\cdot(a_k\rho_k u_k) = 0 \tag{2.1}$$

$$\frac{\partial}{\partial t}(a_k\rho_k u_k) + \nabla\cdot(a_k\rho_k u_k u_k) = -a_k\nabla p + \nabla\cdot\left(a_k\boldsymbol{\tau}_k^{eff}\right) + a_k\rho_k g + \sum_{\substack{n=1\\ n\neq k}}^{2} M_{kn} \tag{2.2}$$

$$\frac{\partial}{\partial t}[a_k\rho_k(e_k+k_k)]+\nabla\cdot[a_k\rho_k(e_k+k_k)u_k]=-\nabla\cdot\left(a_k\boldsymbol{q}_k^{eff}\right)-\left[\frac{\partial a_k}{\partial t}p+\nabla\cdot(a_k u_k p)\right] \quad (2.3)$$

$$+a_k\rho_k g\cdot u_k+\sum_{\substack{n=1\\n\neq k}}^{2}E_{kn}$$

The numerical method is based on a finite-volume framework, using an implicit pressure-based solver for the governing equations of the two-fluid model. Numerical coupling for the independent systems of conservation equations is achieved through additional source terms added to the Navier-Stokes equations, which appear after the imposed averaging procedure. These source terms account for the mass, momentum, and energy exchange phenomena by providing suitable closure relations for the macroscopic interfacial interactions occurring in a transient multiphase flow system. Specifically, the interfacial momentum source term $M_{kn}$ represents the forces acting on the dispersed phase and depends on local topology, since different forces are dominant under different flow regimes. The interfacial energy source term $E_{kn}$ demonstrates the heat transfer between the phases that can be modelled via a standard heat transfer law. The interfacial mass source term, which is responsible for the mass transfer due to phase-change effects or other interfacial phenomena that result to production or destruction of the interface, such as sub-grid scale turbulence and droplet interactions, is not implemented in the continuity equations as expected. Instead, in the present work the mass exchange contributions with an effect on interface formation are considered in the transport equation for the liquid gas interface surface area density. Phase-change phenomena, like vaporisation and cavitation, are neglected since they are negligible in the examined high-speed droplet impact case at the early stages of impact, where temperature variation around the standard conditions is not significant and local pressure drop is not sufficient to cause remarkable cavitation regions, as it has been stated before in the literature for similar impact conditions in the studies of Niu & Wang [89] and Kyriazis et al. [90].

Viscous and turbulence effects are introduced in the model with the effective stress tensor $\boldsymbol{\tau}^{\text{eff}}$ in the momentum equations and the effective heat flux vector $\mathbf{q}^{\text{eff}}$ in the energy equations; $\boldsymbol{\tau}^{\text{eff}}$ accounts for the molecular viscosity and the Reynolds stress tensor, which based on Boussinesq's hypothesis [92] relates turbulent velocity fluctuations to the eddy viscosity; $\mathbf{q}^{\text{eff}}$ corresponds to the laminar and turbulent thermal diffusivity. For the turbulent components, appropriate models are implemented within either a RANS or an LES framework in OpenFOAM®; LES modelling is used for the turbulent flow cases in the present study with the implementation of the one-equation SGS model of Lahey [93]. Given the occurring Reynolds numbers, a dimensionless wall distance $y^+$ with a value lower than 1 is observed; thus, the appropriate turbulent wall functions are implemented for capturing the near-wall phenomena; the two-layer wall function is used

which is a blending between the logarithmic and the linear laws for the turbulent and viscous sublayers, respectively.

Finally, the thermodynamic closure of the system is achieved by solving independently an individual equation of state for each phase from which the corresponding density field is obtained. In the following simulations, the ideal gas equation of state is used for the gaseous phase and the stiffened gas equation of state, proposed by Ivings et al. [94], has been implemented and used for the liquid phase. The stiffened gas equation of state is basically the same as the ideal gas equation of state with an additional pre-pressurization term to match the density and stiffness of the liquid. Despite its deficiencies, it is commonly used in the fundamental flow investigations of Saurel et al. [1] and in highly violent phenomena, studied by Beig et al. [95]; moreover, it is known to be valid for the pressure and temperature conditions examined in the present simulations.

*Σ-Y Model Transport Equations*

The liquid dispersion in a liquid and gaseous flow is simulated with the liquid phase volume fraction transport equation, which represents the volume proportion of liquid at a given volume in the computational domain. The transport equation for the liquid volume fraction in a compressible two-phase flow is:

$$\frac{\partial a_l}{\partial t} + \nabla \cdot (a_l u_m) + v_{topo}[\nabla \cdot (a_l(1-a_l)u_c)] = a_l a_g \left(\frac{\psi_g}{\rho_g} - \frac{\psi_l}{\rho_l}\right)\frac{Dp}{Dt} + a_l \nabla \cdot u_m - (1 - v_{topo})R_{a_l} \quad (2.4)$$

where the topological parameter $\nu_{topo}$ distinguishes the two different interface approaches by taking either the 0 or 1 value under a diffuse or sharp interface formulation, respectively. $u_c$ is the artificial compression velocity, defined by Deshpande et al. [96], that is introduced along the interface as a countereffect of the inevitable numerical diffusion in order to maintain interface sharpness in flow regions subject to a segregated regime. The turbulent liquid flux $R_{\alpha l}$ on the RHS of the transport equation, as modelled by Vallet et al. [52], accounts for the liquid dispersion induced by turbulent velocity fluctuations, which is important in dispersed flows and smaller scales. Additionally, since a compressible flow is involved, the gradients of liquid density that are related to compressibility effects on the liquid volume fraction are taken into consideration and equation (2.4) takes the formed described by Jadidi et al. [97].

The liquid gas interface surface area density, namely the surface area of the liquid gas interface per unit of volume, provides supplementary information regarding the interface formation without the assumption of a particular shape in the produced flow features. The transport equation for the liquid gas interface surface area density, as defined by Lebas et al. [55], is described as follows:

$$\frac{\partial \Sigma'}{\partial t} + \nabla(\Sigma' u_m) = (1 - v_{topo})\left[-R_\Sigma + C_{SGS}\frac{\Sigma}{\tau_{SGS}}\left(1 - \frac{\Sigma}{\Sigma^*_{SGS}}\right)\right] \quad (2.5)$$

The turbulent flux of the interface surface area density $R_\Sigma$, namely the first source term on the RHS of the transport equation, represents the surface area diffusion due to turbulent velocity fluctuations. The second source term on the RHS accounts for all physical mechanisms which fall below the computational mesh resolution and are responsible for the surface area production and destruction. In sharp interface regions with dominant large scale features the evolution of the interface surface area is captured directly by the computational model and grid. On the contrary, in highly diluted and dispersed flows, the interface production and destruction at sub-grid level significantly affects the overall interface formation; thus, appropriate modelling is required to obtain this sub-grid scale information. Under the assumption of a minimum interface surface area due to simultaneous existence of liquid and gas on the interface, Chesnel et al. [98] defined the total interface surface area density as follows:

$$\Sigma = \Sigma' + \Sigma_{min} \quad (2.6)$$

where $\Sigma_{min}$ is the minimum interface surface area density that can be found within a control volume for a given liquid volume fraction value with $0<\alpha_l<1$, which imposes the presence of two phases and thus, the presence of an interface in the examined control volume. Based on empirical correlations obtained from CDNS studies and under the assumption of a spherical droplet inside the examined computational cell, the minimum interface surface area density is defined by Chesnel et al. [98] as $\Sigma_{min} = 2.4\sqrt{a_l(1-a_l)}V_{sphere}^{-1/3}$.

## 2.2.2 Sharp Interface Approach

Interface sharpening is implemented in OpenFOAM® with the MULES algorithm [96], an iterative technique which guarantees boundness of the volume fraction and sharpness at the interface by modifying the advection term in the transport equation for the volume fraction. In this manner, an additional advection term is introduced which acts as an artificial compression in order to maintain sharpness without the need for interface reconstruction. This approach has been implemented within the proposed multiscale two-fluid framework and thus, in the segregated flow regions the transport equation for the liquid volume fraction takes the final form of equation (2.4) with the topological parameter $v_{topo}$ set to 1. Then, the artificial compression velocity $u_c$ is given by the expression:

$$u_c = C_a|u_m|\frac{\nabla a_l}{|\nabla a_l|} \quad (2.7)$$

with $C_\alpha$ the interface compression parameter that takes values equal or greater than 1 so as to increase the imposed interface sharpness. In the following simulations the typical value of $C_\alpha$=1 has been implemented so as to introduce interface sharpness with the MULES algorithm.

However, the introduction of an interface sharpening approach within a two-fluid framework requires further modifications in the numerical model. In the limit of a sharp interface, the velocities on either side of the interface must be equal in order to eliminate the relative velocity and meet the no-slip interface condition. At the same time, a fundamental principle of the two-fluid model is the presence of separate velocity fields for the two interpenetrating liquids. Several studies in the literature, such as the studies of Černe et al. [99], Wardle & Weller [62] and Strubelj & Tiselj [100], are dealing with the coupling of a two-fluid model and an interface sharpening method by implementing an additional source term in the momentum equations. This extra term practically imposes large interfacial drag values; as a result, the relative velocity on the interface is eliminated and finally the coupling between the two-fluid model and the sharp interface approach is stabilized. In the present model, the source term introduced in the momentum equations (2) has an expression similar to the aerodynamic drag force, introduced by Strubelj & Tiselj [100], and enforces instantaneous equalizing of the velocities near the resolved interface. The artificial drag force is defined as:

$$F_{Da} = v_{topo}\, F(u_r) \frac{\tau_r}{\Delta t} \tag{2.8}$$

where $F(u_r)$ is an expression proportional to the relative velocity $u_r$ between the two phases and the density of the two-fluid mixture $\rho_m$ with $F(u_r) = a_l(1 - a_l)u_r\rho_m$, as proposed by Strubelj & Tiselj [100], $\Delta t$ the computational time step and $\tau_r$ a relaxation factor which needs to be calibrated correspondingly, in order to meet the no-slip interface condition. As it is described in detail in §2.3.2, the elimination of the interfacial relative velocity, which practically results to a stronger coupling between the two-fluid model and the sharp interface approach, is achieved by maximizing the relaxation factor $\tau_r$. In an attempt to avoid any case-dependent calibration of $\tau_r$, an on-the-fly algorithm has been developed which gradually increases the value of $\tau_r$ starting from the value of 1, until the point that the tangential component of the relative velocity on the interface reaches a sufficiently low lower-bound close to zero; under this condition, the no-slip interface condition is satisfied. In practice, a numerical criterion is examined on the interface, which requires for the tangential component of the relative velocity to be only a small proportion of the total local relative velocity, approaching a zero value.

Under a segregated flow regime, the surface tension plays a greater role against the aerodynamic forces. Therefore, its contribution should be taken into consideration and a surface tension force is added as a source term in the momentum equations (2.2). The surface tension force is defined by the Continuum Surface Force (CSF) of Brackbill et al. [101] as follows:

$$F_s = v_{topo}\,\sigma\kappa\frac{\nabla\rho}{[\rho]}\frac{\rho}{\langle\rho\rangle} \tag{2.9}$$

where σ is the surface tension coefficient, κ the interface curvature, [ρ] the density jump described as $[\rho]=\rho_g-\rho_l$ and <ρ> the density at the interface given by $\langle\rho\rangle=\frac{1}{2}(\rho_l+\rho_g)$ in order to replace the local discontinuity with a smooth variation.

Regarding the interface density, all sub-grid scale phenomena, which are modelled via source terms in equation (2.5), are out of the scope of a sharp interface approach and thus, the RHS of the transport equation is set to zero. Besides, a basic principle of the multiscale formulation is the accurate topological distinction between different flow regimes and the imposition of a sharp interface approach in regions where all present flow features can be resolved by the utilized grid resolution.

## 2.2.3 Diffuse Interface Approach

Under a dispersed flow regime with prevailing small, dispersed structures, the aerodynamic forces and particularly the drag force acting on the dispersed phase is the dominant factor in interfacial momentum exchange between the liquid and gaseous phases. Different drag models are implemented by Marschall [102] depending on local flow conditions, i.e. dispersed droplets in continuous gas or dispersed bubbles in continuous liquid. The drag force, which is introduced as the interfacial momentum source term in momentum equations (2.2), is described as:

$$F_D = (1 - v_{topo})\frac{1}{2}C_D\rho_{continuous}u_r|u_r|A_{particle} \tag{2.10}$$

where $\rho_{coninuous}$ is the density of the phase, which is considered continuous and $A_{particle}$ is the projected area of a typical dispersed particle. For the estimation of the drag coefficient $C_D$, there are many empirical models in the literature, for instance the drag models of Schiller & Naumann [103], Ishii & Zuber [104] and Tomiyama & Shimada [105], depending on properties of the flow field and the discrete particle characteristics. In the present work, where the focus is mainly on the motion of very small droplets in highly dispersed flows with low or moderate Reynolds numbers, the drag coefficient is obtained from the model of Rodi and Fueyo [106]:

$$C_D = \begin{cases} \frac{16}{Re}, & Re < 1.5 \\ \frac{14.9}{Re^{0.78}}, & 1.5 < Re \leq 80 \\ \frac{49.9}{Re}\left(1 - \frac{2.21}{Re^{0.5}}\right) + 1.17 \times 10^{-8} Re^{2.615}, & 80 < Re \leq 1530 \\ 2.61, & Re > 1530 \end{cases} \quad (2.11)$$

However, since many semi-empirical correlations are involved, the closure relations of the interfacial source terms are usually the main cause for the uncertainties of the two-fluid model. In an attempt to reduce the possible inaccuracies, in the proposed numerical model the interface surface area is obtained from the transport equation for the interface surface area density, which is used to calculate a characteristic length corresponding to the flow structures in each computational cell. More specifically, the diameter of a spherical particle, which has the same volume to surface area ratio as the examined computational cell volume to the calculated interface surface area density, is used as the equivalent dispersed particle diameter in drag force calculations. Then, the interface surface area density diameter is defined by Chesnel et al. [98] as follows:

$$d_\Sigma = \frac{6a_l(1-a_l)}{\Sigma} \quad (2.12)$$

Concerning the transport equation for the liquid volume fraction, the diffuse interface approach results to exclusion of the interface compression term; consideration of the sub-grid turbulent fluctuations, as it appears in equation (2.4) with the topological parameter $v_{topo}$, is set to 0. The turbulent liquid flux $R_{\alpha l}$ on the RHS of the transport equation represents stochastic liquid dispersion phenomena due to the occurring turbulence, as modelled by Vallet et al. [52]. Previous studies on modelling $R_{\alpha l}$, conducted by Demoulin et al. [107] and Andreini et al. [56], depict a relation between the statistically dependent turbulent velocity fluctuations and the averaged local relative velocity, which corresponds to a correlation between slip and drift velocities of the mean flow field, as presented below:

$$R_{a_l} = -\nabla \cdot \left(a_l'' \widetilde{\rho_l''} u_m''\right) = -\nabla \cdot [a_l(1-a_l)\rho_l V_r] = -\nabla \cdot [a_l(1-a_l)\rho_l(u_r - V_D)] \quad (2.13)$$

where $V_r$ is the local relative velocity, $u_r$ the slip velocity and $V_D$ the drift velocity. The slip velocity contribution to the turbulent liquid flux can be calculated directly without the need of modelling due to the two-fluid formulation. As for the drift velocity effects, they are modelled via a first order closure by García-Oliver et al. [108], i.e. a classic gradient law using the turbulent properties of the liquid and gaseous mixture is implemented.

A significant advantage of the proposed multiscale two-fluid formulation is the coupling with the transport equation for the interface surface area density. Especially within the framework of a

diffuse interface approach, where the interface is neither tracked nor resolved by the grid resolution, this additional information provides an insight into the interface surface area density evolution in space and time even in the sub-grid scales. Examining the source terms on the RHS of equation (2.5), which are activated under the dispersed regime, the turbulent flux of the interface surface area density $R_\Sigma$ accounts for its dispersion due to turbulence. Analogous to the turbulent liquid flux $R_{\alpha l}$ on the RHS of equation (2.4), $R_\Sigma$ is a turbulent diffusion term. Then, with respect to the closure of the turbulent liquid flux $R_{\alpha l}$ in equation (2.13), the turbulent diffusion flux $R_\Sigma$ is modelled accordingly, as suggested by Andreini et al. [56], as follows:

$$R_\Sigma = -\nabla \cdot \left(\widetilde{\Sigma' u_m''}\right) = -\nabla \cdot [\Sigma\, a_l(1-a_l)(u_r - V_D)] \tag{2.14}$$

The last term on the RHS of equation (2.5) represents the sub-grid scale mass exchange phenomena between the liquid and gaseous phases, which have been neglected from the continuity equations (2.1) and are related to the interface surface area density production and destruction. Different physical mechanisms with an effect on interface formation are included and described by their characteristic time scale $\tau_{SGS}$, the critical interface surface area density $\Sigma^*_{SGS}$ at an equilibrium state between production and destruction of the interface and an adjustable constant coefficient $C_{SGS}$ set to 1 in the presented cases. In the proposed model, the contributions of turbulent flow stretching and wrinkling particularly in dense flow regions, the droplet collision and coalescence effects, as well as the secondary breakup effects of produced droplets are taken into account with the appropriate closure relations proposed by Lebas et al. [55], which are summarized in Table 2.1.

**Table 2.1** Closure relations for the SGS terms in equation (2.5) related to interface surface formation.

| **SGS mechanism** | $\tau_{SGS}$ | $\Sigma^*_{SGS}$ |
|---|---|---|
| turbulence | $\frac{k}{\varepsilon}$ | $\frac{\alpha_l(1-\alpha_l)\rho_m k_m}{\sigma We^*_{turb}}$ with $We^*_{turb} = 1$ at equilibrium |
| collision and coalescence | $\frac{1}{\Sigma\sqrt{\frac{2}{3}k_m}}$ | $\frac{6\alpha_l(1-\alpha_l)}{d^*_\Sigma}$ with $d^*_\Sigma = d_\Sigma \frac{1+\frac{We^N_{coll}}{6}}{1+\frac{We_{coll}}{6}}$<br>• critical We for coalescence: $We^N_{coll} = 12$<br>• relevant We for collision: $We_{coll} = \frac{4\alpha_l(1-\alpha_l)\rho_l k_m}{\sigma\Sigma}$ |
| secondary breakup | $f(We_{BU})\frac{d_\Sigma}{u_r}\sqrt{\frac{\rho_l}{\rho_g}}$<br>with $We_{BU} = \frac{6\rho_g u_r^2 \alpha_l(1-\alpha_l)}{\sigma\Sigma}$ | $\frac{6\rho_g u_r^2 \alpha_l(1-\alpha_l)}{\sigma We^*_{BU}}$<br>with $We^*_{BU} = 12(1+1.077Oh^{1.6}) \cong 12$ for Oh << |

## 2.2.4 Flow Topology Detection Algorithm

A key factor for the accurate functioning of the multiscale formulation is the implementation of a stable topology detection methodology. The developed algorithm can detect instantaneous topological changes in flow regimes, evaluate the most appropriate numerical treatment for local interfaces and allow for a flexible two-way switching between sharp and diffuse interface approaches. The switching criteria, described in detail below, are applied exclusively in interfacial flow regions as in single phase regions a sharp interface is defined by default.

### 2.2.4.1 Switching criterion from sharp to diffuse interface approach

In any computational cell under the sharp interface approach, a diameter of an equivalent spherical structure based on the curvature of the interface can be calculated based on Shonibare & Wardle [63] as follows:

$$d_{curv} = \frac{2}{\kappa} \tag{2.15}$$

Assuming that at least 3 computational cells are needed for the grid resolution to capture any spherical structure with sufficient sharpness, as suggested by Shonibare & Wardle [63], the following geometric criterion can be proposed as the limit for the sharp interface approach:

$$d_{curv} < 3 * max\,(d_{cell}) \tag{2.16}$$

Nevertheless, this geometric criterion can only be considered as an indication for a potential switch to a diffuse interface approach. All computational cells which meet criterion (2.16) are subject to a second stage of topological examination based on the condition of their neighbour cells. The three different possibilities are as follows:

- A single cell which is supposed to follow a diffuse interface approach based on the geometric criterion but belongs to a strictly segregated region with sharp interfaces, will remain unaffected by changes, as shown in Figure 2.1(a).

- When a cell is part of a topologically unstable region, where all its neighbour cells previously respected a sharp interface approach but now some of them are also subject to changes, then as depicted in Figure 2.1(b), an expanded region is examined. Specifically, the surrounding area of the neighbour cells which are of particular interest is evaluated with regards to the occurring topological conditions. Finally, if the examined cell belongs to a highly transitional region, then the topological criterion is met and a change for the interface approach is applied.

- As illustrated in Figure 2.1(c), any cell that is in the border of transition between segregated and highly dispersed flow regimes will follow the tendency of local interface formation and will be subject to the diffuse interface approach in the following time step.

### 2.2.4.2 Switching criterion from diffuse to sharp interface approach

The reset of a sharp interface approach for a previously diffuse cell is performed after meeting a single geometric criterion, which correlates the interface surface area density diameter from equation (2.12) to the local computational mesh resolution. When the calculated diameter $d_\Sigma$ is larger than the cell size, then the presumed dispersed flow features can no longer be treated as mesh unresolvable structures and a switch to a sharpened interface state is required.

$$d_\Sigma > min\,(d_{cell}) \tag{2.17}$$

Since the overall concept of the diffuse interface approach is inextricably linked to sub-grid scale structures, the described geometric criterion is sufficient for changing the interface formulation without examining the surrounding flow conditions, as shown in Figure 2.1(d).

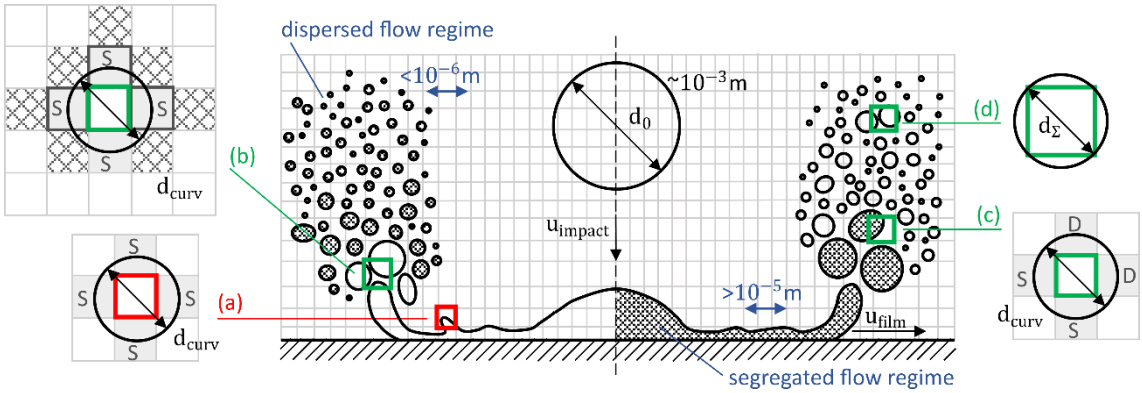


**Figure 2.1** Local topology detection and distinction criteria between the segregated and the dispersed flow regimes in order to impose the appropriate interface approach in each time step. Application in the multiscale flow of a droplet impact on a rigid wall with indicative dominant scales under each flow regime.

# 2.3 Results and Discussion

## 2.3.1 Two-Phase Shock Tube Problem

Initially, the capability of the proposed compressible two-fluid model to accurately capture the wave dynamics under high density ratios between the interacting phases is examined against the benchmark case of a two-phase shock tube. A one-dimensional 1m long two-fluid shock tube without mass transfer and initial discontinuity at x=0.75m, as studied by Saurel et al. [1], is used for validation. The left part of the shock tube is occupied by liquid dodecane at high pressure $p_l=10^8$Pa and density $\rho_l=500$kg/m$^3$, while the right part is set at atmospheric conditions with the occurring vapour dodecane at density $\rho_v=2$kg/m$^3$. The simulation is performed using the twoPhaseEulerFoam solver in a uniform computational grid of 1000, 10000 and 20000 cells with second order spatial accuracy and an adaptive time step to meet the convective Courant–Friedrichs–Lewy (CFL) number of 0.2. As a matter of consistency between the conducted simulation and the results of Saurel et al. [1], using the hyperbolic two-fluid model with two temperature and entropy fields but a single pressure and velocity field, the stiffened gas equation of state with the exact parameters utilised in the simulations of Saurel et al. [1] has been implemented in OpenFOAM® and applied for the thermodynamic closure. In Figure 2.2, the results obtained from the proposed two-fluid approach and the model of Saurel et al. [1] are compared with the exact solution at 473μs after the initial contact discontinuity was removed. The involved convectional waves, namely the left-facing rarefaction wave propagating through the liquid dodecane, the moving from left to right contact discontinuity and the right-facing shock wave propagating though the vapour dodecane are accurately captured with the proposed two-fluid model. Moreover, the increase in mesh resolution eliminates the numerical diffusion in the pressure and mixture velocity fields and the illustrated results using the finest mesh converge to a satisfactory agreement with the exact solution of the shock tube problem.

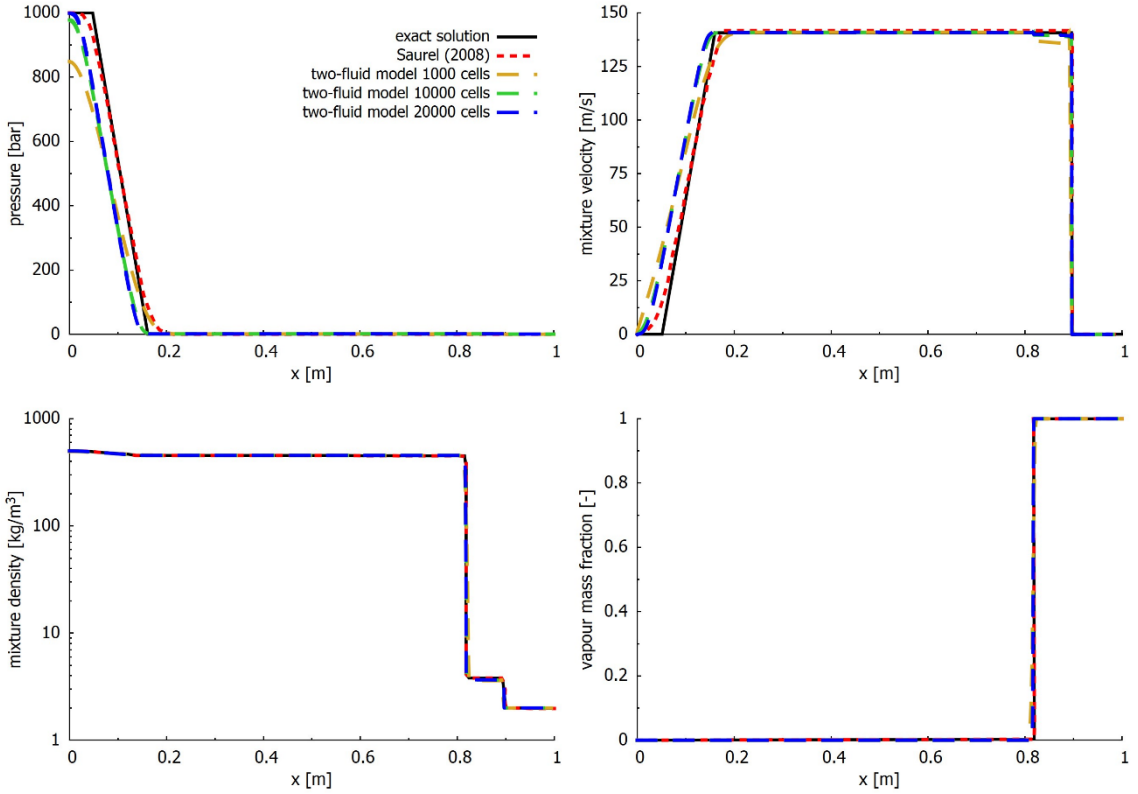


**Figure 2.2** Dodecane liquid–vapour shock tube problem. Pressure, mixture velocity, mixture density and vapour dodecane mass fraction fields at 473μs after the initial contact discontinuity was removed. Comparisons between the exact solution and the numerical solutions of Saurel et al. [1] and the two-fluid model with different mesh resolutions.

## 2.3.2 Rising Bubble

The effective coupling between the two-fluid model and the implemented sharp interface method is evaluated against the behaviour of a rising bubble in a quiescent viscous liquid under the influence of the gravitational force. The dynamic deformation of a single rising bubble in a liquid column has been extensively examined with experimental studies (see selectively the studies of Clift et al. [109], Bhaga & Weber [110] and Tomiyama et al. [111], among many others). Thus, the obtained bubble shape diagram, also known as the Grace diagram [109], depicts comprehensively a regime classification based on the final bubble shape and its terminal velocity as a function of dimensionless numbers. From a numerical perspective, a rising bubble simulation is commonly used to validate interfacial flow solvers, due to the high variety of interface deformation patterns under slightly modified flow conditions. For this purpose, in the absence of any analytical solution, Hysing et al. [2] performed a two-dimensional numerical benchmark configuration with different codes and established a reference solution for two numerical cases of

different density and viscosity ratios between the gas bubble and the surrounding liquid. A numerical benchmark case of an initially circular gas bubble rising in an initially stagnant liquid with liquid density 1000kg/m$^3$, liquid dynamic viscosity 10Pa·s and both density and viscosity ratios equal to 10, as proposed by Hysing [2] is used here for validation of the developed method. The gravity in the system g=-0.98m/s$^2$ and the surface tension between the two fluids σ=24.5N/m. Under these conditions, which correspond to intermediate Reynolds and Eotvos numbers with values 35 and 10, respectively, a moderate shape deformation is expected with a final bubble unbroken ellipsoidal shape based on the Grace diagram [109]. The two-dimensional simulation was conducted with the initial configuration and boundary conditions of Figure 2.3 in a uniform computational mesh of 320×640 cells.

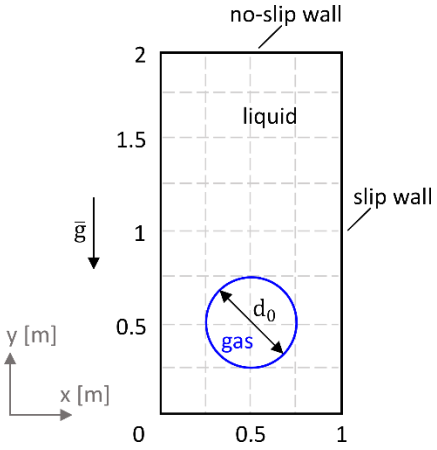


**Figure 2.3** Initial configuration and boundary conditions for a two-dimensional circular gas bubble rising in a liquid column.

The rising bubble shape is presented in Figure 2.4 in three successive time instances and under the effect of different relaxation factor $\tau_r$ values, which appears in the artificial drag force of equation (2.8), as a case-dependent parameter to regulate an efficient coupling between the two-fluid model and the sharp interface approach. Focusing on the macroscopic evolution of the two-dimensional bubble interface, it is observed that the circular bubble is gradually deformed to an ellipsoid shape, due to the counteraction of gravitational and surface tension forces. Under the occurring ellipsoid regime, surface tension is dominant and mainly responsible for the evolution of a moderate bubble deformation without breakup of the interface, as previously discussed in the study of Clift et al. [109]. As it is also depicted in Figure 2.4, a stronger coupling between the two-fluid model and the sharp interface approach is achieved by maximizing the relaxation factor, corresponding to the elimination of the interfacial relative velocity. This numerical trick practically overcomes the two-fluid principle of the mathematical model, which imposes different

velocity fields for each phase and approaches a standard sharp interface formulation, in which the two phases share a single momentum equation and respect the no-slip condition on the interface. Additionally, an increase of the relaxation factor, apart from the gradual elimination of the gas liquid relative velocity on the interface, has an apparent effect on the macroscopic bubble shape development.

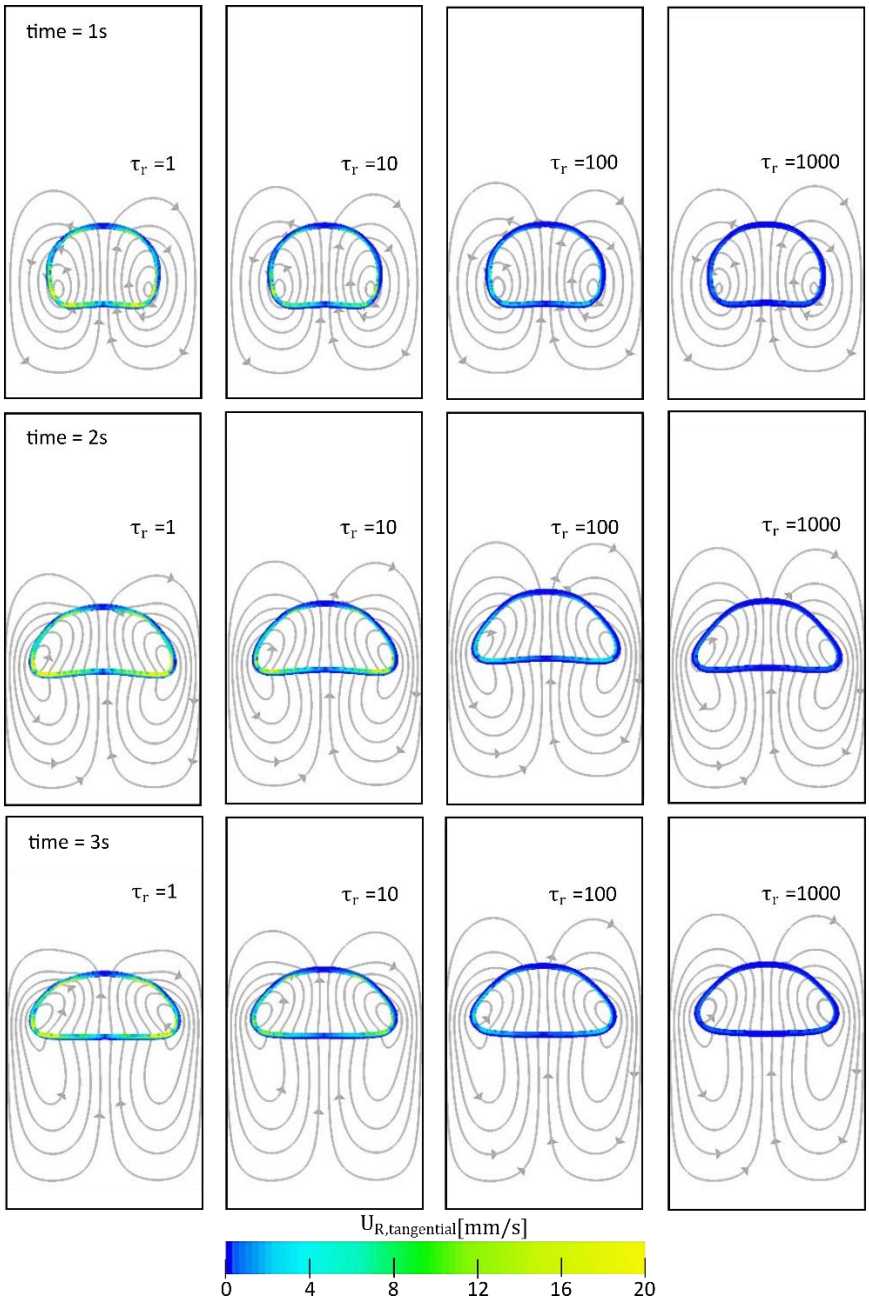


**Figure 2.4** Tangential relative velocity distribution on the interface of a rising bubble and gas liquid mixture velocity vectors at successive times under the effect of different relaxation factors $\tau_r$.

However, the case-dependent calibration of $\tau_r$ has been avoided with the implementation of an on-the-fly algorithm, which evaluates the interfacial region and gradually increases the value of $\tau_r$, until the point that the tangential component of the relative velocity on the interface reaches a defined lower-bound close to zero. More specifically, in each iteration of the pressure correction the computational cells in the interfacial regions are evaluated to meet the no-slip condition. The criterion used relates the tangential component of the relative velocity on the interface with its total local value and sets a sufficiently low lower-bound, as follows:

$$|u_{r,tangential}| < 10^{-5}|u_r|$$

In the case that the above condition is not satisfied, the $\tau_r$ value is increased starting from the value of 1 for each interfacial cell in each new time step of the pressure correction algorithm. In order to avoid significant jumps on the drag force values and to improve the performance with reduction of the computation cost, a smoothing of the $\tau_r$ values in the neighbour cells is performed. A demonstration of the algorithm with different local values for $\tau_r$ with respect to the no-slip interface condition is illustrated in Figure 2.5 for the rising bubble. The maximum values for $\tau_r$ are observed on the sides of the rising bubble, where also peaks in the relative velocity are observed due to the vertical motion of the bubble in the surrounding liquid.

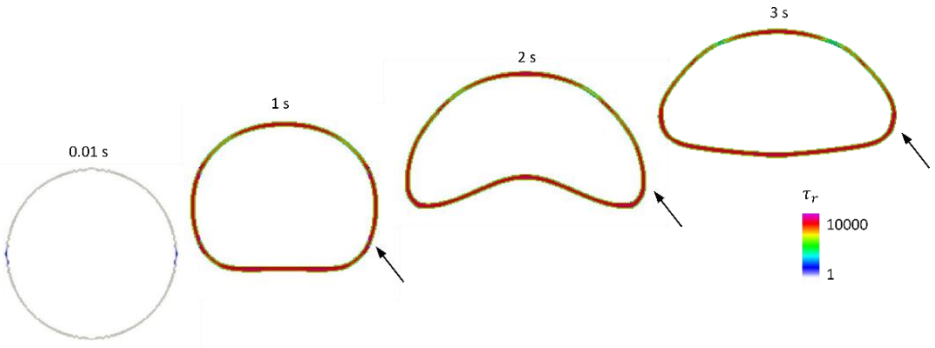


**Figure 2.5** Relaxation factors $\tau_r$ calculated on the interface of the rising bubble with the on-the-fly algorithm for meeting the no-slip interfacial condition.

In the scope of a rigorous quantitative analysis, the mass centre position, the mean rise velocity, and the deformed bubble circularity obtained with different relaxation factor values are examined in Figure 2.6. The computed benchmark quantities are compared with the reference solution of Hysing et al. [2] and the results presented by Štrubelj et al. [3], using a similar concept of coupling the two-fluid model with an interface sharpening approach; in this case, a conservative level-set method has been utilised. Hereby, it is verified that a stronger coupling with the implementation of maximum value for the relaxation factor ensures that the evolution of the rising bubble will

reach the expected behaviour. Specifically, the final position of the bubble centre of mass with the optimum relaxation factor $\tau_r$=1000 is at 1.055m and differs 1.22% from the results of Štrubelj et al. [3]. Furthermore, the maximum rise velocity is observed at 0.92s and with a value of 0.239m/s deviates by 2.58% from the solution of Štrubelj et al. [3]. Regarding the bubble shape deformation, the minimum circularity value occurs at 1.98s, approximately 0.1s later than in the study of Štrubelj et al. [3]; however, with respect to the tendency of circularity evolution in time the quantitative error is 1.7%. Finally, the shape of the rising bubble at its final position at 3s, as calculated with both the minimum and maximum relaxation factor values, shows the significant effect of an effective coupling between the two-fluid model and the sharpened interface approach on the bubble shape development with regards to the results in the literature [2], [3]. The results obtained from the on-the-fly algorithm also meet a satisfactory agreement with the reference solution and show that the use of the proposed automatic algorithm for calibrating on-the-fly the relaxation factor $\tau_r$ is a good compromise to avoid any arbitrary case-dependent calibration and the significantly increased computational cost, when the artificial drag force is maximised in the whole interfacial region with an effect on the converge of the pressure correction algorithm.

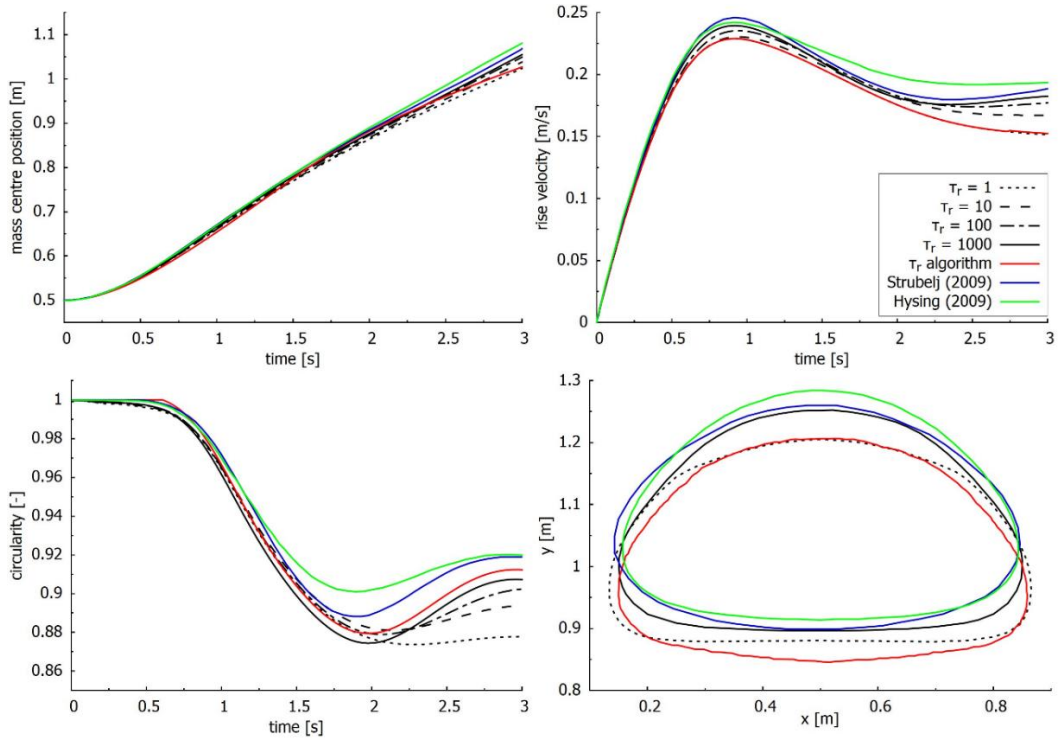


**Figure 2.6** Bubble benchmark quantities, i.e., mass centre position, rise velocity and circularity, evolution in time under the effect of different relaxation factors $\tau_r$. Bubble shape at its final position at 3s computed with minimum and maximum $\tau_r$ values. Comparisons with the reference solution of Hysing et al. [2] and the results of Štrubelj et al. [3].

## 2.3.3 High-Speed Droplet Impact

### 2.3.3.1 Experimental Set-up

In order to validate the multiscale approach developed, new experiments have been performed for a droplet impact onto a solid surface. The experiments have been conducted at the University of Magdeburg and concern a water droplet impact onto a high-speed moving target in three different cases summarized in Table 2.2. The deionized water droplet is slightly deformed to an ellipsoid shape, due to the acoustic field which keeps it levitated; the droplet is hit by the flat and smooth moving target, propelled from an initial distance of 2.35m away from the levitating droplet. The experiments were performed at room temperature 21$^{o}$C and atmospheric pressure conditions; the surface tension between the water droplet and the surrounding air is equal to 0.072N/m. The high-speed impact velocities of 120, 150 and 200m/s correspond to significantly high Weber and Reynolds numbers both of the order of $10^5$ to $10^6$, as calculated for the droplet properties at impact conditions. The rapid droplet splashing, and the subsequent violent fragmentation of the produced secondary structures were visualized with the use of a high-speed camera of 5 million frames per second and a spatial resolution of 50μm per pixel; recording of video started when the moving target was approximately 3.17mm away from the droplet.

**Table 2.2** Impact conditions for the examined experimental cases of high-speed droplet impact on a moving target.

| case | $d_x$ [mm] | $d_y$ [mm] | $u_{imp}$ [m/s] | target | We [-] | Re [-] | Oh [-] |
|---|---|---|---|---|---|---|---|
| 1 | 2.017 | 1.55 | 120 | teflon | $3.6\times10^5$ | $2.2\times10^5$ | $7.6\times10^{-3}$ |
| 2 | 2.65 | 2.2 | 150 | teflon | $7.6\times10^5$ | $3.7\times10^5$ | $5.5\times10^{-3}$ |
| 3 | 2.14 | 1.796 | 200 | acrylic | $1.1\times10^6$ | $4.2\times10^6$ | $6.9\times10^{-3}$ |

### 2.3.3.2 Simulation Results

For the numerical simulations of high-speed droplet fragmentation, the problem is set up in a different but corresponding manner with the water droplet moving with the impact velocity towards a rigid wall target. The simulations were performed in a 3D wedge geometry with one cell thickness, using a computational mesh of 412,500 cells; the details are described in Figure 2.7. For the purpose of a grid dependency investigation regarding the multiscale model functionality, two additional computational meshes have been used with twice coarser and twice finer resolution compared to the original mesh in the region around the droplet and wall interaction, illustrated as zone I in Figure 2.7. At the initial time step the moving droplet is set 0.9mm away from the rigid wall. Apart from the liquid phase velocity field, which is initialized

with the initial velocity of the moving droplet, the air velocity field is also initialized from a developed field obtained with the impact velocity set as an inlet in the right patch of the computational domain. Using this configuration, the effect of the moving target on the surrounding air in the original experimental set-up is adequately represented in the conducted simulations. The liquid gas interface surface area density is initialized on the droplet interface as the surface area of an ellipsoid with the dimensions of the examined water droplet, which corresponds to a 5º wedge per unit of the local computational cell volume. On the wall, the no-slip boundary condition is applied for the velocity fields, while a Neumann boundary condition is satisfied for the other computed flow fields.

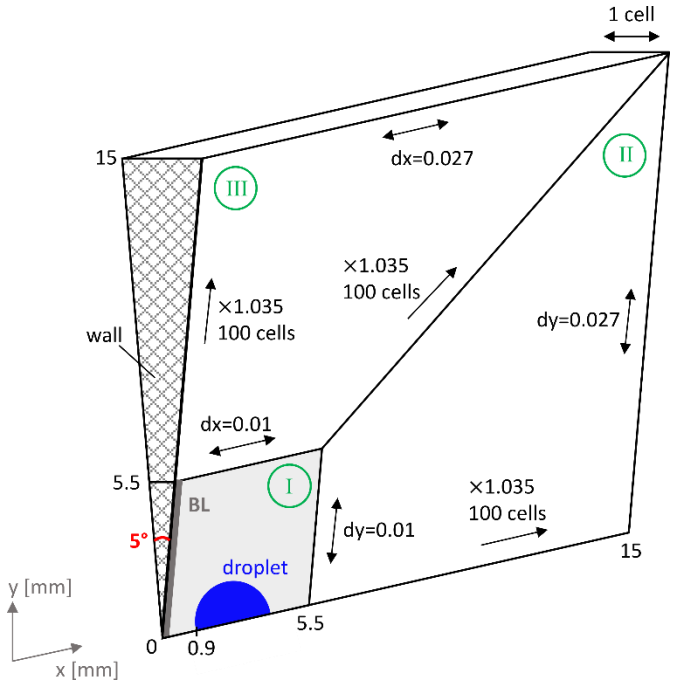


**Figure 2.7** Initial configuration and information regarding the computational mesh for the simulation of high-speed droplet impact on a rigid wall.

The spatial discretization used is based on second order linear discretization schemes, limited towards a bounded first order upwind scheme in regions of rapidly changing gradients. Time stepping is performed adaptively during the simulation, so as to respect the selected limit for the convective Courant–Friedrichs–Lewy (CFL) condition of 0.4. Even though the turbulent state corresponds to fully 3D-developed phenomena, the evolution of the droplet fragmentation under the examined impact conditions is found to be significantly quicker compared to the turbulence timescales. Therefore, the configuration of Figure 2.7, which is utilised in the performed

simulations, is an acceptable compromise between the accuracy of the numerical model and a viable computational cost.

The simulations conducted were based on the assumption that the liquid phase is the only present dispersed phase, interpenetrating and interacting with the continuous air phase. Under the high-speed impact conditions corresponding to very high Weber numbers ranging from $10^5$ to $10^6$, the droplet impact on the wall and the imposed prompt splashing will evolve rapidly; thus, contact angle boundary conditions are not explicitly defined and a zero gradient boundary condition for the water volume fraction on the wall is imposed, as previously applied in the simulations of Kyriazis et al. [90]. With regards to phase-change phenomena, vaporisation plays a minor role at the early stages of impact, since the temperature variations around the room conditions are not significant in comparison to the other physical phenomena that take place, as depicted by Kyriazis et al. [90]. Specifically, in the present simulations the local water temperature does not increase more than 20K at the moment of impact, when the strong shock wave is formed inside the droplet and the maximum local pressure of about $10^8$Pa is observed. On the contrary, cavitation is produced inside the droplet due to the influence of strong compressibility effects; however, in this particular case its influence is negligible compared to other dominant physical phenomena and it is not taken into consideration in the numerical modelling, as it is analysed in detail in the following paragraphs.

The evolution of the droplet fragmentation at 2, 4 and 6μs after the impact on the target are presented in Figures 2.8, 2.9 and 2.10, respectively, as it has been captured by the experimental study and the performed simulations with the proposed multiscale two-fluid model under the three different impact conditions of Table 2.2. In the numerical investigation, the widespread and highly dispersed water cloud produced after the prompt splashing of the droplet is subject to the diffuse interface formulation of the multiscale two-fluid model, shown as a grey iso-surface in the results. Therefore, the dominant sub-grid scale structures are modelled accordingly within the dispersed flow regime formulation of the numerical model and the interface surface area density diameters are calculated and used in the drag force calculations. Despite the vast spectrum of scales involved, the macroscopic characteristics of the successive stages of the droplet fragmentation are adequately predicted by the performed simulations, with the corresponding results to depict the radially expanding water cloud. In cases 1 and 2, which correspond to Weber numbers at impact conditions of the order of $10^5$, a similar evolution of the phenomenon is observed with an expected more rapid water dispersion under the impact velocity of 150m/s. On the contrary, in case 3 the increase in the Weber number of the order of $10^6$ results to a significantly violent droplet

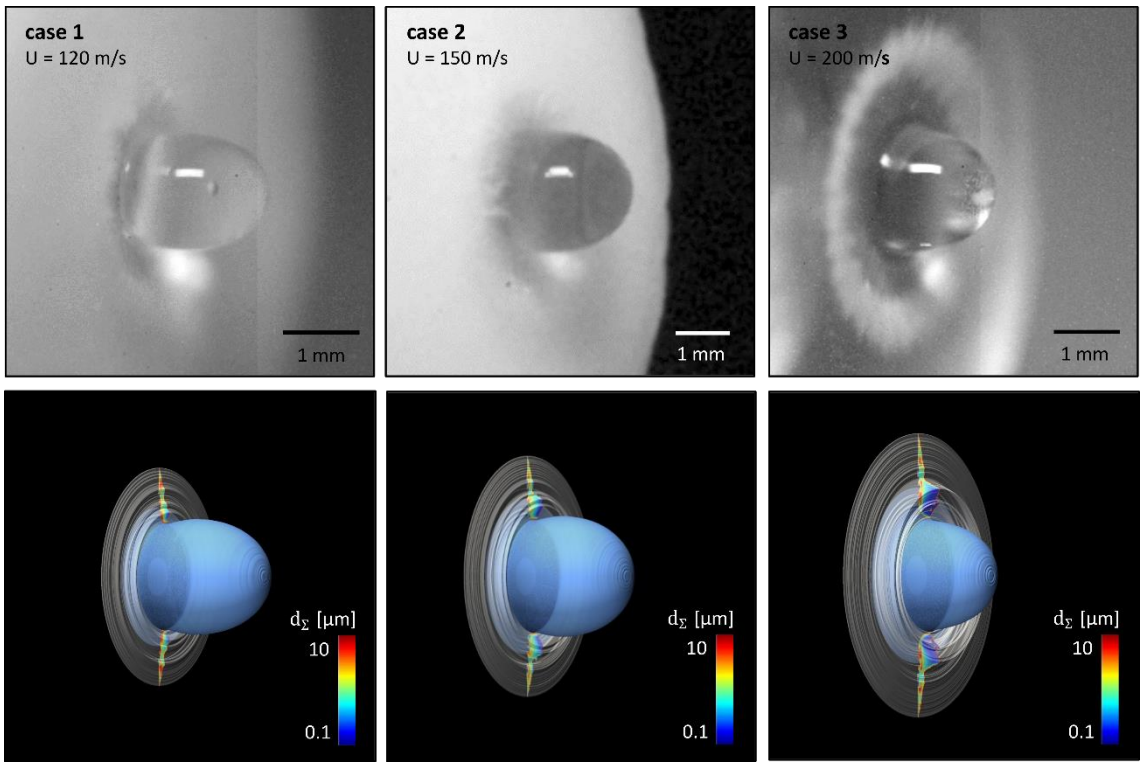


**Figure 2.8** Droplet fragmentation 2μs after impact on the target in cases 1, 2, 3. Comparison between the experimental results captured 32º from the perpendicular view and the 3D reconstructed flow fields from the simulation. Blue iso-surface represents the sharp interface regions and grey iso-surface the diffuse interface regions calculated with the multiscale two-fluid approach.

splashing with a widespread water cloud corona to be captured both by the experimental results and the simulation. However, the water microjet injected from the centre of the deforming droplet surface opposite to the droplet motion, which is depicted in the experimental captures as an effect of the secondary cavitation formation inside the droplet, is a low intensity phenomenon compared to the dominant and rapid water dispersion.

The evolution of the droplet impact with the target under the impact velocity of 150m/s (case 2), the prompt splashing at the early stages of impact along with the severe fragmentation and water dispersion at later stages are presented in Figures 2.11 and 2.12. In successive time instances, the experimental video snapshots are compared with the 3D reconstructed water volume fraction iso-surface at $10^{-3}$ obtained from the performed simulations with the proposed multiscale two-fluid model and the compressibleInterFoam solver, which is based on a VOF method commonly used for this type of problems. The iso-line of the water volume fraction at a value of $10^{-5}$, as calculated with the multiscale two-fluid approach, is plotted against the experimental results. Moreover, the detected dispersed flow regions using 3 different computational grids, namely the original grid of

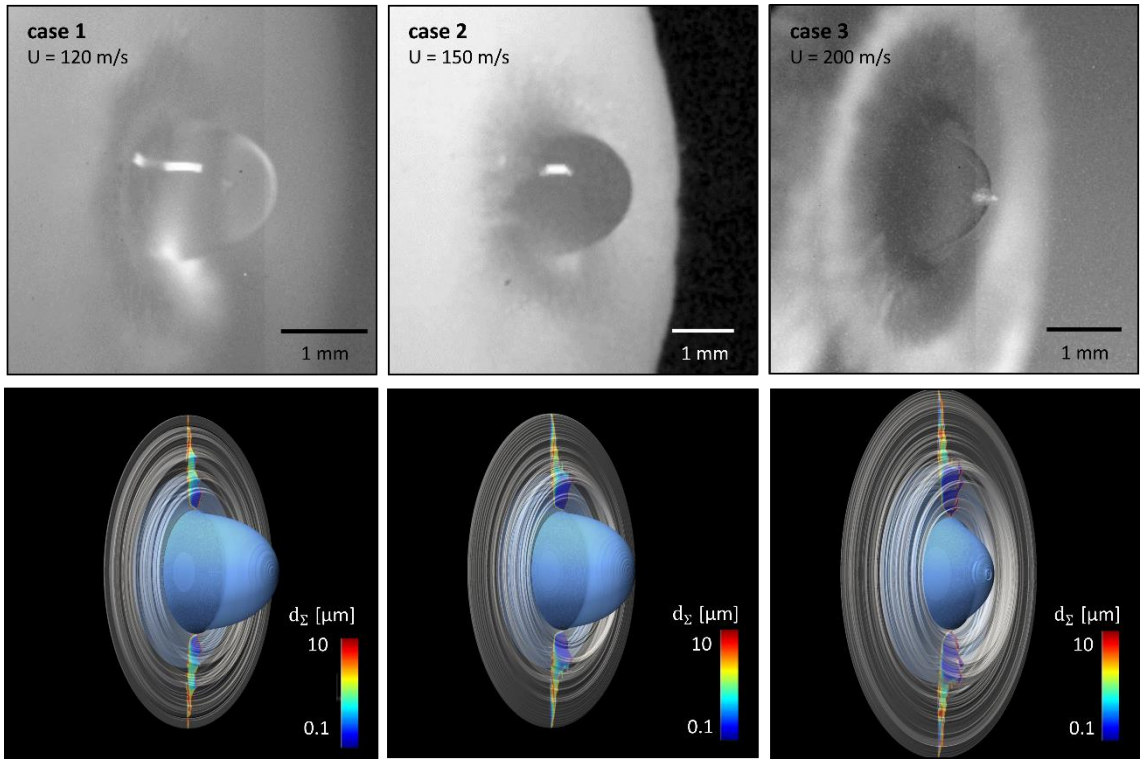


**Figure 2.9** Droplet fragmentation 4μs after impact on the target in cases 1, 2, 3. Comparison between the experimental results captured 32º from the perpendicular view and the 3D reconstructed flow fields from the simulation. Blue iso-surface represents the sharp interface regions and grey iso-surface the diffuse interface regions calculated with the multiscale two-fluid approach.

Figure 2.7 along with two new grids with twice coarser and twice finer resolution in region I, respectively, are presented to depict the dependency of the interfacial approaches capabilities and the performed topological investigation on the local mesh resolution.

As it can be observed in Figure 2.11, at the moment of impact the flow field is dominated by a segregated flow regime with perfectly separated two phases as defined by the droplet interface. Thus, up to this point, the sharp interface approach is applied exclusively in the whole flow field; good results are obtained with respect to the initial droplet shape. At that time, the occurring impact conditions correspond to a very high Weber number of $7.6\times10^5$ and thus, a prompt splashing is imposed driven by the dominant droplet inertia. Subsequently, the violent impact conditions do not allow for a liquid lamella to be formed, as depicted in the experimental results; instead, the production of a dense cloud of secondary droplets and ligaments is observed, which is moving radially ahead of the deformed droplet. At these stages, which correspond to times 1-3μs in Figure 2.11, the topological algorithm detects the first transitions in the dispersed flow regime; the cloud of the produced fluid structures after the droplet and wall impact is subject to a

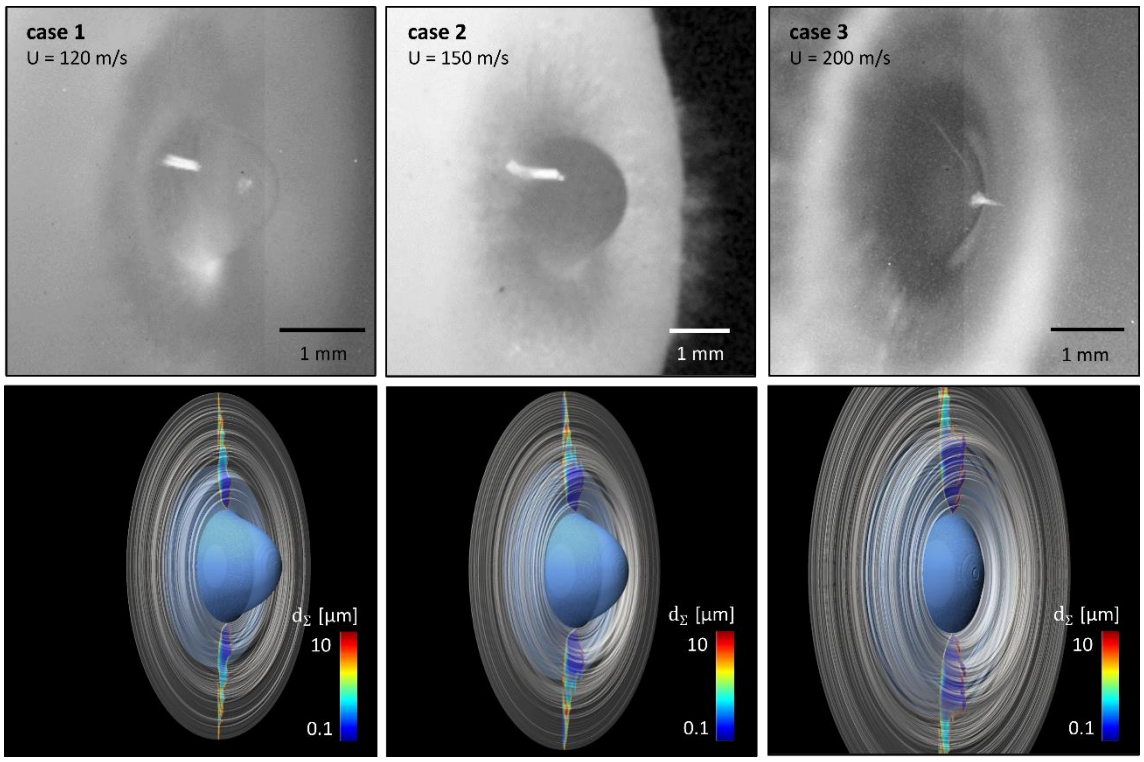


**Figure 2.10** Droplet fragmentation 6μs after impact on the target in cases 1, 2, 3. Comparison between the experimental results captured 32º from the perpendicular view and the 3D reconstructed flow fields from the simulation. Blue iso-surface represents the sharp interface regions and grey iso-surface the diffuse interface regions calculated with the multiscale two-fluid approach.

diffuse interface approach, since it consists of structures smaller than $10^{-5}$m that cannot be resolved by the local mesh resolution. On the contrary, the simulation with the VOF method applied in the whole flow field captures accurately the tendency of a radial water expansion.

However, the overall sharp interface formulation leads to the prediction of an unphysical thin water film after the impact, as in the case of a well-formed lamella under moderate impact conditions, instead of the experimentally observed wide cloud of secondary droplets. This predicted behaviour corresponds to the deficiency of the VOF method to resolve small fluid structures in the sub-grid scale limit. As a result, the computational cells with relatively small volume fractions, that imply the existence of microscale secondary droplets, are underestimated and therefore, a thin water film is calculated in the regions of a high-water volume fraction concentration. It is interesting to notice that at the examined early stages of impact, the multiscale two-fluid model with a finer mesh can predict more accurately the extent of the water spatial dispersion compared to the original or an even coarser mesh, as it is illustrated in Figure 2.11 at 2 and 3μs. Given the fact that large-scale structures dominate the dispersed regions at early times

after impact, it is expected that a finer mesh can obtain most of the flow field information with the multiscale model to operate under a diffuse interface approach. Nevertheless, this is not the case for the later stages of impact, in which the microscale droplets overtake the larger initially produced droplets of the dense water cloud, as it will be discussed afterwards.

Later stages of the droplet impact are depicted in Figure 2.12, where the flow is highly dispersed with an extended cloud of secondary features expanding radially away from the target. A widespread dispersed region in the form of an expanding corona is also captured by the multiscale two-fluid model; however, the calculated radial water dispersion is limited compared to the experimental observation. More specifically, after 4μs in regions of apparent water concentration in the experiment, approximately 1 mm away from the target, there is not any significant amount of water volume fraction present in the simulation. Moreover, as shown in Figures 2.8, 2.9, 2.10, the smaller structures are underestimated at the outer sides of the expanding cloud and the mixing of the injected water with the surrounding air is limited. Due to the supersonic conditions of the expelled surrounding air at the later stages of impact and the significant increase in local air temperature, vaporisation may be the key mechanism of water dispersion at the borders of the expanding water cloud; thus, the consideration of vaporisation effects should lead to an improved and more realistic capturing of the extended water dispersion at the later stages of impact. However, as it is comprehensively presented in Figure 2.13, the vertical expansion of both the attached-on-wall water film and the dispersed secondary droplets cloud is well predicted with the performed simulation under the existing highly multiscale conditions in the course of the impact and meets satisfactorily the experimental measurements for the lower values of the water volume fraction. Therefore, the obtained results provide a relatively accurate insight into the presence of an extended and chaotic water dispersion in contrast to the VOF method results, which are restricted to a non-realistic water film spreading with only a few droplets being formed as a numerical result of the strict sharp interface implementation. Within the scope of a grid dependency analysis, it is noticeable in Figure 2.12 that for the occurring dominant dispersed flow regime, a coarser computational mesh along with the multiscale approach can provide locally a more extended radial water dispersion region. Some of the original computational cells with negligible water volume fraction are now incorporated to neighbour cells and therefore, are subject to a diffuse interface regime for the modelling of local sub-grid scale secondary droplets with dimensions even less than 1μm. This behaviour comes in contrast to the results obtained with the multiscale approach and a finer mesh, which predict a limited radial water spreading and

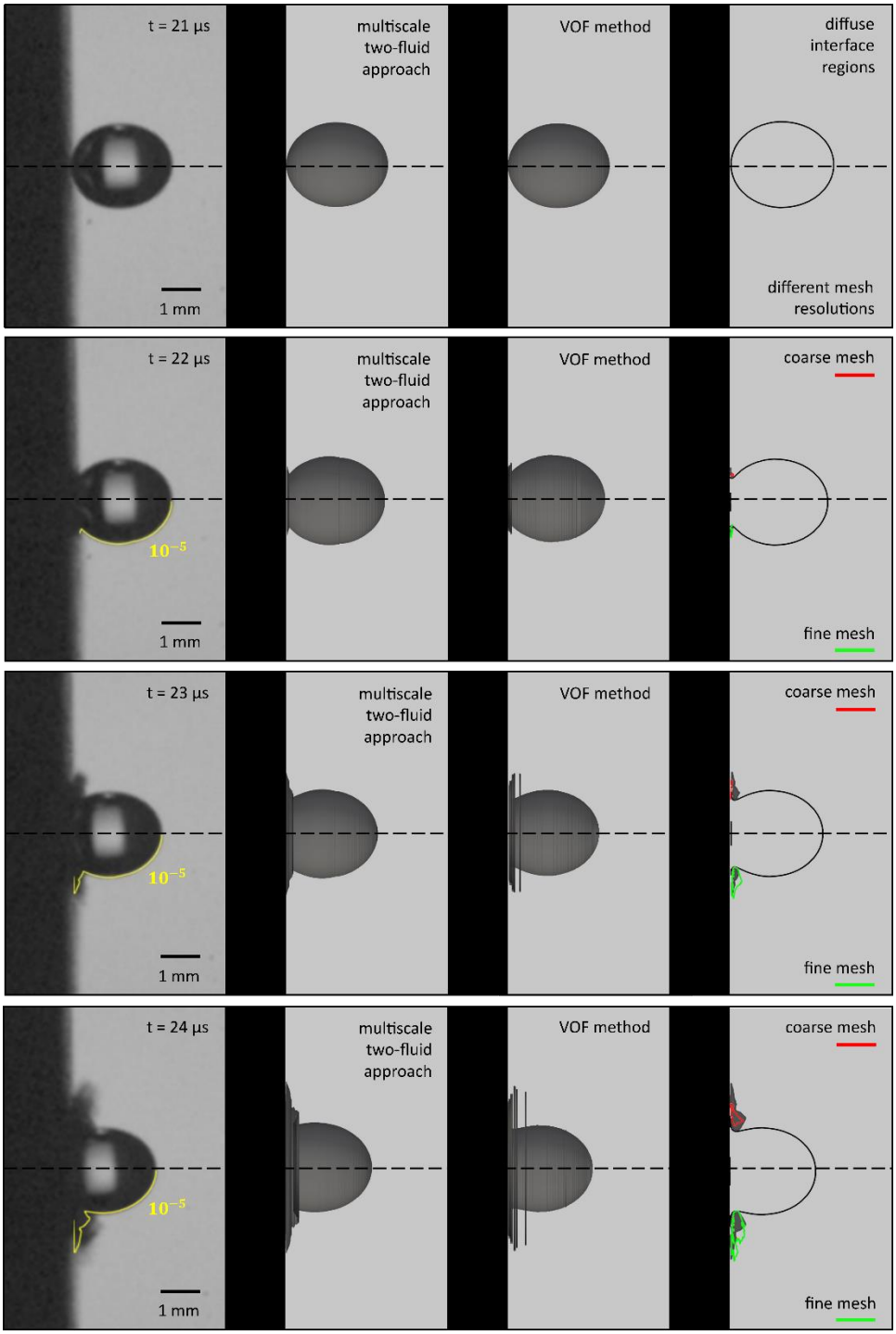


**Figure 2.11** Early stages of droplet impact with the target under the impact velocity of 150m/s (case 2). Comparisons between the experimental results from side view and the 3D reconstructed water volume fraction iso-surface at $10^{-3}$ obtained with the multiscale two-fluid model and the VOF method. The diffuse interface regions, calculated with the multiscale two-fluid model using 3 different mesh resolutions, are compared in the last column. Yellow iso-line represents the water volume fraction at $10^{-5}$, red isoline the diffuse interface regions using a coarse mesh and green isoline the diffuse interface region using a fine mesh.

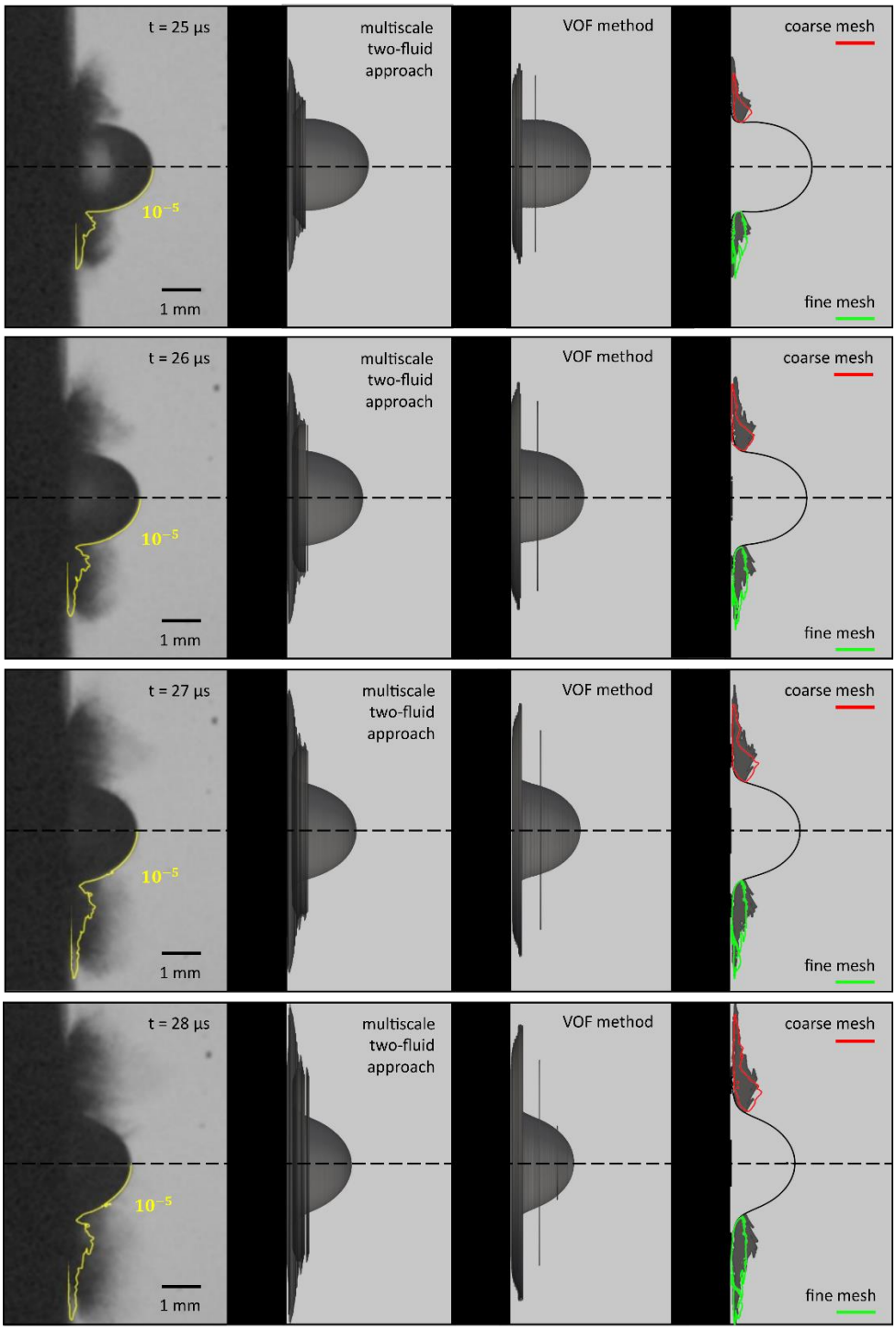


**Figure 2.12** Later stages of droplet impact with the target and intense water dispersion under the impact velocity of 150m/s (case 2). Comparisons between the experimental results from side view and the 3D reconstructed water volume fraction iso-surface at $10^{-3}$ obtained with the multiscale two-fluid model and the VOF method. The diffuse interface regions, calculated with the multiscale two-fluid model using 3 different mesh resolutions, are compared in the last column. Yellow iso-line represents the water volume fraction at $10^{-5}$, red isoline the diffuse interface regions using a coarse mesh and green isoline the diffuse interface region using a fine mesh.

approach the results of the pure VOF simulation. Consequently, the application of the multiscale two-fluid model in flow regions with multiple dynamic transitions between the segregated and dispersed regimes using a locally uniform computational grid, as performed in the conducted simulations, requires a compromise regarding the selected grid resolution. More specifically, given the numerical limitations of the VOF and the diffuse interface methods with respect to the computational grid and the switching criteria of the flow topology detection algorithm, an intermediate grid resolution is defined as optimum.

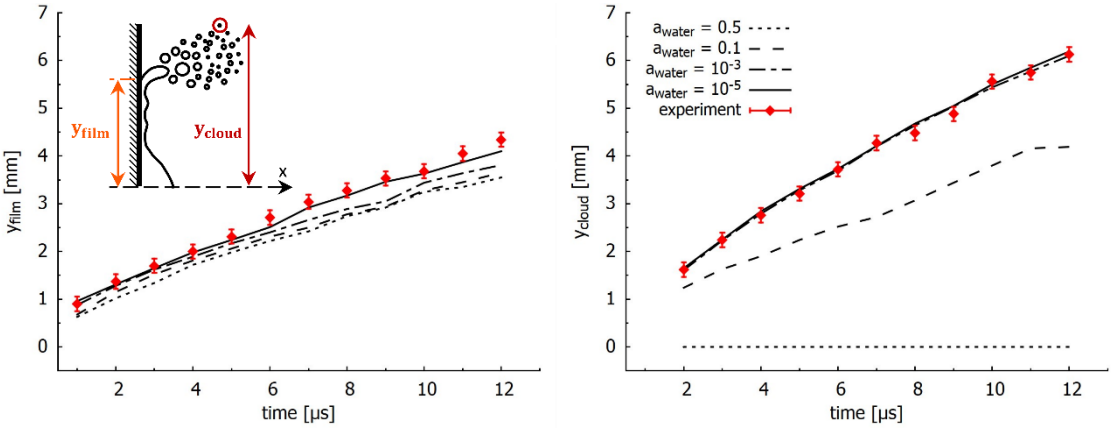


**Figure 2.13** Droplet fragmentation under the impact velocity of 150m/s (case 2). Comparisons between the experimental and the numerical results with different water volume fraction values for the vertical expansion of the attached-on wall-water film and the secondary droplets cloud.

The high-speed droplet impact is governed by significant compressibility effects inside the droplet at the early stages of the interaction with the rigid wall. After the moment that the droplet reaches the wall, a strong shock wave is formed inside the droplet with local pressure up to 1200bar, as depicted in Figure 2.14 at 0.4μs. The shock wave is propagating and moving outwards, opposite to the droplet motion, while it gradually overtakes the contact line between the target and the deforming droplet. At 1.7μs, it is observed that the shock wave is reflected normal to the droplet outer free surface and an expansion wave adjacent to the free surface is created, as previously observed by Haller et al. [88] and Wu et al. [91]. Afterwards, the shock wave propagation continues with the formation of an increasing low-pressure region inside the droplet, until the time it reaches the boundary of the deforming droplet interface, and it is reflected backwards at 2.7μs. This shock wave reflection results to the creation of strong rarefaction waves at 2.9μs, as previously captured by Haller et al. [88] and Wu et al. [91] for similar impact cases; the shock wave reflection could result to extended cavitation regions inside the droplet. However, it has been shown in previous numerical studies of Niu & Wang [89], Kyriazis et al. [90] and Wu et

al. [91] that under similar conditions the produced vapour volume fraction after the shock wave reflection does not exceed the value of 0.03, defining a non-significant cavitation effect. Since the droplet impact evolution is not driven by cavitation under the examined impact conditions, a model for cavitation has not been implemented in the developed multiscale framework; instead, a very small volume fraction of air of the order of $10^{-6}$, which corresponds to the nucleation volume fraction, is introduced in the initial droplet volume fraction. Under this assumption, the small gaseous volumes inside the droplet will expand after the significant pressure drop, leading to volumes equal to those that would occur with cavitation. The pressure evolution inside the droplet will continue with the gradual elimination of the created regions of small gaseous volumes, as long as the droplet widespread splashing is dominating the surrounding flow field.

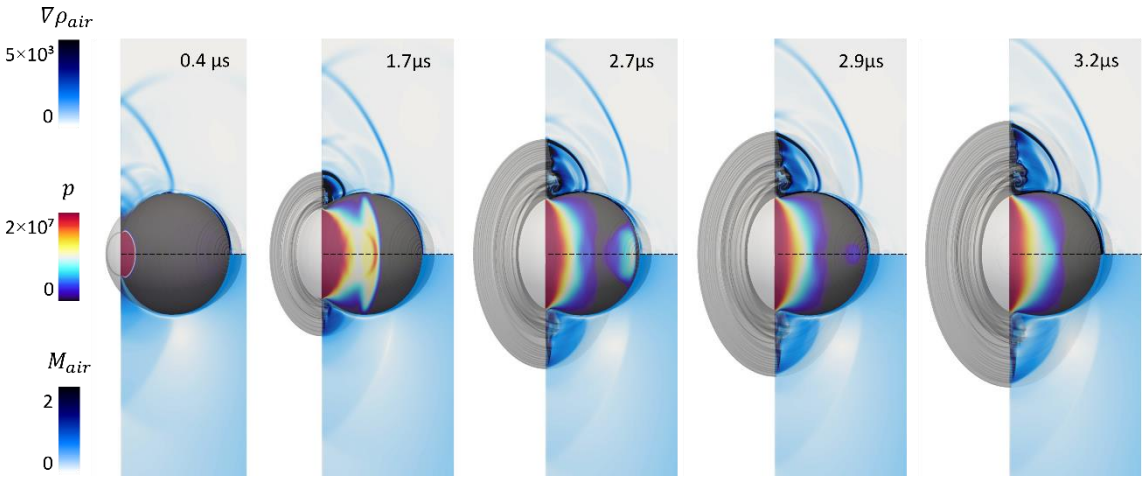


**Figure 2.14** Time evolution of the pressure field inside the droplet, the shock wave formation and propagation along with the density gradient and the Mach number for the surrounding air after the droplet impacting the rigid target with a velocity of 150m/s (case 2).

After the droplet impact and along with the beginning of a strong shock wave propagation inside the droplet, the development of a high-speed jetting is observed in Figure 2.15. The injected water film, which just after the droplet impact at 1μs has a velocity 5 times larger than the impact velocity, is responsible for the rapid lateral and radial water dispersion. This observation also meets the experimental measurements of a maximum liquid film expanding velocity at around 720m/s. At the same time, a supersonic flow with strong propagating shock waves is observed in the surrounding air, due to the high-speed dispersion of the produced water cloud. As illustrated in Figure 2.14, the formation and high-speed injection of the water film at the early stages of the droplet impact, corresponds to a violent displacement of the surrounding air, resulting to a supersonic flow of the air with local Mach numbers up to 2.5. Subsequently, during the droplet lateral spreading on the wall target, the intensity of the initial jetting and the propagating shock

waves in the air is reduced; however, the velocities of the water phase remain significant with peaks on the dispersed flow regions, where the secondary droplets cloud is penetrating the surrounding air. An examination of the temporal and spatial evolution of the relative velocities between the droplet and the surrounding air in Figure 2.15 comes to the same conclusion that the highest water velocities occur at the borders of the expanding water cloud. Thus, in highly dispersed flow regions, where practically very small droplets are present, the consideration of aerodynamic and slip velocity effects increases the physical coherency of the numerical model.

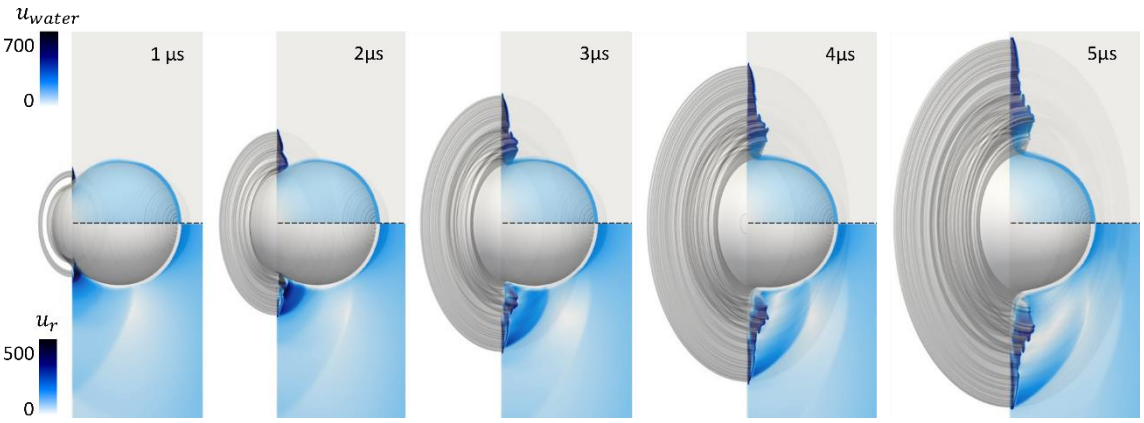


**Figure 2.15** Time evolution of the water velocity field inside the droplet and the relative velocity field in the surrounding area after the droplet impacting the rigid target with a velocity of 150m/s (case 2).

In Figure 2.16, the temporal evolution of the calculated interface surface area under different impact velocities is presented, as it is obtained from the transport equation for the liquid gas interface surface area density (2.5). A similar pattern regarding the interface surface area production over time is observed irrespectively of the impact conditions. More specifically, after the droplet impact the interface surface area is gradually increasing with the same rate until approximately point A. These time instances, as shown in Figure 2.17, correspond to the early stages of splashing, where the water film lateral spreading on the wall target dominates the formation and expansion of the dispersed water cloud. Since the surface area of the undeformed droplet interface remains unchanged, the maximum values of the interface surface area are observed on the dispersed regions away from the wall targe,t where sub-grid scale turbulent mixing and secondary droplet coalescence and breakup have a crucial effect on interface production, as described in equation (2.5). After that and until approximately point B in Figure 2.16, the interface surface area performs a rapid increase which is more intense with an increase on the impact velocity and is related to later stages of the fragmentation evolution with the water dispersion becoming the main effect on interface production. After point B and until the end of the observation of the phenomenon, an almost smooth increase in interface surface area is shown

due to the penetration of the previously produced secondary droplets cloud in the surrounding area.

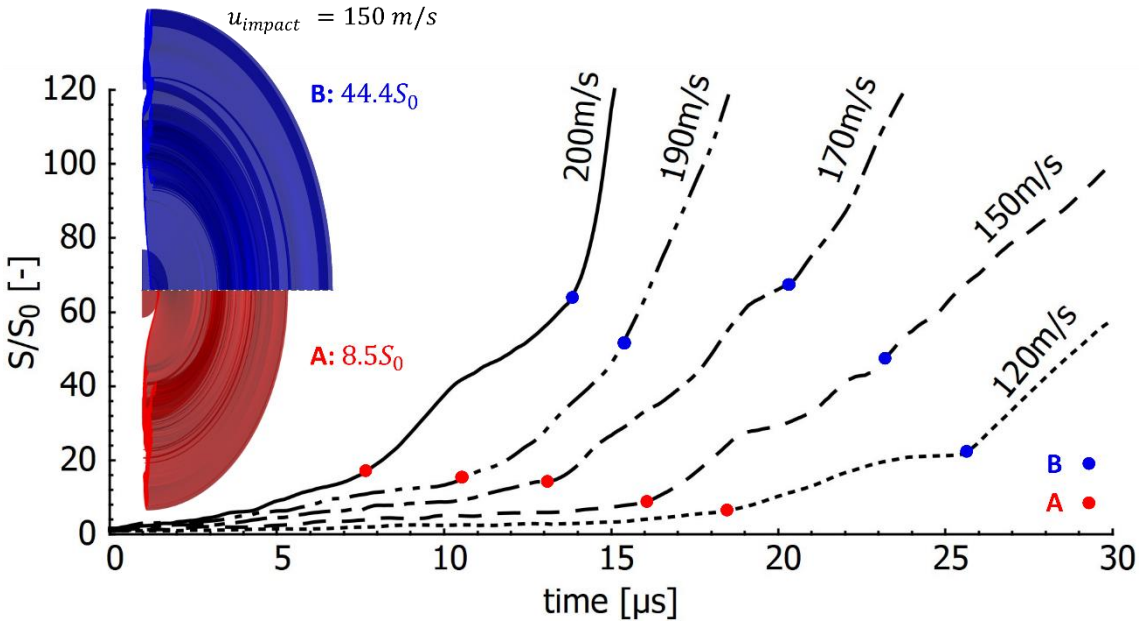


**Figure 2.16** Time evolution of the interface surface area for the developed water cloud and the secondary flow features after the droplet impact on wall with respect to the initial ellipsoid droplet surface area $S_0$ under different impact velocities. As time zero is set the moment of impact onto the rigid wall for the droplet with impact velocity 150m/s.

In Figure 2.18, two characteristic time instances at the earlier and later stages of the droplet fragmentation under the impact velocity of 150m/s are selected to depict the functionality of the flow topology detection algorithm. On the left side of the axis of symmetry the calculated diameters based on the interface curvature $d_{curv}$ are illustrated, which are used for the first geometric criterion of equation (2.16) in the sharp interface regions. As shown, the local interface curvature can obtain relatively large values which based on equation (2.15) are correlated with small fluid structures, reaching the limit of the local mesh resolution and the accuracy capabilities of the sharp interface approach. However, only the geometric criterion is not sufficient to keep a physical consistency regarding the areas of small $d_{curv}$ values, with such small fluid structures to be detected even in areas inside the deforming droplet core where the presence of small droplets has no physical interpretation. Thus, the additional topological criteria are the key factor in introducing a switching between sharp and diffuse interface approaches with respect to the local flow development and the physical transition from a segregated to a dispersed flow regime. The computational cells which satisfy both the geometric and the topological criteria and are subject to a diffuse interface formulation in the following time-step are marked in green. As expected,

these regions are detected at the borders of the already diffuse interface regions within the dispersed water cloud and they concern relatively large flow structures, which were previously resolvable by the mesh resolution with local minimum cell sizes of $10^{-5}$m. On the right side of Figure 2.18, the calculated interface surface area density diameters $d_\Sigma$ for the currently diffuse interface region within the highly dispersed secondary droplet cloud are illustrated. As shown, the local diameters used for the local drag force calculation range from the spectrum of microscales to $10^{-5}$m, which is the local minimum cell size and correspondingly the limit for a sub-grid scale analysis. In both time instances, a few computational cells are detected in the borders between sharp and diffuse interface approach regions with $d_\Sigma$ that exceed the local cell dimensions; these computational cells are subject to a sharp interface approach based on the geometric criterion of equation (2.17).

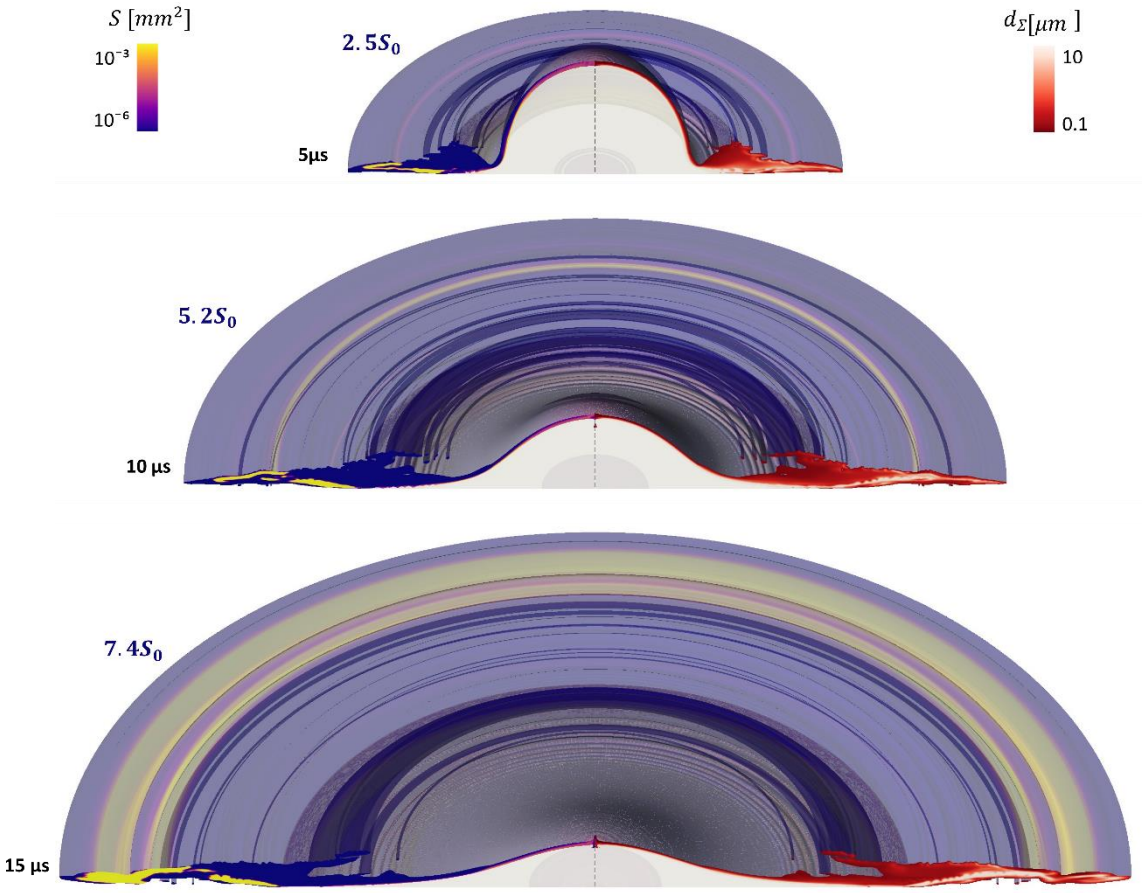


**Figure 2.17** Characteristic instances of the interface surface area evolution with respect to the initial ellipsoid droplet surface area $S_0$ and the calculated diameters under the impact velocity of 150m/s (case 2).

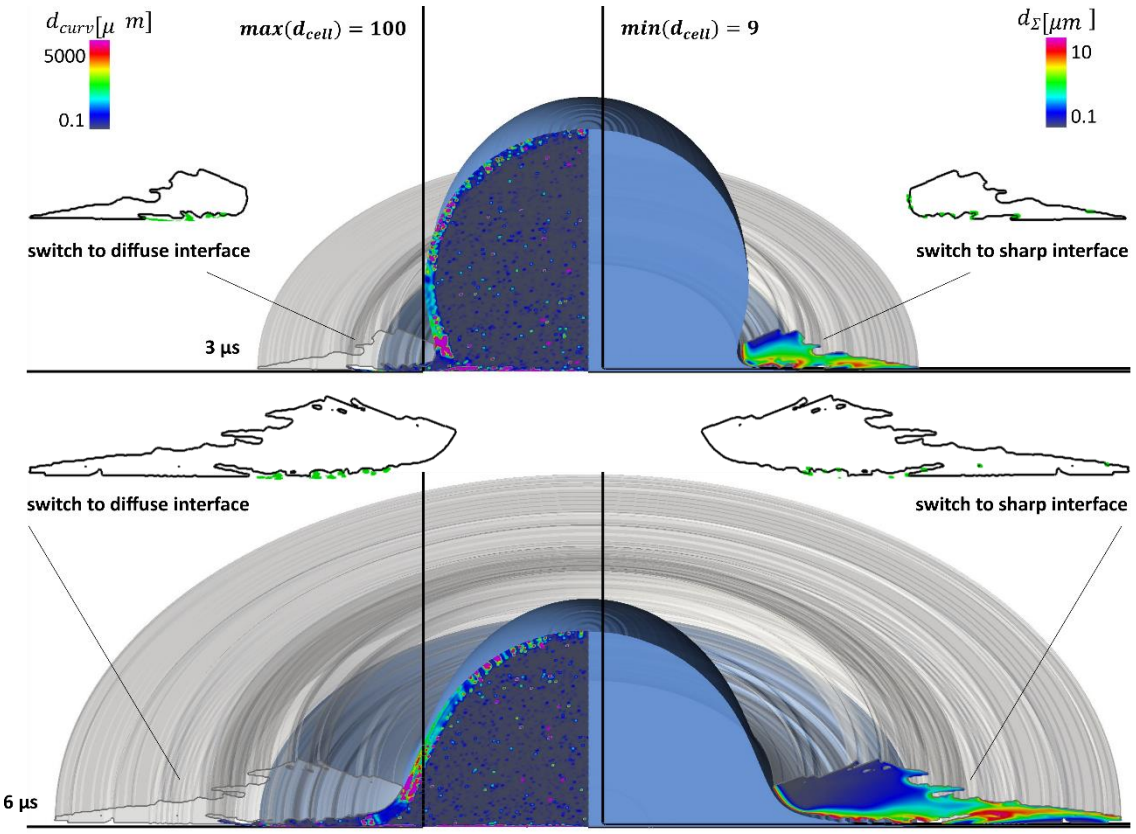


**Figure 2.18** Droplet fragmentation with impact velocity 150m/s (case 2). Blue iso-surface represents the sharp interface regions and grey iso-surface the diffuse interface regions calculated with the multiscale two-fluid approach. (On the left) The calculated diameters based on the interface curvature. In green are marked the cells switching from sharp to diffuse interface approach. (On the right) The calculated interface surface area density diameters. In green are marked the cells switching from diffuse to sharp interface approach.

Considerable emphasis has been put on correlating the geometric switching criteria of the flow topology detection algorithm, which in essence act as an indication for the numerical capabilities of the sharp and diffuse interface approaches, with the physically observed transition between different flow regimes during the flow development. Therefore, in Figure 2.19 the Weber and Reynolds numbers for the dispersed secondary droplets after impact are presented, which are subject to an aerodynamic breakup induced by the relative velocity between the injected droplet with calculated diameter $d_{\Sigma}$ and the expelled surrounding air. As illustrated for successive time instances, the flow development after impact is restricted by the limit of Ohnesorge numbers less than 0.1, which indicates that the produced secondary droplets breakup is mainly controlled by the droplet Weber number, as described in Guildenbecher et al. [18]. Additionally, only inside the diffuse interface region are observed Weber numbers with values larger than 0.5, which correspond to the beginning of the droplets oscillation and deformation, as defined in

Guildenbecher et al. [18], confirming that the flow topology detection accurately predicts the dispersed flow. Within the diffuse interface region and closer to the edges of the radially expanding cloud of secondary droplets regions with increasing Weber number and values larger than 10 are detected, which is set as a limit for the droplet aerodynamic breakup in the review study Guildenbecher et al. [18].

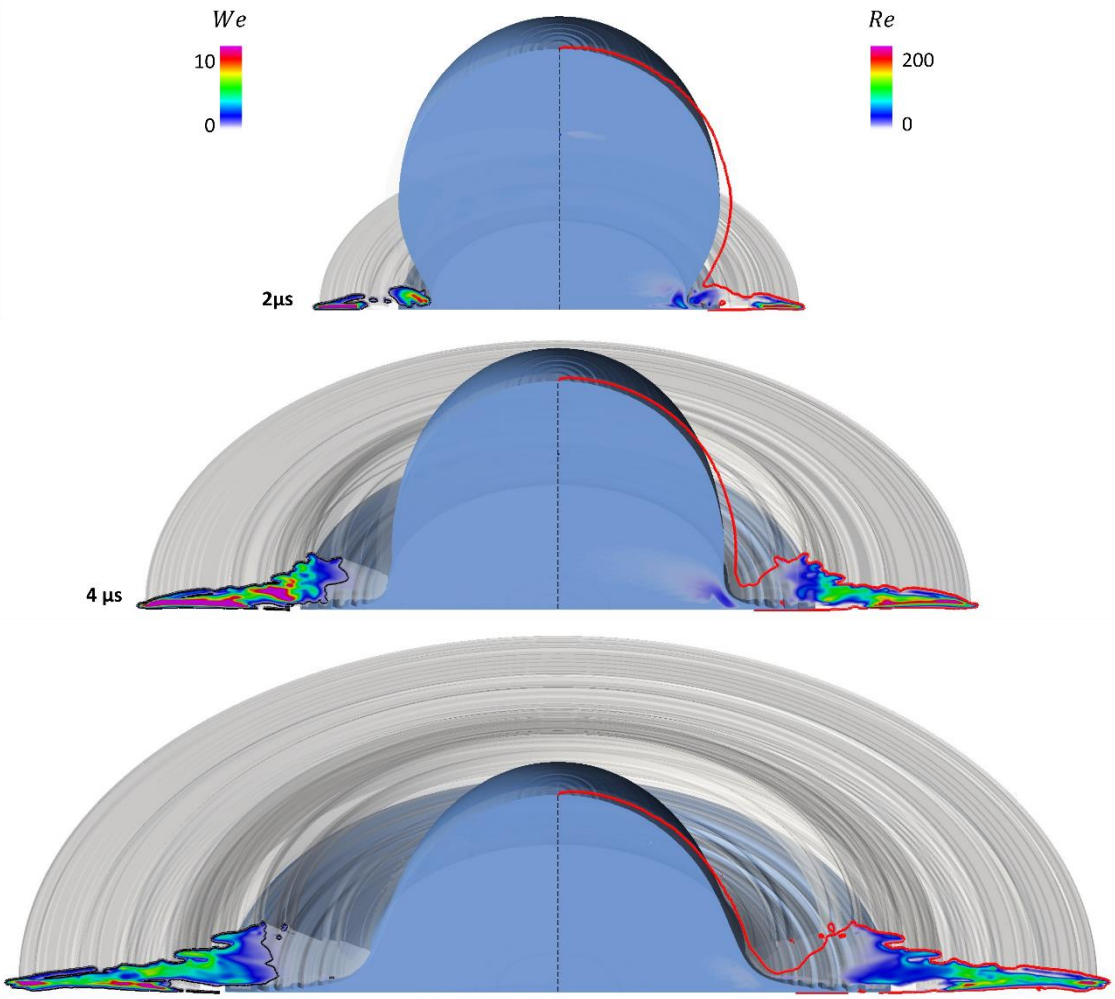


**Figure 2.19** Droplet fragmentation with impact velocity 150m/s (case 2). Blue iso-surface represents the sharp interface regions and grey iso-surface the diffuse interface regions calculated with the multiscale two-fluid approach. (On the left) The Weber number field for the aerodynamic breakup of the produced secondary droplets after impact. Black iso-line corresponds to Weber number value of 0.5. (On the right) The Reynolds number field for the aerodynamic breakup of the produced secondary droplets after impact. Red iso-line corresponds to Ohnesorge number value of 0.1.

## 2.4 Summary

A compressible Σ-Y two-fluid model with dynamic interface sharpening based on local topological criteria has been developed and implemented in OpenFOAM ®. The aim of the present study was to simulate highly compressible flows with significant slip velocity effects and multiscale complexities using a uniform solver, which detects dynamically the different coexisting flow regimes and operates under the most appropriate formulation. The numerically challenging coupling of a two-fluid model with an interface sharpening method has been examined and validated against a benchmark case of a shock tube and a rising bubble, obtaining useful results on how to eliminate the relative velocity at the interfacial region to achieve an effective coupling.

The model functionality has been thoroughly examined and applied in the highly compressible and multiscale case of a high-speed droplet impact; new experiments have been performed for a water droplet splashing on a surface at Weber number ~$10^5$ that have not been previously reported in the literature. The obtained results have shown a good agreement with the conducted experimental study regarding the capturing of the macroscopic characteristics of droplet fragmentation. Additionally, the proposed model has provided significant advantages particularly under a dispersed flow regime which dominates the later stages of droplet splashing in comparison to numerical methods imposing a sharpened interface and thus, excluding all the relevant sub-grid scale phenomena. The developed multiscale two-fluid methodology contributes with significant additional information regarding the physical phenomenon evolution, like the relative velocity field, the shock waves development, and the interface surface area evolution, which have contributed to a better understanding and more accurate modelling of complex multiscale flow fields.

# 3 DROPLET AEROBREAKUP

A droplet exposed to a high-speed gas flow is subject to a rapid and violent fragmentation, dominated by a widespread mist of multiscale structures that introduces significant complexities in numerical studies. In the present chapter, the aerodynamic breakup of a water-like droplet imposed by three different intensity shock waves, with Mach numbers of 1.21, 1.46 and 2.64, is investigated using the multiscale two-fluid approach. Overall, the breakup of the deforming droplet and the subsequent dispersion of the produced mist show good agreement with available experimental studies in the literature. The major features and physical mechanisms of breakup, including the incident shock wave dynamics and the vortices development, are discussed, and verified against the experiments and the theory. While the experimental visualizations inside the dense mist are restricted by the capabilities of the diagnostic methods, the multiscale two-fluid approach provides insight into the mist dynamics and the distribution of the secondary droplets under different post-shock conditions.

---

*Published as:

G. Nykteri and M. Gavaises, “Droplet Aerobreakup under the Shear-Induced Entrainment Regime Using a Multiscale Two-Fluid Approach”, *Physical Review Fluids*, vol. 6, p. 084304, 2021.

# 3.1 Introduction

The aerodynamic breakup of a liquid droplet imposed by a passing shock wave is a fundamental problem with a wide spectrum of engineering interest, ranging from fuel injection in both internal combustion [18], [112], [113], [114] and rocket engines [115], [116] to erosion damage in supersonic flights [117], [118]. Different classifications for the droplet breakup regimes are reported in the literature and defined based on key dimensionless parameters, namely the Weber number (We) at free-stream conditions and the Ohnesorge number (Oh) for the liquid droplet, as follows:

$$We = \frac{\rho_g u_g^2 d_0}{\sigma} \quad , \qquad Oh = \frac{\mu_l}{\sqrt{\rho_l \sigma d_0}}$$

with $d_0$ the initial droplet diameter, σ the surface tension coefficient, $\rho_g$ the post-shock gas density, $u_g$ the post-shock gas velocity, $\rho_l$ the liquid density and $\mu_l$ the liquid dynamic viscosity.

The five classic breakup modes, known as vibrational, bag, bag-and-stamen (or multimode), sheet-stripping (or sheet-thinning) and catastrophic regime, are summarized in a We-Oh regime map for low Ohnesorge numbers (Oh << 1) in the early review studies of Hinze [119], Pilch & Erdman [120] and Faeth et al. [121]. Recently, Stefanitsis et al. [122], [123], [124] provided improved breakup models for diesel droplets within the bag, bag-and-stamen and sheet-stripping regimes and identified an additional breakup mode, termed as "shuttlecock", which is observed during the aerodynamic breakup of droplet clusters at low Mach numbers. On the other hand, Theofanous et al. [125] reclassified the classic droplet breakup modes into two principal regimes based on the governing interfacial instabilities, namely the Rayleigh-Taylor piercing (RTP) and the shear-induced entrainment (SIE) regime, introducing a broad and unified classification for both Newtonian and non-Newtonian droplets independent of the liquid viscosity and elasticity. Specifically, the RTP regime concerns a moderate droplet fragmentation, driven by a gradual flattening of the deforming droplet and a subsequent penetration of its accelerating mass by one or more unstable Rayleigh-Taylor waves. On the contrary, the SIE regime describes a chaotic fragmentation, defined by the prompt shear stripping from the droplet equator and followed by an extended entrainment of a multiscale mist. Dominant mechanisms that induce the droplet breakup are the Kelvin-Helmholtz instabilities, the capillary forces and the turbulent mixing, as described by Theofanous [5]. For low viscosity liquids with Ohnesorge numbers Oh<<1, the onset of the SIE regime is established for Weber numbers above $10^3$, while the transition zone between the RTP and SIE regimes occurs for moderate Weber numbers in the range of $10^2$ to $10^3$.

Early experimental investigations of the SIE regime are focused on shadowgraphy experiments of water droplets, in a first attempt to depict and explain the stripping mechanism. Engel [126] examined the fragmentation of a large (2.7mm diameter) and a small (1.4mm diameter) water droplet imposed by three different shock waves of Mach numbers 1.3, 1.5 and 1.7 in order to demonstrate the influence of the sizes of rain droplets in the high-speed rain-erosion damage. Additionally, Nicholls & Ranger [127] considered incident shock waves with Mach numbers up to 3.5 and investigated the role of various parameters in the droplet aerobreakup evolution, such as the droplet diameter, the breakup time, the relative velocity between the droplet and the gas stream and the liquid-to-gas density ratio. Even though the macroscopic features of aerobreakup are revealed in both experimental studies [126], [127], namely the liquid stripping from the droplet surface and the production of an extended mist, the shadowgraphy method imposes limitations in displaying details of the internal structure of the dense water cloud. Alternatively, the pulsed laser holographic interferometry is proposed in the experiments of Wierzba & Takayama [128] and Yoshida & Takayama [129] and provides more clear and measurable visualizations of the shock-droplet interaction, the structure of the disintegrating droplet and the formation of a wake region behind the droplet under moderate Weber numbers around $10^3$ and Mach numbers between 1.3 and 1.56.

In current research, great emphasis is put on understanding the breakup mechanisms of liquid droplets, other than water droplets, of both Newtonian and non-Newtonian nature, as shown in the works of Theofanous & Li [130], Theofanous et al. [4], [131] and Mitkin & Theofanous [132]. Using laser-induced florescence (LIF), significant flow features are elucidated for the first time within a vast range of Weber and Ohnesorge numbers, including the initial Kelvin-Helmholtz waves on the coherent droplet surface and the development of different scales inside the dense mist at later stages of aerobreakup. In the case of elastic liquids, it is observed that the SIE regime is not subject to capillary forces; instead, the breakup initiates with the ruptures of extending liquid films and filaments at significantly higher Weber numbers, referred to as shear-induced entrainment with ruptures (SIER). Furthermore, recent studies in the literature investigate the effect of the post-shock flow on the initiation and evolution of the aerobreakup. Wang et al. [133] examined the effect of the gas stream conditions on the macroscopic breakup pattern and the final dispersion of the produced secondary structures for a constant Weber number at 1100 and varied post-shock flow Mach numbers in the range of 0.3 to 1.19. Specifically, the mist penetration and the fragment sizes show a dependency on the gas stream conditions and thus, a narrower mist of less uniform fragments is observed at the advanced stages of aerobreakup under supersonic post-

shock conditions. Finally, Hébert at al. [134] presented experiments for significantly high Mach numbers between 4.2 and 4.6 and Weber numbers above $10^5$ and defined the three stages and characteristic times of the breakup mechanism in supersonic post-shock flow, namely the droplet deformation, the extended fragmentation and the formation of a filament from the remaining liquid mass.

An important and still uninvestigated feature of the shear-induced breakup mechanism concerns the dynamics of the dense and polydisperse mist, which is forming and disintegrating as a result of the droplet fragmentation. Even with state-of-the-art laboratory apparatus available, the access to information about the dimensions of the produced structures within the mist remains challenging. The attempts to obtain droplet size distributions from high-quality experimental data visualizations in the up-to-date literature, employed by Hsiang & Faeth [135], [136], [137], Villermaux [8] and Xu [138], are restricted to cases with moderate breakup, falling in the transition zone between the RTP and SIE regimes. Recent experimental studies of the SIE regime, such as the works of Theofanous [5], Theofanous et al. [4] and Wang et al. [133], provide a thorough investigation of the dominant physical mechanisms that influence the development of the dispersed mist. However, a quantification of the obtained fragment sizes inside the mist is not available.

A key characteristic of the droplet aerobreakup under the SIE regime is the broad range of spatial and temporal scales involved, which introduces additional difficulties in the accurate capturing of the overall droplet deformation and fragmentation with the available numerical methods. Two-dimensional simulations are suggested in the literature as a good compromise between the assumption of a fully symmetric droplet fragmentation and the prohibitive computational cost of a full-scale analysis. Specifically, the planar breakup of a cylindrical water column is a commonly adopted simplified problem to study the shock-imposed breakup and the shear-stripping mechanism. In the first numerical study of the entire shear-induced breakup process, Chen [139] simulated the aerobreakup of a water column after the impact with two different shock waves with Mach numbers 1.3 and 1.47, using the five-equation model of Saurel & Abgrall [140]. The simulations capture the macro-scale phenomena of the droplet deformation and displacement and show a good agreement with the experimental observations of Igra & Takayama [141]; however, the utilized diffuse interface approach imposes limitations regarding the sharpness of the coherent droplet interface. Similarly, with the use of the diffuse five-equation model of Allaire et al. [142], Meng & Colonius [143] provided simulations for the water column aerobreakup within a broader range of conditions with shock wave Mach numbers between 1.18 and 2.5; for the first time, the

development of a recirculation region behind the deforming droplet is investigated. Sembian et al. [144] conducted new experiments and simulations with the Volume of Fluid (VOF) method for the early stages of the shock-water column interaction for shock wave Mach numbers 1.75 and 2.4; details of the shock waves motion are captured by the VOF method and a resolution of 440 cells per diameter. Yang & Peng [145] examined the effect of viscosity on the deformation of the liquid column, using an adaptive mesh refinement (AMR) method for higher spatial resolution. More recently, Kaiser et al. [146] performed high-resolution simulations with adaptive mesh refinement for the benchmark case of Mach number 1.47, previously simulated by Chen [139], Meng & Colonius [143] and Yang & Peng [145], with an emphasis put on the more accurate prediction of the shock wave dynamics, observed in the experiments of Igra & Takayama [147], [148]. Overall, the two-dimensional simulations of the shear-induced droplet breakup in the literature focus on the capturing of the early stages of breakup and the shock wave dynamics, without investigating the later stages of fragmentation and mist development.

Considering the high computational cost of a full-scale analysis, the limitation of the ordinary numerical methods to accurately model all different-scaled structures remains the main source of deviation between the simulation results and the experimental observations. Among the reported three-dimensional simulations in the up-to-date literature, Meng & Colonius [24] utilized an interface capturing method and a moderate mesh resolution of 100 cells per original droplet diameter to capture the macroscopic droplet deformation and achieved a good agreement with the experimental results of Theofanous et al. [4] for a shock wave Mach number 1.47 and post-shock flow Weber number 780. Additionally, a Fourier analysis was performed to interpret the mechanisms of the observed surface instabilities and the subsequent ligament breakup. Liu et al. [10] conducted both axisymmetric and three-dimensional simulations to examine the aerobreakup mechanism under supersonic conditions and identified significant details of the liquid stripping and the vortices development at the early stages of aerobreakup. In an attempt to investigate water dispersion, Stefanitsis et al. [149] proposed a coupled VOF/Lagrangian approach to simulate the coherent droplet and the produced droplets cloud, respectively. The obtained results predict the detachment of micro-scale droplets from the coherent droplet periphery, as depicted in the experimental visualizations of Theofanous et al. [4]; however, with a lack of physical input for the sizes of the produced Lagrangian particles. Recently, an improved Eulerian/Lagrangian model is proposed by Kaiser et al. [150] that allows a pre-set number of Lagrangian particles to detach from the droplet surface and later, evolve in sizes, following the gas stream flow.

More sophisticated studies in the literature, including the direct numerical simulations (DNS) performed by Chang et al. [151], demonstrate the developed Kelvin-Helmholtz instabilities on the coherent droplet surface for a glycerol droplet impacted by a shock wave of Mach numbers 1.2 and 2.67. Additionally, the DNS study of Hébert et al. [134] reveals the characteristic stages and breakup times of the aerobreakup process for a water droplet under supersonic conditions with a shock wave Mach number equal to 4.24. The obtained results accurately capture the incident shock wave propagation and the subsequent bow shock formation, as observed in the conducted experiments by the same authors. However, despite the efficiency in computational resources, both DNS studies [151], [134] mainly focus on the early-stage dynamics and avoid investigating the dimensions of the secondary structures inside the dense water mist, which is captured as a detached but continuous filament in the simulations Hébert et al. [134] without any internal structures .

At the same time, thorough interpretations of all the stages of aerobreakup in the current literature concern only studies with moderate Weber numbers in the transition zone between the RTP and SIE regimes, namely with Weber numbers in the range of $10^2$ to $10^3$. Specifically, Dorschner et al. [152] presented a comprehensive analysis of the ligaments formation and disintegration for the case of a water droplet exposed to a shock wave of Mach number 1.3 and a subsequent post-shock flow with Weber number 470. The conducted simulations, using a multicomponent model with interface capturing and a moderate spatial resolution of 140 cells per diameter, accurately predict the recurrent breakup mechanism of the produced ligaments in consistence with the experimental observations. Additionally, in the studies of Jalaal & Mehravaran [153] and Jain et al. [154] a thorough quantitative analysis of the fragments development is demonstrated, along with information for the number of the produced fragments and secondary droplet size distributions. However, both numerical studies [153], [154] investigate flows with Weber numbers below $10^3$ and thus, concern the development of a relatively light mist of distinguishable larger-scaled fragments. A summary of the key numerical studies of droplet aerobreakup in the up-to-date literature, the utilized numerical methods, the examined conditions, and the experimental works used for validation is presented in Table 3.1. Overall, additional quantitative research is required to reveal all macroscopic and microscopic mechanisms at the later stages of breakup and provide an insight into the dense mist development under the SIE regime.

Following the limitations and challenges of the commonly adopted numerical methodologies for the simulation of droplet aerobreakup, there is a gap in the up-to-date literature concerning a detailed analysis of the dispersed mist development under the SIE regime, due to the dominance

of multiscale structures and the significant computational cost of a full-scale analysis. In the present chapter, the multiscale two-fluid approach is proposed in order to investigate the multiscale features of droplet aerobreakup with a viable computational cost. The multiscale two-fluid approach employs a sharp interface method for the deforming droplet interface and a physically consistent sub-grid scale modelling for the produced mist, using numerical models for the dominant sub-grid scale mechanisms previously validated and utilized in the literature for similar multiscale flows and conditions [155], [56]. The proposed numerical method is now utilized for the first time in the droplet aerobreakup problem and is found to predict accurately both the early-stage breakup mechanisms and the later-stage dispersion of the produced fragments imposed by three different shock waves with Mach numbers 1.21, 1.46 and 2.64, as presented in §3.3 and compared with the experimental observations of Theofanous [5] and Theofanous et al. [4]. The novelty of the present simulations lies on the thorough quantitative analysis of the droplet fragmentation and the produced mist dynamics. Specifically, during the early mist development, two stripping mechanisms are identified and investigated in consistence with the experimental visualizations. Additionally, the differences in the early and later mist development under subsonic and supersonic post-shock conditions are demonstrated and a physical interpretation is provided with respect to the evolution of the gas stream flow. Finally, for the first time in the up-to-date literature, a characterization of the droplets' population inside the dense mist is obtained and analysed based on the modelled sub-grid scale phenomena that govern the mist dynamics within the SIE regime.

**Table 3.1** Summary of the key numerical studies of droplet aerobreakup in the up-to-date literature.

| Year | Authors | Numerical Model | Simulation | $M_s$ | We | Experiments |
|---|---|---|---|---|---|---|
| 2008 | Chen [139] | five-equation model [140] (diffuse interface method) | 2D planar | 1.3<br>1.47 | $3.7 \times 10^3$<br>$7.4 \times 10^3$ | Igra & Takayama [141] |
| 2012 | Jalaal & Mehravaran [153] | AMR VOF method | DNS | - | 38 - 400 | Bremond & Villermaux [156]<br>Cao et al. [157] |
| 2013 | Chang et al. [151] | MuSiC$^+$ solver (high-order/ AMR method) | DNS | 1.2<br>2.67 | $5.2 \times 10^2$<br>$5.4 \times 10^4$ | Theofanous [5] |
| 2015 | Jain et al. [154] | AMR VOF method | 3D | - | 20 - 120 | Own |
| 2015 | Meng & Colonius [143] | five-equation model [142] (diffuse interface method) | 2D planar | 1.18 - 2.50 | 940 - $1.9 \times 10^4$ | Igra & Takayama [147], [141] |
| 2016 | Sembian et al. [144] | VOF method | 2D planar | 1.75<br>2.4 | $9.5 \times 10^4$<br>$3.8 \times 10^5$ | Own |
| 2018 | Liu et al. [10] | five-equation model [142] (anti-diffusion method) | 2D planar/ 3D | 1.2 – 1.8 (post-shock M) | $10^3 < We < 10^5$ | Sembian et al. [144] |
| 2018 | Meng & Colonius [24] | five-equation model [142] (interface capturing method) | 3D | 1.47 | 780 | Theofanous et al. [4] |
| 2019 | Yang & Peng [145] | AMR sharp-interface method | 2D planar | 1.47 | $7.4 \times 10^3$ | Igra & Takayama [148] |
| 2020 | Dorschner et al. [152] | multicomponent model with interface capturing | 3D | 1.3 | 470 | Own |
| 2020 | Hébert et al. [134] | Eulerian solver | 2D axisymmetric/ DNS | 4.24 | $1.2 \times 10^5$ | Own |
| 2020 | Kaiser et al. [146] | AMR Level-Set method | 2D planar | 1.47 | $7.4 \times 10^3$ | Igra & Takayama [147], [148] |
| 2021 | Kaiser et al. [150] | Eulerian/Lagrangian method | 2D planar | 1.47 | $7.4 \times 10^3$ | Igra & Takayama [148] |
| 2021 | Stefanitsis et al. [149] | VOF/Lagrangian method | 2D planar<br>3D | 1.47<br>1.24 | $7.4 \times 10^3$<br>780 | Igra & Takayama [147]<br>Theofanous et al. [4] |

## 3.2 Numerical Modelling

### 3.2.1 Numerical Method

The Σ-Y two-fluid model with dynamic local topology detection, as introduced in §2.2, is utilized for the droplet aerobreakup simulations. The developed multiscale two-fluid approach consists of a broad and numerically stable case-independent multiscale framework, and thus, no modifications were required for the present simulations. Therefore, the individual features of the proposed method allow for a physically consistent investigation of the multiscale aspects of droplet aerobreakup within the multiscale framework. Specifically, the implemented compressible two-fluid approach, introduced by Ishii & Mishima [38], provides remarkable advantages, due to the consideration of compressibility and slip velocity effects; both flow phenomena are responsible for inducing the droplet breakup mechanism under the SIE regime. Additionally, the incorporation of the Σ-Y model, which was initially proposed by Vallet & Borghi [53], contributes to a computationally efficient full-scale analysis, since it provides modelling solutions for the microscale droplets and the underlying sub-grid scale phenomena inside the widespread mist.

A fundamental feature of the multiscale framework is the topological detection of different flow regimes based on advanced on-the-fly criteria. As a result, the most appropriate modelling formulations are applied in each flow region, remaining in coherence with the local mesh resolution. Particularly, in segregated flow regions, which are present on the interface of the deforming but still coherent droplet, the interface is fully resolved using the VOF sharp interface method [45], [46]. On the contrary, inside the dispersed water mist with structures smaller than the local grid size, the methodology applies a diffuse interface approach and incorporates an additional transport equation for the interface surface area density Σ [55] in order to model the unresolved sub-grid scale phenomena.

The governing equations of the multiscale two fluid approach, along with details of the implementation in OpenFOAM®, are previously introduced in §2.2. Regarding the aerobreakup simulations of the present chapter, a comprehensive discussion about the validity of the utilized numerical models and the imposed assumptions within the multiscale framework is presented in Appendix 3.A.

## 3.2.2 Problem Definition and Simulation Set-up

The droplet aerobreakup is examined for a water-like droplet with an initial diameter of 1.9mm, namely a tri-butyl phosphate (TBP) droplet with density $\rho$=978kg/m³ and dynamic viscosity $\mu=4\times10^{-3}$Pa·s, similar to water properties, but a very low surface tension of $\sigma$=0.027N/m. The numerical simulations are conducted for three different shock waves that impact the droplet and correspond to a subsonic, transonic, and supersonic post-shock gas stream. The simulation results are compared with the experimental observations of Theofanous [5] and Theofanous et al. [4] for the same aerobreakup cases. The three examined cases comprehensively cover the range of the available experimental conditions for low viscosity liquids within the SIE regime in the literature, as depicted in the regimes map in [4]; the onset of the SIE regime is defined for Weber numbers greater than $10^3$ and demonstrates a moderate shear-induced aerobreakup, while the most intense and violent fragmentation is observed for significantly higher Weber numbers above $10^5$ and supersonic post-shock flow conditions.

Table 3.2 summarizes the Mach numbers of the propagating shock waves, the post-shock flow conditions and the Weber and Reynolds numbers calculated for the gas properties at post-shock conditions. The post-shock gas stream properties are also used for the non-dimensionalization of the flow fields, as shown in Meng & Colonius [24], in order to obtain a direct comparison between the different cases.

**Table 3.2** Shock wave and post-shock conditions for the conducted droplet aerobreakup simulations.

| case | $M_s$ | $p_s$ [Pa] | $T_s$ [K] | $\rho_s$ [kg/m$^3$] | $u_s$ [m/s] | We | Re |
|---|---|---|---|---|---|---|---|
| 1 | 1.21 | 156187 | 340.4 | 1.6 | 110.87 | $1.6 \times 10^3$ | $1.6 \times 10^4$ |
| 2 | 1.46 | 235094 | 388 | 2.11 | 224.97 | $7 \times 10^3$ | $3.7 \times 10^4$ |
| 3 | 2.64 | 807006 | 683.9 | 4.11 | 654.9 | $1.23 \times 10^5$ | $1.6 \times 10^5$ |

The droplet aerobreakup simulations are performed in a 2D axisymmetric geometry with one cell thickness in the azimuthal direction, using two computational meshes with a resolution of 100 and 200 cells per original droplet diameter around the area of interest. The computational domain is sufficiently large to avoid non-physical reflections on the borders and Neumann boundary conditions are applied for all the computed flow fields. The simulations are initiated with the shock wave being one diameter away from the centre of the droplet. Details of the initial configuration and the computational mesh are illustrated in Figure 3.1.

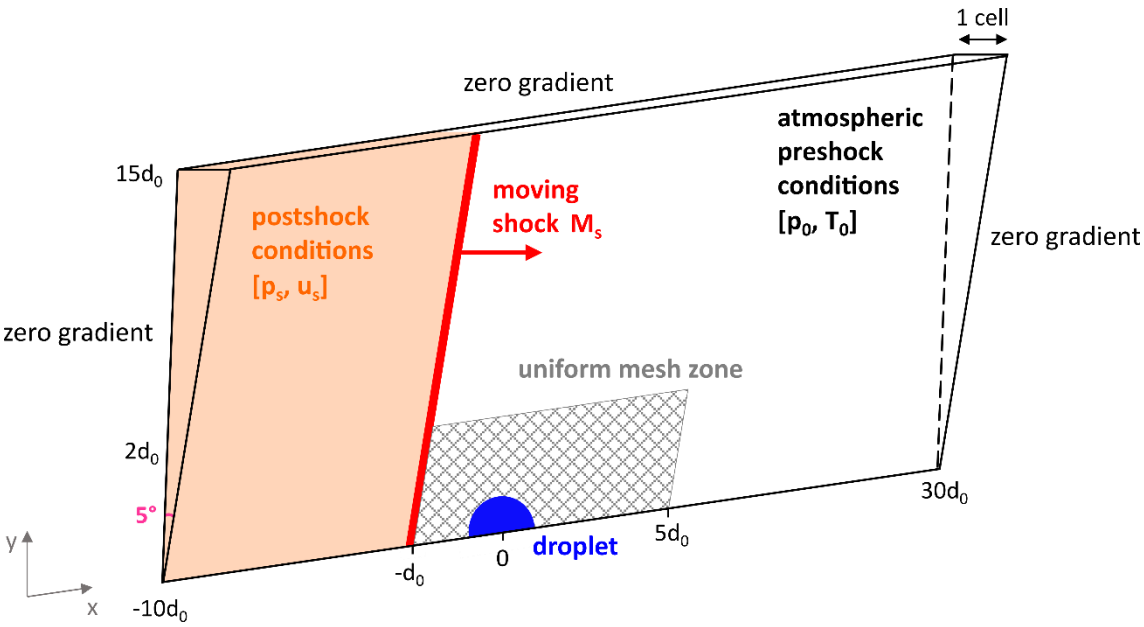


**Figure 3.1** Initial configuration and information regarding the computational mesh for the simulation of droplet aerobreakup.

DNS studies in the literature [10], [151] utilized a computational mesh of more than 1000 cells per diameter to solve the viscous boundary layer and predict the Kelvin-Helmholtz instabilities. However, due to the significant computational cost, these DNS studies are restricted to the demonstration of the early-stage instabilities on the coherent droplet surface and do not examine the later-stage fragmentation and mist development, which is the main objective of the current simulations. On the contrary, the utilized spatial resolution of 100 and 200 cells per original diameter is commonly selected in the literature, indicatively in [134], [24], [149], [152], and is proven to capture accurately the macroscopic deformation of the coherent droplet surface, while the investigation of the Kelvin-Helmholtz instabilities remains out of scope in the present study.

The two characteristic scales that determine the onset of the droplet aerobreakup under the SIE regime are the characteristic viscous velocity $u_V^+ = \frac{\nu_l}{d_0} \cong 9 \times 10^{-6} m/s$ and the characteristic capillary velocity $u_C^+ = \sqrt{\frac{\sigma}{d_0 \rho_l}} \cong 0.12 m/s$, as defined by Theofanous [5]. The viscous velocity is related with the unresolved Kelvin-Helmholtz instabilities inside the viscous boundary layer, while the capillary velocity balances the stripping actions of the developed wake on the droplet surface and the surface tension force that restrains the liquid detachment. With respect to the turbulence characteristic scales, the Kolmogorov velocity scale is around ~0.1m/s in subsonic case 1 and it rises to ~1m/s in supersonic case 3. At the same time, the produced secondary

droplets inside the mist have diameters in the range of 0.01μm to 19μm, while the Kolmogorov length scale is of the order of ~0.5μm in the three examined cases. Therefore, turbulence effects are becoming more significant under supersonic post-shock conditions and are responsible for the breakup of the smallest-scaled droplets.

In the present simulations, the flow turbulence is considered using LES modelling with the implementation of the one-equation SGS model of Lahey [93]. However, the utilized 2D axisymmetric geometry with one cell thickness in the azimuthal direction imposes limitations regarding the accurate capturing of the turbulent state, which corresponds to fully 3D-developed phenomena. Specifically, the simulation is initialized without turbulence in the flow field and thus, the instantaneous velocity field is 2D. Therefore, in the absence of developed turbulence or a developed turbulent boundary layer at the initial conditions, the LES approximation can be applied in the present geometry of one cell thickness in the azimuthal direction without significant limitations. Additionally, Stefanitsis et al. [158] depicted that the assumption of a symmetrical flow field around the deforming droplet under the influence of turbulence and vortex shedding does not affect the shape of the coherent droplet; however, it can have an influence on the trajectory and the breakup time of the fragments. Hence, the present axisymmetric geometry can adequately predict the coherent droplet deformation and fragmentation with minor limitations regarding the produced fragments motion due to the absence of the stochastic character of a fully developed turbulent field. At the same time, key numerical studies in the literature [134], [143], [24], [10], [146] exclude the consideration of turbulence effects, without a limitation in capturing the dominant macroscopic phenomena of the aerobreakup evolution, while DNS studies [134], [151] do not report any significant difference or previously unrevealed mechanisms in the flow field due to the resolved turbulence. Consequently, despite the discussed limitations, the utilized 2D axisymmetric geometry with one cell thickness in the azimuthal direction is an acceptable compromise between an adequate turbulence model and a viable computational cost.

Regarding the numerical simulation set-up, the spatial discretization used is based on second-order accurate discretization schemes. Time stepping is performed adaptively during the simulation to respect the selected limit for the convective Courant–Friedrichs–Lewy (CFL) condition of 0.2. Finally, the thermodynamic closure of the system is achieved by implementing the stiffened gas equation of state, proposed by Ivings et al. [94], for the liquid phase and the ideal gas equation of the state for the gaseous phase, which can perform adequately even under supersonic post-shock conditions, as shown in Hébert et al. [134].

## 3.3 Results and Discussion

The numerical investigations of the droplet aerobreakup using the proposed multiscale two-fluid approach are presented for the three cases of Table 3.2 in Figures 3.2, 3.3, 3.4, respectively and compared with the corresponding experimental observations of Theofanous [5] and Theofanous et al. [4]. Following the pass of the shock wave, the small-scale interfacial instabilities on the droplet surface and the pressure differences between the upstream and downstream side of the droplet impose a gradual deformation of the initially spherical droplet into a flattened shape. The deforming coherent droplet interface is captured using the VOF method and illustrated with red isolines in Figures 3.2(i), 3.3(i), 3.4(i). As it can be observed for the three simulated cases, the macroscopic deformation of the coherent droplet interface shows a good qualitative agreement with the experimental results, following satisfactorily the spanwise expansion and the flattening of the backside of the droplet.

At the same time, the large-scale droplet deformation is followed by an extended fragmentation, which initiates due to liquid stripping from the droplet surface and results in the formation of a dispersed mist of microscale structures. The produced mist is simulated within the diffuse interface formulation of the multiscale framework, while numerical models are introduced for consideration of the unresolved sub-grid scale phenomena. Specifically, during the early stages of aerobreakup, liquid stripping is observed initially from the droplet equator and later from the backside of the droplet with the two streams to collide into a primary stream and form a widespread mist, as shown in Figures 3.2(i), 3.3(i), 3.4(i) and previously discussed in the study of Liu et al. [10]. The main stripping mechanism, which is responsible for the production of the primary stream, is enhanced by the growing vortices formed on the backside of the droplet; the vortices interact with the droplet surface and enhance the existing mist with additional fragments, as illustrated in Figures 3.2(iv), 3.3(iv), 3.4(iv). Even though the near-stagnation region remains relatively flat, as observed in the experimental visualizations of Theofanous [5] and Theofanous et al. [4], a secondary stream of fragments is detached from the frontside of the droplet. Unlike the main stripping mechanism, which is dominated by the local flow vorticity, the secondary stripping mechanism is acting on the high-pressure side of the droplet and is driven by the interfacial instabilities on the droplet surface, the strong shear, and the aerodynamic conditions around the droplet. As a result, the produced secondary stream is more pronounced with an increase of the incident shock wave Mach number, as observed in Figure 3.4(i), since the supersonic post-shock conditions impose higher local pressure and gas stream velocities and thus,

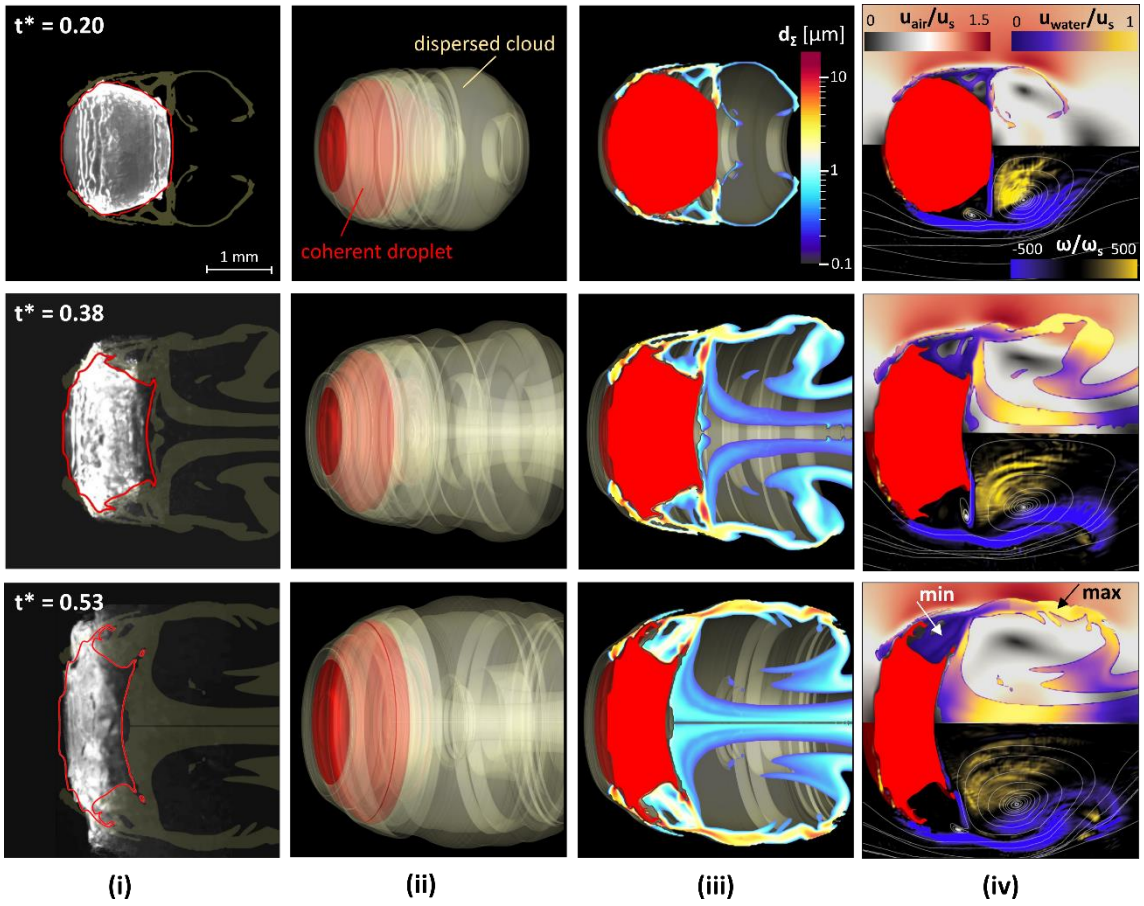


**Figure 3.2** Droplet aerobreakup in case 1. (i) Comparison between the experimental visualizations of Theofanous et al. [4] (t*=0.20, 0.38) and Theofanous [5] (t*=0.53), the simulation results of the deforming coherent droplet (red iso-line for water volume fraction value 0.5) and the produced water mist (yellow iso-surface for water volume fraction values higher than $10^{-5}$) (ii) 3D reconstructed results (iii) Dimensions of the secondary droplets inside the mist (iv) Air and water velocity magnitudes (top) and vorticity streams (bottom).

amplify the aerodynamic forces on the frontside of the droplet. Finally, the primary and secondary streams of fragments merge, following the free-stream gas flow and the aerodynamic force imposed by the upstream and downstream pressure differences, and create a dense mist layer around the deforming droplet in consistence with the experimental observations. At the late stages of fragmentation, secondary structures continue to detach from the surface of the elongated but still coherent body of the deformed droplet, while the penetration and dispersion of the produced mist dominate the breakup mechanism.

The dimensions of the produced droplets inside the dense mist are obtained in coherence with the evolution of the interface surface area, considering turbulence, droplet collision and coalescence,

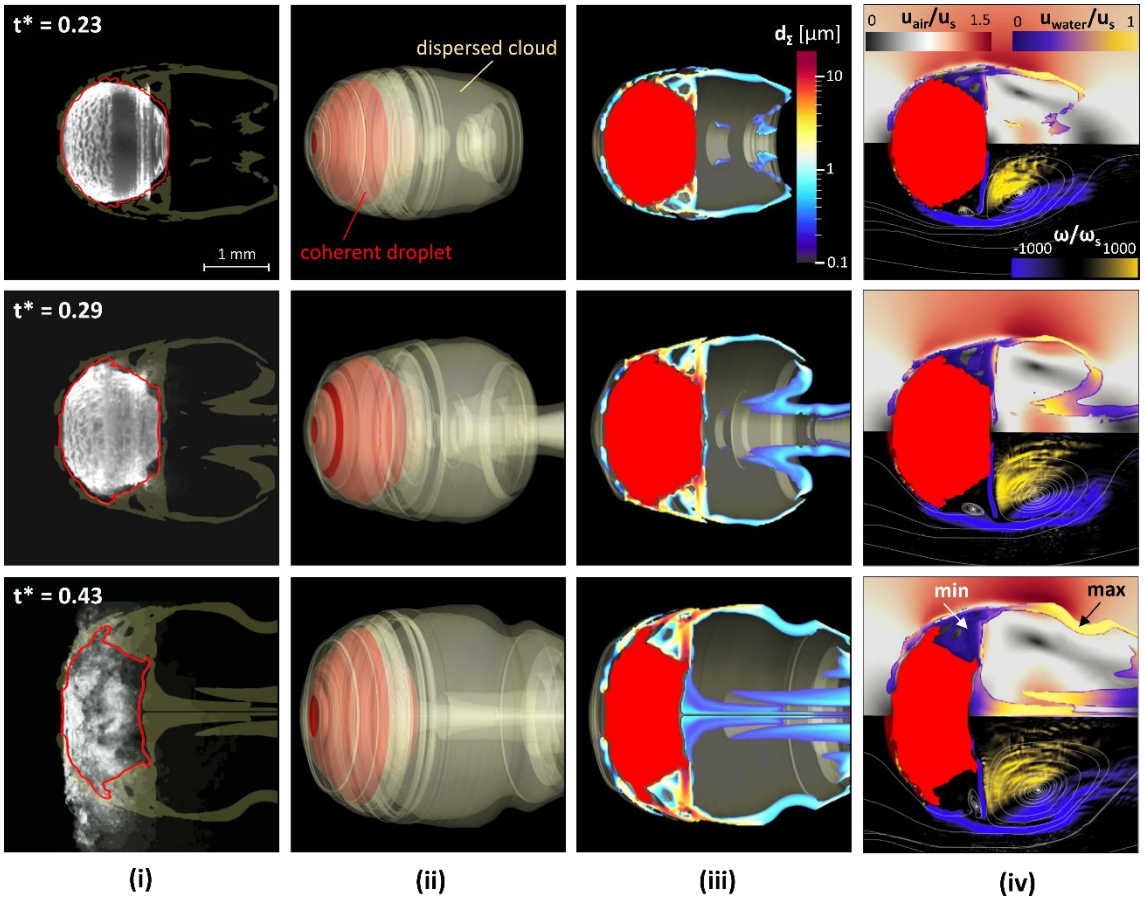


**Figure 3.3** Droplet aerobreakup in case 2. (i) Comparison between the experimental visualizations of Theofanous et al. [4] (t*=0.23) and Theofanous [5] (t*=0.29, 0.43), the simulation results of the deforming coherent droplet (red iso-line for water volume fraction value 0.5) and the produced water mist (yellow iso-surface for water volume fraction values higher than $10^{-5}$) (ii) 3D reconstructed results (iii) Dimensions of the secondary droplets inside the mist (iv) Air and water velocity magnitudes (top) and vorticity streams (bottom).

and secondary breakup effects within the multiscale framework. The largest secondary droplets with a maximum diameter of 19μm are detected close to the coherent droplet and on average around the droplet equator and the droplet flattened backside, as illustrated in Figures 3.2(iii), 3.3(iii), 3.4(iii). Thus, based on the liquid stripping mechanism, the largest captured secondary droplets are detached from the coherent droplet under the influence of the main stripping mechanism and are embedded in the primary stream of fragments. Additionally, in the supersonic case 3 in Figure 3.4(iii), significantly large droplets close to the maximum diameter are also observed on the droplet frontside during the later stages of fragmentation, when the secondary stripping mechanism contribution to the overall droplet aerobreakup is remarkable. The maximum diameter is correlated with the local mesh resolution for a mesh of 100 cells per initial diameter and thus, the size limit for structures that can be resolved with the VOF method. Details about the

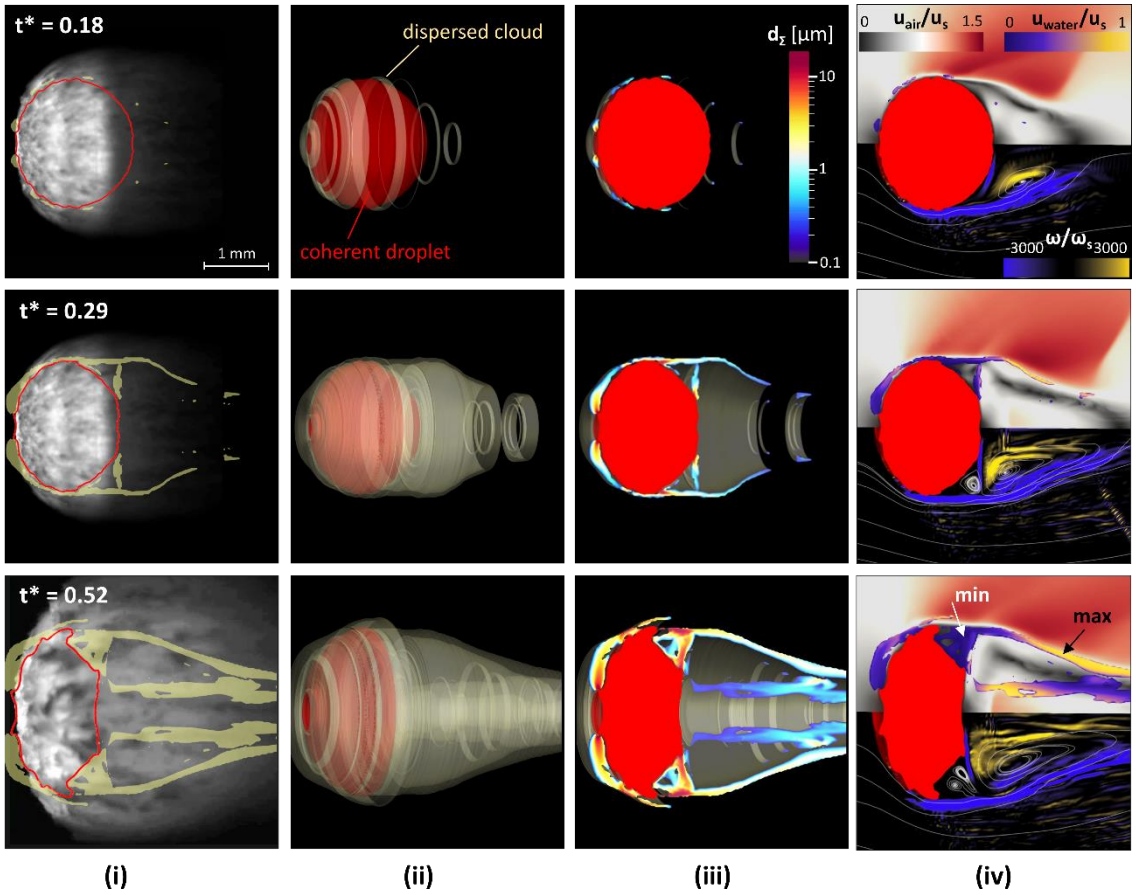


**Figure 3.4** Droplet aerobreakup in case 3. (i) Comparison between the experimental visualizations of Theofanous et al. [4] (t*=0.18, 0.29) and Theofanous [5] (t*=0.52), the simulation results of the deforming coherent droplet (red iso-line for water volume fraction value 0.5) and the produced water mist (yellow iso-surface for water volume fraction values higher than $10^{-5}$) (ii) 3D reconstructed results (iii) Dimensions of the secondary droplets inside the mist (iv) Air and water velocity magnitudes (top) and vorticity streams (bottom).

upper limit of the sub-grid diameters with respect to the local grid resolution are presented in Appendix 3.A. In the review study of Pilch & Erdman [120], the largest fragments detached from the droplet equator are approximately one to two orders of magnitude smaller than the original droplet, which is in agreement with the newly detached fragments captured by the multiscale two-fluid approach. At the same time, the smallest sub-grid scale droplets observed downstream have diameters in the range of 0.01μm to 0.1μm, without the numerical model to impose a lower diameter limit. These micro-scale droplets are visible as a cloud but cannot be quantified in the experiment and thus, there is no experimental input for the smallest droplet sizes. However, the significant extend of the secondary droplets interactions inside the dense mist can justify the production of the detected smallest sizes, while the exclusion of vaporization effects from the

performed simulations can be related with the possible longer-term presence of the smallest secondary droplets inside the dense mist. During the earlier stages of aerobreakup, the small-scale secondary droplets with diameters below 1μm are mostly observed downstream at the edges of the forming mist. Later, these are trapped inside the extended mist that continuously increases in volume and recirculates behind the deforming droplet.

A driving mechanism for the aerodynamically imposed breakup and characteristic feature of the water dispersion evolution is the recirculation of the produced secondary droplets within the water mist. As depicted in Figures 3.2(iv), 3.3(iv), 3.4(iv) and discussed in the simulations of Meng & Colonius [24], the interaction of two counter rotating vortices is the key mechanism for the formation of a dominant wake recirculation region behind the deforming droplet. In the course of fragmentation, more secondary vortices with varying length scales and spatial arrangement form in the wake between the convex frontside and the flattened backside of the coherent droplet and are responsible for its deforming shape. Focusing on the effect of the propagating shock wave on the dynamics of the produced water mist, an increased Mach number results in a post-shock flow with an extended streamwise but relatively limited spanwise recirculation zone behind the droplet, as illustrated in Figures 3.2(iv), 3.3(iv), 3.4(iv). The free-stream gas velocity shows similar behaviour irrespectively of the Mach number with maximum values up to 1.5 times the initial post-shock velocity, observed in the region above the droplet equator and extending downstream along the negative vorticity side of the primary wake. At the same time, the secondary droplets that are subject to a vortical flow show maximum and minimum velocity values in anti-diametrical positions along the primary recirculation region independent of the underlying droplet sizes. As highlighted in Figures 3.2(iv), 3.3(iv), 3.4(iv), the maximum velocity values are observed for the secondary droplets located along the upper and lower side of the primary wake, while the minimum velocity values are found above the droplet backside and downstream on the right side of the primary wake. Following the dominance of the vortical mechanism over time, the maximum velocity values among the secondary droplets gradually increase, until they reach or even slightly exceed the gas steam velocity values at the initial post-shock conditions, namely 110.87m/s, 224.97m/s and 654.9m/s, for cases 1, 2 and 3, respectively. While the minimum velocity values in the droplets' recirculation region approach zero, the newly detached fragments from the backside of the droplet do not remain stagnant. Nevertheless, they are embedded in the primary stream of fragments that is continuously enhanced and governed by the developed flow vorticity.

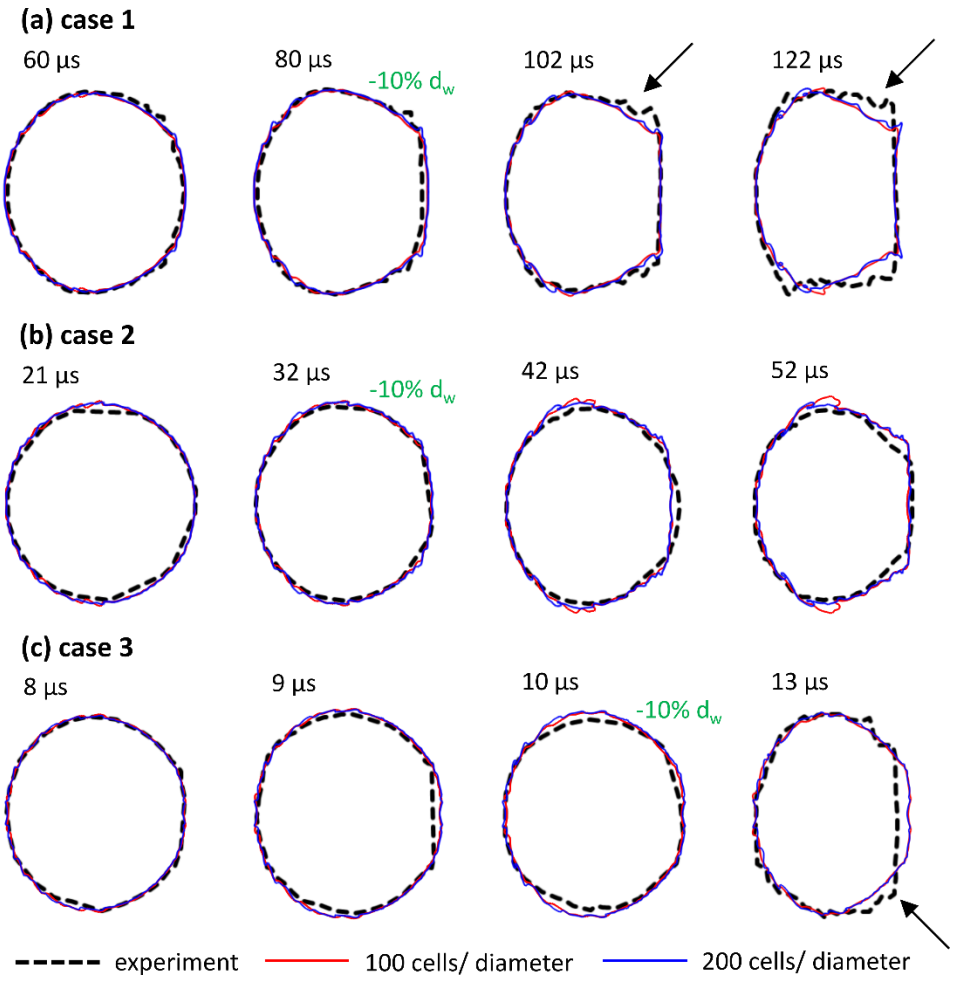


**Figure 3.5** Coherent droplet isolines. Comparison between the experimental isolines of Theofanous et al. [4] (black dashed line) and the simulation isolines for volume fraction value 0.5 using a computational mesh with 100 (red solid line) and 200 (blue solid line) cells per initial droplet diameter. The arrows point to the small deviations between the experimental and simulation isolines.

Focusing on the early-stage deformation in Figure 3.5, the droplet surface isolines, obtained from the experimental results in the work of Theofanous et al. [4], are compared against the numerical isolines for two different mesh resolutions of 100 and 200 cells per initial droplet diameter. The droplet surface deformation is adequately predicted by the conducted simulations and only minor deviations from the experimental isolines are observed on the tip of the flattened backside of the droplet, where the numerical method already detects detached fragments, as depicted in Figures 3.2, 3.3, 3.4. Additionally, the good agreement between the simulation results with the utilization of a coarse and a fine computational mesh demonstrates that a moderate mesh resolution of 100 cells per initial diameter is sufficient to resolve the large-scale droplet deformation. The sharpness of the numerical solution is examined in Figure 3.6, obtaining the droplet surface isolines from

different values of the liquid volume fraction and considering more advanced droplet deformation. As illustrated in Figure 3.6, the coherent droplet interface remains sufficiently sharp even at the late stages of aerobreakup. Some minor differences are observed on the upper tip of the deformed droplet interface and the detached large-scale secondary droplets.

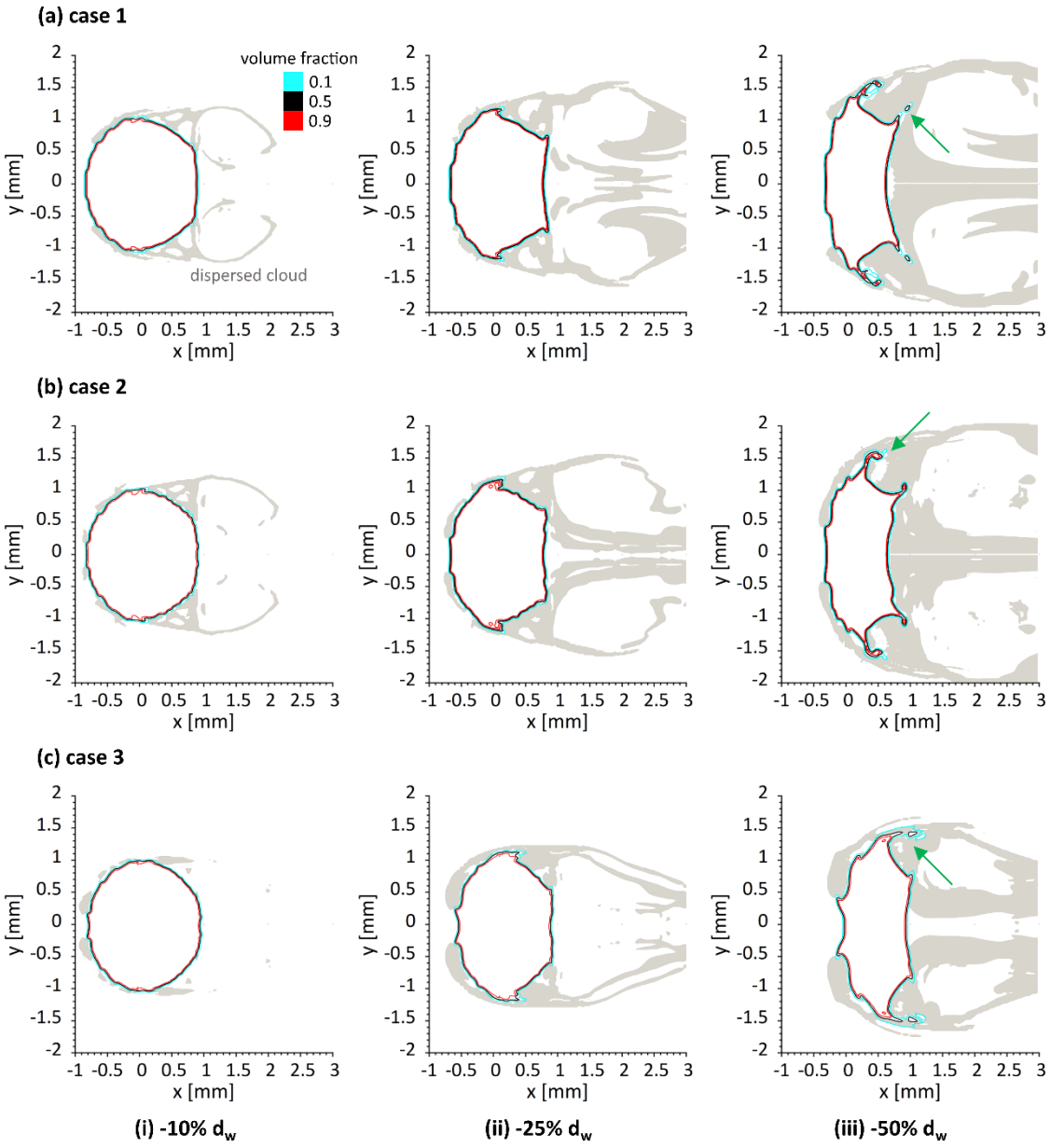


**Figure 3.6** Coherent droplet isolines for different water volume fraction values, using a computational mesh with 100 cells per initial droplet diameter. Produced water mist iso-surface for water volume fraction values higher than $10^{-5}$ (grey). Comparison between cases 1, 2 and 3 at time instances that correspond to a decrease for the width of the deforming droplet by 10%, 25% and 50%. The arrows point to the small deviations in interface sharpness with different volume fraction values.

The intensity of the incident shock wave imposes the occurring post-shock flow conditions and is crucial for the droplet deformation and the consequent water dispersion. In the subsonic case, shown in Figure 3.7(a), when the shock wave with Mach number 1.21 impacts the stagnant droplet, the local pressure increases at approximately 2bar. At the same time, the incident shock wave continues to propagate downstream, and a reflected shock wave is established on the front side of the droplet and initiates its upstream propagation. The developed post-shock flow conditions are characterized by moderate pressure difference around the droplet and maximum local Mach number values at about 0.45. The transonic case of Figure 3.7(b) shows similar behaviour; however, the slower propagation of the reflected shock wave and the higher local Mach numbers lead to a more widespread fragmentation. On the contrary, in the supersonic case of Figure 3.7(c) the strong shock wave with Mach number 2.64 results to a significant increase of the local pressure at 35bar after impact. The subsequent reflected shock wave stabilizes close to the droplet as a detached bow shock. As a result, the flow conditions around the droplet remain supersonic with maximum local Mach number values above 2 that impose a significantly faster and more violent droplet fragmentation, which appears as a very dense and extensive dispersed mist downstream, also observed in the experiments of Hébert et al. [134] for similar Weber numbers.

The widespread water dispersion in the form of a dense mist is the major fragmentation pattern under the SIE regime. An insight into the dimensions of the produced secondary droplets within the mist is presented in Figure 3.8, depicting the volume concentration of different droplet classes over the total volume of the dispersed region, as captured by the numerical model for the three cases in Table 3.2. A significant advantage of the conducted numerical simulations is the consideration of every fluid structure that forms as part of the flow development without excluding of small sizes; thus, providing information for sizes below the 5μm/pixel resolution of the camera utilized in the reported experiments and illustrated in grey colour in Figure 3.8. The first secondary droplets produced in all three cases are small structures, with more than 60% of the diameters in the total volume being below 1μm; these droplets are forming due to the initial liquid stripping from the droplet equator, as observed in the experiments at the very early stages of aerobreakup. Shortly after, the large-scale fragmentation is established when droplets with diameters above 5μm are detached from the coherent droplet surface and thus, an additional class of larger droplets, coloured in grey, is included in the distributions of Figure 3.8 at 42μs, 20μs and 7.1μs for the cases 1, 2 and 3, respectively.

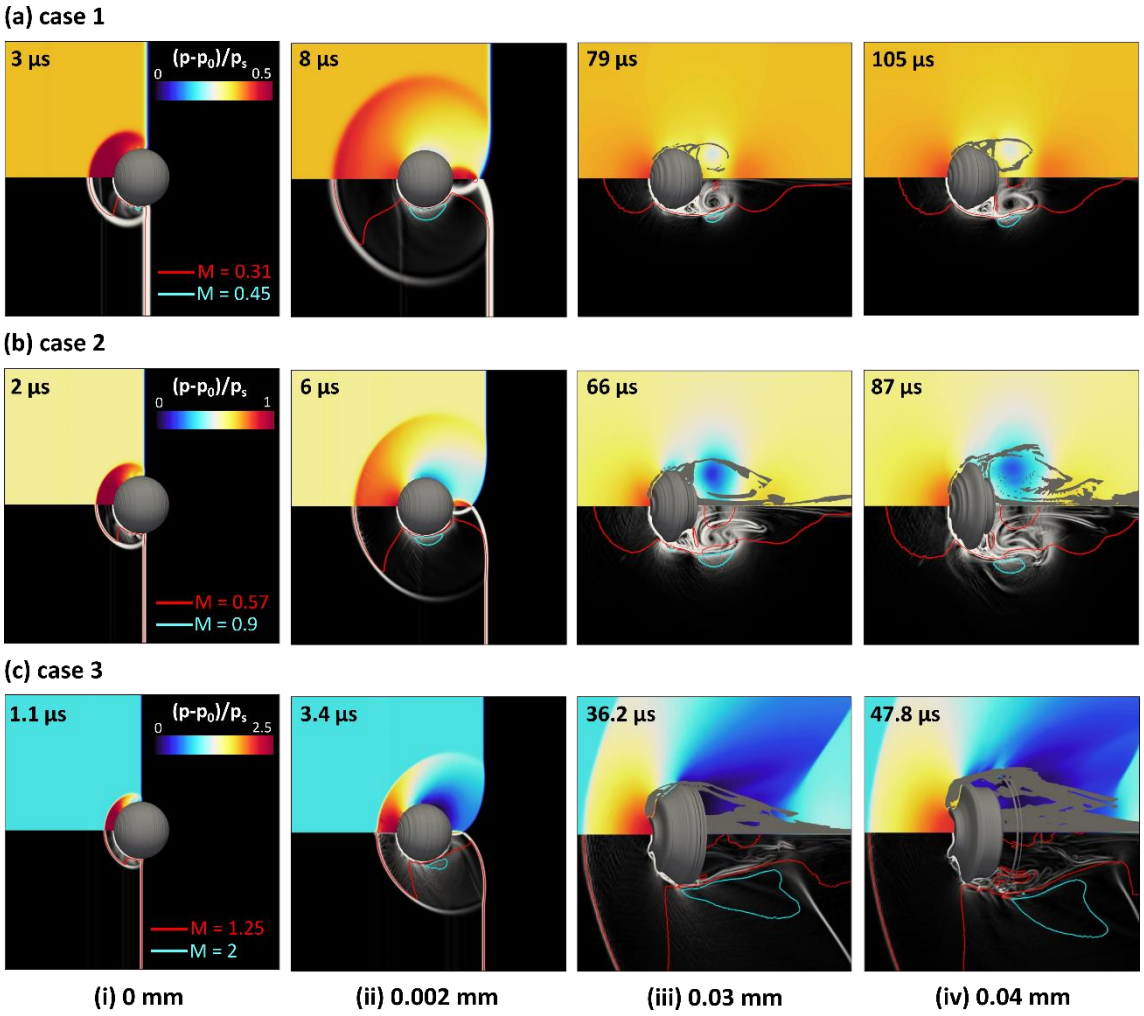


**Figure 3.7** Gas stream conditions during the droplet aerobreakup, while the incident shock wave lies at the same distance from the centre of the droplet. Pressure field and produced water mist evolution (top). Numerical schlieren images and Mach number isolines (bottom).

Considering the evolution of the population of secondary droplets over time, larger droplet sizes above 1μm become more significant in the population with increasing Mach number, as observed in Figure 3.8 for cases 2 and 3. There are two crucial parameters that influence the secondary droplets distribution; firstly, the sizes of the newly detached fragments from the coherent droplet surface and secondly, the sub-grid scale droplet interactions inside the existing dispersed mist. Specifically, an increase of the incident shock wave Mach number imposes a violent droplet fragmentation with extended liquid stripping from the droplet surface due to severe aerodynamic conditions around the droplet and the dominance of the secondary stripping mechanism. As a result, large-scale droplets continue to fragment from the coherent droplet surface and enhance the secondary droplets population even during advanced stages of the aerobreakup process, as

depicted in the distributions of Figure 3.8(ii) and 3.8(iii) for the class of the largest droplets with diameters between 5 and 19μm and also illustrated in Figures 3.3 and 3.4 for indicative time instances.

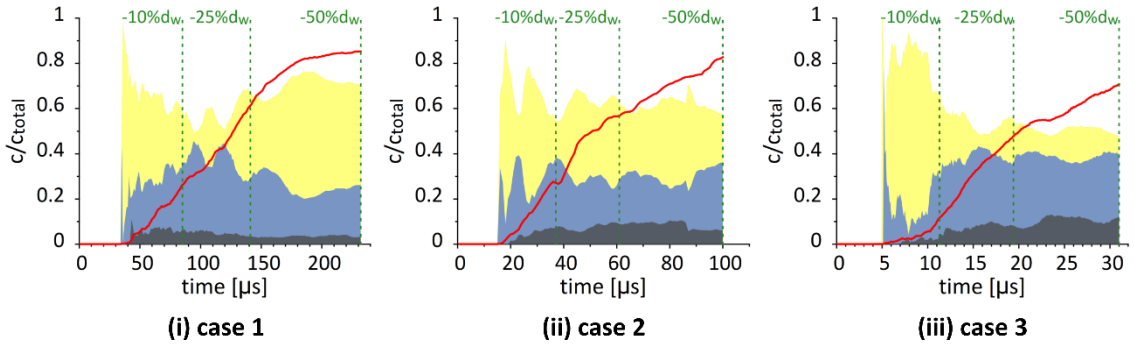


**Figure 3.8** Volume concentration of the secondary droplets with diameters between 5 and 19μm (grey), 1 and 5μm (blue) and lower than 1μm (yellow) over the total volume of the dispersed region. The volume concentration of the dispersed region over the total volume of the water phase is plotted in red. The green vertical lines correspond to a decrease for the width of the deforming droplet by 10%, 25% and 50%.

Following the production of the new fragments, the sub-grid scale droplet interactions are responsible for the further evolution of the secondary droplet sizes inside the dispersed mist. The required sub-grid scale modelling is performed within the multiscale framework using the transport equation for the interface surface area, equation (2.5) in §2; the mechanisms that determine the local interface formation, namely turbulent mixing, droplet collision and coalescence, and secondary breakup effects, are modelled as individual source terms $S_{SGS}$. A positive contribution of the SGS source term corresponds to an increase of the local interface surface area and physically correlates with the evolution of the underlying sub-grid scale droplets into smaller diameters, while a negative SGS source term value describes a decrease of the local interface surface area due to the creation of sub-grid scale droplets with larger diameters. The secondary breakup mechanism can only result in the further breakup of the existing secondary droplets inside the mist and thus, has only a positive contribution in the SGS source term. Details regarding the calculation of the SGS source term are presented in Appendix 3.A.

Figure 3.9 represents the volume concentration of the three sub-grid scale mechanisms that contribute positively on the local interface surface area production and the creation of smaller-scaled droplets, namely the flow turbulence, droplet collision and secondary breakup effects, over the total volume of the dispersed region, as calculated in equation (2.5) for the three examined cases. In case 1, the sub-grid scale turbulence and collision effects contribute to the production of

the local interface surface area by above 90%, already at the early stages of aerobreakup, while the secondary breakup effects, governed by the relative velocity between the liquid and gaseous phases, are absent under the subsonic post-shock conditions. Overall, the predominant pattern is the further decrease of the secondary droplets sizes inside the dispersed mist, which is also reflected in the droplets population in Figure 3.8(i), highlighting an increase and dominance of the smallest scales over time. A distribution of uniformly small-scaled fragments is also demonstrated in the experiments of Wang et al. [133] at subsonic post-shock flows. In case 2, shown in Figure 3.9(ii), the creation of smaller-scaled droplets, driven by the local turbulence and collision, remains dominant for the mist evolution with a minor decrease compared to case 1. Additionally, the secondary breakup mechanism is not completely absent and has a small contribution in the mist dynamics. Therefore, the slightly reduced concentration of the class of droplets with the smallest diameters below 1μm, as depicted in the distribution in Figure 3.8(ii), is a combination of the enhancement of the larger-scaled new fragments under the transonic post-shock conditions and the small decrease of the sub-grid scale interface surface area production.

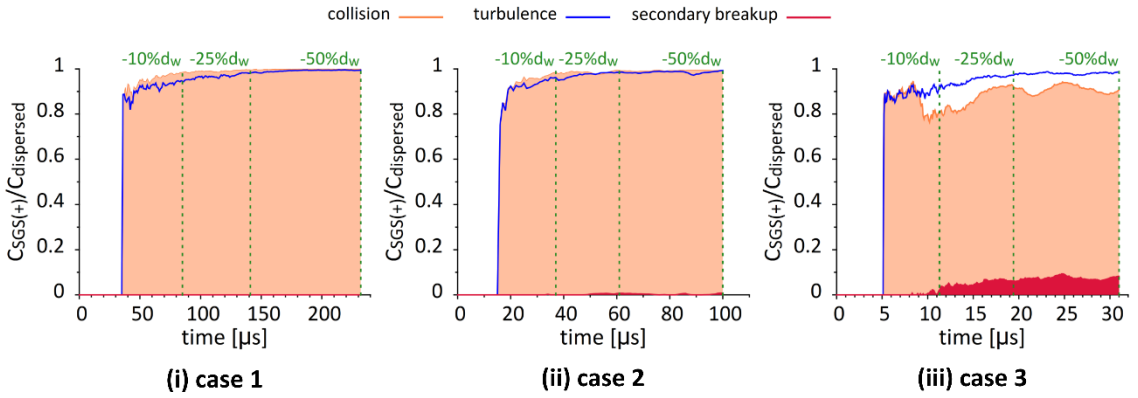


**Figure 3.9** Volume concentration of the sub-grid scale mechanisms, namely turbulence, droplet collision, and secondary breakup, that contribute positively on the local interface surface area production and the creation of smaller-scaled droplets over the total volume of the dispersed region. The green vertical lines correspond to a decrease for the width of the deforming droplet by 10%, 25% and 50%.

Finally, case 3, presented in Figure 3.9(iii), demonstrates the significant influence of the supersonic post-shock conditions on the sub-grid scale mechanisms. Specifically, even though the flow turbulence maintains a major positive contribution on the production of smaller-scaled droplets, the collision effects are remarkably reduced by coalescence that becomes significant after the early stages of aerobreakup, even before the width of the deforming droplet is decreased by 10%. The coalescence of the secondary droplets enhances the droplet population with larger-scaled droplets and explains the decreased concentration of the droplet class with the smallest

diameters, observed approximately after 10μs in Figure 3.8(iii). As illustrated in Figure 3.10, coalescence effects are present in the region of the main stripping mechanism, namely close to the droplet equator and the backside of the deforming droplet. During the evolution of aerobreakup, the coalescence region expands, driven by the increasing local flow vorticity. Similarly, in the study of Wang et al. [133], the presence of larger fragments among the dominant micro-droplets is observed at the advanced stages of aerobreakup under supersonic post-shock conditions. As discussed in [133] and in agreement with the present sub-grid scale analysis, these non-uniform fragments coalesce into larger secondary droplets, as imposed by the local flow conditions and the limited spanwise spread on the produced dense mist. At the same time, the secondary breakup shows a considerable and gradually increasing contribution on the mist evolution over time, as depicted in Figure 3.9(iii). The secondary breakup mechanism is mainly established on the droplet frontside, shown in Figure 3.10, where the secondary stripping mechanism dominates and the relative velocity between the newly detached droplets and the supersonic gas flow locally exceeds the value of 200m/s. However, the secondary breakup of sub-grid scale droplets is not contributing significantly on the increase of the population of the smallest droplets, since it involves on average the breakup of large-scaled droplets with diameters above 2μm, as demonstrated in Figure 3.10 for the time instances that correspond to a decrease for the width of the deforming droplet by 10%, 25% and 50%.

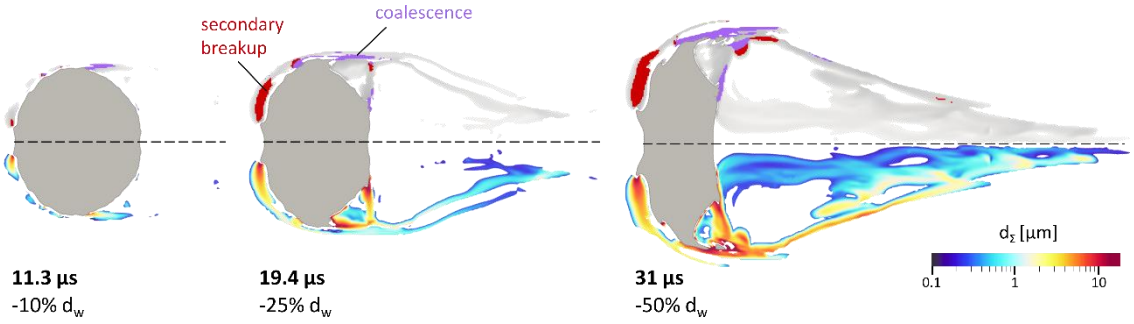


**Figure 3.10** Droplet aerobreakup in case 3 at time instances that correspond to a decrease for the width of the deforming droplet by 10%, 25% and 50%. Regions in the dispersed mist where the droplet coalescence (purple) and secondary breakup (red) are present (top). Dimensions of the secondary droplets inside the mist (bottom).

Lastly, the volume concentration of the water mist over the total volume of the water phase is reduced by approximately 10% in case 3 compared to the lower Mach number cases 1 and 2 for the same width deformation, as shown in Figure 3.8(iii). At the early stages of aerobreakup, the limited mist concentration is related with the postponed breakup initiation, also observed in the experiments of Wang et al. [133] at supersonic post-shock conditions. However, at the later stages

of aerobreakup, the stripping mechanism becomes more significant under the influence of both the main and the secondary stripping mechanisms, depicted in Figure 3.6 in comparison with cases 1 and 2, leading to an extended and violent stripping from the coherent droplet surface. On the contrary, during the later stages of the aerobreakup process, the mist dynamics, governed by the modelled sub-grid scale mechanisms, play a major role in the evolution of the dispersed mist. In particular, as highlighted in Figure 3.9(iii) and discussed previously, the remarkable coalescence effects result in the destruction of the local interface surface area and thus, act against the further expansion of the existing mist. At the same time, the violent fragmentation under the supersonic post-shock conditions along with the increasing flow vorticity behind the deforming droplet impose the mist into a rapid downstream penetration. Therefore, the expansion of the dispersed mist in the spanwise direction is restricted compared to the cases with lower Mach numbers due to the severe gas stream conditions. Likewise, in the experiments of Wang et al. [133] a significantly narrower mist expansion is observed at supersonic conditions. In conclusion, the supersonic post-shock conditions impose the development of a relatively reduced mist with the significant presence of larger-scaled droplets until the advanced stages of aerobreakup.

## 3.4 Summary

The aerodynamic breakup of a water-like droplet under the SIE regime, imposed by three different shock waves with Mach numbers 1.21, 1.46 and 2.64, has been investigated using the developed multiscale two-fluid approach. The present numerical study provided the opportunity to verify the physical mechanisms of aerobreakup and scrutinize aspects of the process that were not evident in the experimental visualizations of Theofanous [5] and Theofanous et al. [4], using a physically consistent methodology with a viable computational cost. Specifically, the deformation of the coherent droplet interface was fully resolved by the local mesh resolution using the VOF sharp interface method, while the produced mist of secondary fragments was modelled under the diffuse interface approach with consideration of sub-grid scale phenomena, namely turbulent mixing, droplet collision and coalescence, and secondary breakup effects.

During the early-stage mist development, two stripping mechanisms were identified to act on the coherent droplet surface. The main stripping mechanism is responsible for the formation of the primary stream of fragments, detached from the droplet equator and the droplet flattened backside, while the secondary stripping mechanism is present on the droplet frontside and becomes more significant at supersonic post-shock conditions. The largest detached fragments were observed on

average on the locations of the local liquid stripping and subsequently, the fragments sizes evolve inside the mist, following the gas stream flow evolution. The post-shock flow conditions and the development of a dominant recirculation region behind the deforming droplet play a major role in the formation and expansion of the produced mist. In a supersonic post-shock flow, the dispersed mist appears relatively narrower, due to severe aerodynamic conditions that establish a rapid downstream penetration.

For the first time in the up-to-date literature, details for the secondary droplets' population and the evolution of the droplets sizes inside the mist were obtained and analysed based on the modelled sub-grid scale phenomena and the local flow development. At supersonic post-shock conditions, the coalescence and secondary breakup mechanisms become more pronounced. Additionally, the droplet size distribution is enhanced with larger-scaled droplets even at the later-stages of aerobreakup. As a result, the limited mist concentration under supersonic post-shock conditions is an outcome of the restricted spanwise expansion of the produced mist and the enhancement of the sub-grid scale interface destruction mechanisms inside the mist.

Future research of DNS simulations, which include the investigation of the produced fragments, can provide a valuable quantitative validation for the present droplets' population. Additionally, three-dimensional simulations, using the proposed multiscale two-fluid approach, could be appropriate to reveal more details and mechanisms of the mist dynamics and to consider the significance of three-dimensional phenomena, such as turbulence and vortex shedding, in the droplet aerobreakup.

# 3.A Validity of Closure Models and Numerical Limitations

Modelling limitations may arise in the developed numerical method due to the introduction of closure relations for the source terms in the governing equations, the sub-grid scale modelling, the switching criteria within the multiscale framework and the absence of a quantitative validation for the produced mist. The validity of the utilized models and the imposed assumptions is discussed below, considering specifically the present simulations of droplet aerobreakup and the examined flow conditions.

**3.A1)** The closure of the interfacial interaction terms, which appear in Navier-Stokes equations after the imposed averaging procedure and consider the mass, momentum, and energy exchange phenomena between the interacting phases, is an inherent modelling requirement of the two-fluid model formulation. In the present simulations, the applied closure relations are consistent with the examined flow conditions, as discussed below.

**3.A1.1)** In continuity equations (2.1) in §2, the interfacial mass source term, which models the mass transfer due to phase-change phenomena, namely cavitation and vaporization, is neglected.

- Cavitation plays a minor role at the early stages of aerobreakup in the examined cases. Specifically, as depicted in Figure 3.11, in cases 1 and 2 the shock wave propagation evolves smoothly downstream without any significant decrease in the local pressure inside the droplet, that can be related to the development of cavitation regions. On the contrary, in the supersonic case 3, the strong shock wave with Mach number 2.64 results to an increase of the local pressure at 35bar after impact. At 1.5μs the propagating shock wave inside the droplet is reflected normal to the droplet outer surface and an expansion wave is created. When the shock wave reaches the backside of the droplet, it partially reflects backwards, and a low-pressure region is formed at 2.5μs. Similarly, the experimental observations of Sembian et al. [144] depict the creation of cavitation bubbles and the subsequent decrease of the low pressure region in the aerobreakup of a water column under supersonic conditions. Despite the cavitation development, an early fragmentation, initiating from the backside of the droplet due to cavitation bubbles collapse, is not observed in the simulation results; the experimental visualizations of Theofanous et al. [4] also confirm the absence of any distinguishable surface oscillations or breakup on the backside of the droplet that can be related to significant cavitation effects.

Since the early stages of the droplet aerobreakup evolution are not driven by cavitation and the minor cavitation region has no macroscopic effect on the droplet fragmentation under the examined conditions, a model for nucleation and subsequent growth of the cavitating bubbles has not been implemented in the numerical framework. Instead, in the supersonic case 3, a very small volume fraction of air of the order of $10^{-6}$, which corresponds to a typical nucleation volume fraction [159], is introduced in the initial droplet volume fraction. Under this assumption, the small gaseous volumes inside the droplet will expand after the significant pressure drop, producing expansion similar to those that would occur with cavitation; with the subsequent pressure increase, the gaseous volume gradually collapses although any condensation and the pressure overshoot effects due to complete vapour collapse (which is not the case with the gas content) are not considered.

- Vaporization modelling is neglected since the local liquid temperature does not increase more than 10K during the shock wave impact on the droplet in the examined cases. However, vaporization effects can be responsible for the extended water dispersion observed at the later stages of aerobreakup under the supersonic post-shock conditions of case 3; thus, vaporization could be considered in future research of aerobreakup imposed by high Mach number shock waves.

- Other mass exchange contributions with an effect on interface formation are considered in the transport equation for the interface surface area density Σ, equation (2.5) in §2.

**3.A1.2)** In momentum equations (2.2) in §2, the interfacial momentum source term accounts for the aerodynamic drag force, which dominates among the other interfacial forces acting between the dispersed droplets and the free-stream gas flow during the aerobreakup process, due to the severe aerodynamic conditions imposed by the upstream and downstream pressure differences. The aerodynamic drag force is defined as $F_D = \frac{1}{2} C_D \rho_{gas} u_r |u_r| A_{droplet}$. The calculated drag coefficient $C_D$ [106] is validated for a vast range of Reynolds numbers and here it is defined based on the local flow properties. The reference area of the droplet $A_{droplet}$ is calculated based on the local interface surface area density Σ. The velocity fields are accurately predicted in the performed simulations, since a good agreement between the simulation and experimental results is observed with respect to the overall aerobreakup evolution and the liquid penetration; thus, the relative velocity $u_r$ can be precisely extracted from the two-fluid model.

**3.A1.3)** In energy equations (2.3) in §2, the interfacial energy source term is modelled via a standard heat transfer law [160] for the calculated temperature fields of the liquid and gaseous phases. In the present simulations, the observed temperature differences between the liquid and gaseous phases on interfacial regions can locally reach the absolute value of 35K in subsonic case 1, almost 90K in transonic case 2 and can even exceed the absolute value of 500K in the bow shock region in supersonic case 3. Therefore, the modelling of thermal effects is becoming crucial for the accurate capturing of aerobreakup under high Mach numbers.

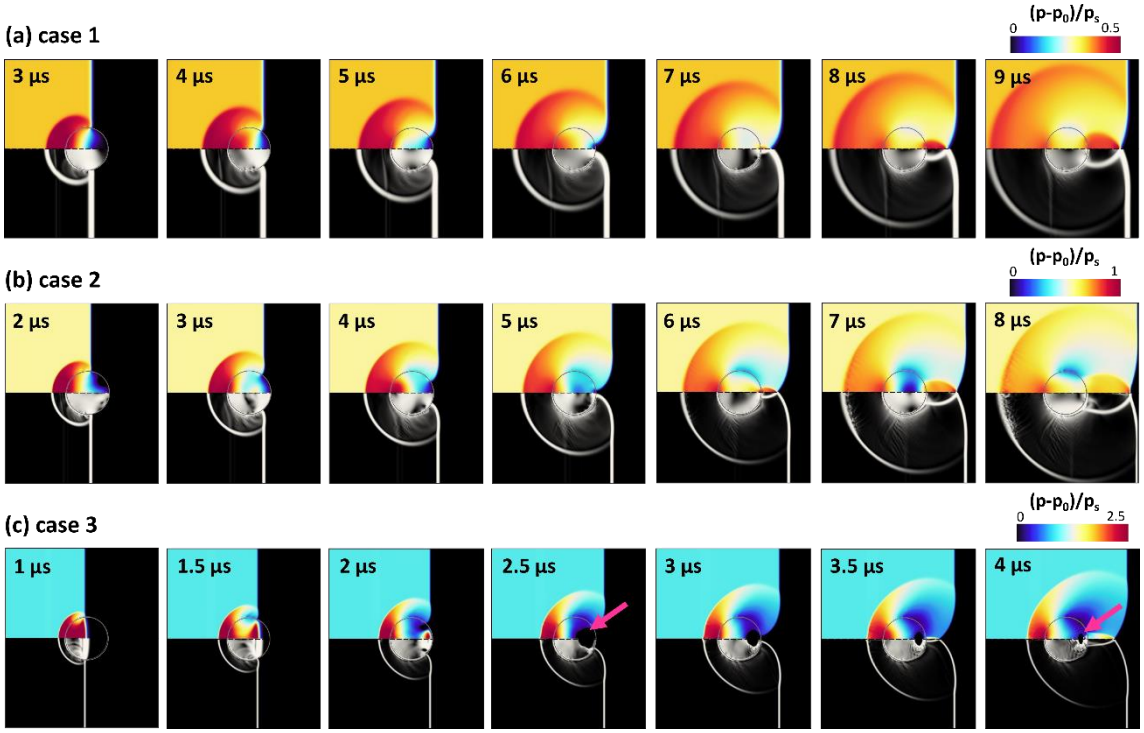


**Figure 3.11** Compressibility effects at the early stages of aerobreakup, namely the incident shock wave downstream propagation, the reflected shock wave in the free gas stream and the transmitted shock wave into the liquid droplet. Pressure field (top) and numerical schlieren images (bottom).

**3.A2)** A fundamental principle of the multiscale two-fluid approach is the sub-grid scale modelling of unresolved flow structures via the transport equation for the interface surface area density Σ, equation (2.5) in §2. The physical mechanisms, which are responsible for the interface production and destruction, and which fall below the local mesh resolution, are considered in equation (2.5) as the sub-grid scale source term $S_{SGS}$. Specifically, the contributions of turbulent flow stretching and wrinkling, along with the sub-grid scale droplet interactions, involving droplet collision and coalescence, and secondary breakup effects, are taken into account with the appropriate closure relations, summarized in Table 2.1. The SGS models are a function of the

characteristic timescale $\tau_{SGS}$ and the critical interface surface area density $\Sigma^*_{SGS}$ at an equilibrium state between interface production and destruction. The modelling assumptions and the validity of the SGS models are discussed below.

- The turbulence term utilizes the Kolmogorov timescale. The accurate closure of the critical Weber number $We^*_{turb}$ [55], which expresses the balance between the liquid kinetic energy and the liquid surface energy at equilibrium state, requires a case-dependent calibration using DNS results. However, considering the significant computational cost, a viable compromise is to set the critical Weber number value equal to 1, even though it may result to a minor underestimation of the effect of turbulence on interface formation, as shown in the DNS study of Duret et al. [161] for the primary atomization of a subsonic spray.

- The collision and coalescence model is based on the particle collision theory [55]. The major assumption concerns the characteristic velocity of collision between the colliding droplets, which is described as a function of the turbulent kinetic energy and has been used in subsonic liquid spray atomization simulations [55], [162]. Due to the lack of any sufficient information regarding the sub-grid scale particles and since collision is mainly turbulence driven, the proposed model is acceptable in the present simulations.

- The secondary breakup model is based on the model of Pilch & Erdman [120], developed for Weber numbers up to $10^4$. The secondary breakup effects are driven by the mean relative phase velocity [55], which is available within the two-fluid model formulation; thus, the relative velocity is directly obtained from the numerical model without the need of further modelling assumptions.

**3.A3)** The dynamic switching from a sharp to a diffuse interface approach and vice versa, following the implemented criteria in the flow topology detection algorithm, is bounded by the local mesh resolution. In other words, the characteristic dimension, that establishes the resolution capabilities of the multiscale framework and determines which flow structures will be fully resolved and which will be modelled as sub-grid scale phenomena, is an external user-defined parameter. Specifically, in the present aerobreakup simulations, the mesh resolution of 100 cells per initial diameter imposes to droplets with diameters greater than 19μm to be resolved with the sharp interface approach, while the finer mesh of 200 cells per initial diameter allows for more droplets with a minimum diameter of 9.5μm to be captured by the local mesh resolution. However,

even though the upper limit for the secondary droplets' diameters modelled within the diffuse mist is different for the coarse and the fine mesh, the droplets with diameters in the range of 9.5μm to 19μm, which are captured by the fine mesh resolution, are not excluded in the coarse mesh predictions. As shown in Figure 3.12, in the region where the fine mesh detects mesh-resolvable fragments, detached either from the droplet backside or the droplet equator, the coarse mesh identifies the largest-scaled secondary droplets within the diffuse mist.

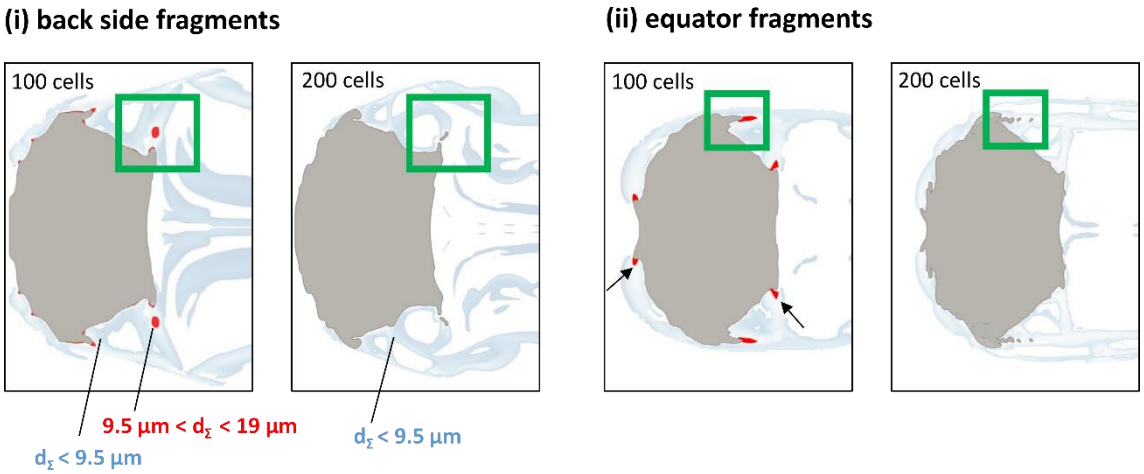


**Figure 3.12** Demonstration of the upper limit for the secondary droplets' diameters modelled within the diffuse mist, using a computational mesh with a resolution of 100 and 200 cells per original diameter. In blue colour are illustrated the secondary droplets inside the mist, captured with both mesh resolutions. In red colour are illustrated the droplets that are modelled inside the mist with the coarse mesh but are resolved by the mesh resolution with the fine mesh, shown inside the green box. The arrows point to areas where the coarse mesh detects fragments due to the unresolved interface sharpness.

This switching mechanism operates well with moderate mesh resolutions in multiscale flows like the droplet aerobreakup problem, in which the sizes of the initial coherent droplet and the firstly formed fragments have a difference of approximately two orders of magnitude. However, in flow fields with structures, covering the complete range between micro-scales to millimetre sizes, the switching mechanisms should be improved. Part of the on-going research is the coupling of an adaptive mesh refinement algorithm with the sharp interface formulation in order to accurately capture the intermediate-scaled structures that are part of the sharp interface formulation, and the original moderate mesh is insufficient to resolve.

Overall, the mesh dependency of the switching criteria does not imply a mesh dependent numerical solution in the aerobreakup simulations. A mesh independence investigation is shown in Figure 3.13, comparing the development of the dispersed region over time for the three

examined cases of Table 3.2, using a computational mesh of 100 and 200 cells per initial diameter. For consistency between the two mesh resolutions, the coarser simulation of 100 cells per diameter includes droplets up to 9.5μm, which corresponds to the local mesh resolution and thus, the upper limit for the dispersed region resolution with the finer mesh. In cases 1 and 2 a very good agreement between the different mesh resolutions is observed, while in case 3 a small deviation of about 10% is noticeable at the early stages of aerobreakup. Considering that any small deviation is enhanced by microscale droplets below 1μm, it is safe to conclude that the proposed numerical method is independent of the computational mesh.

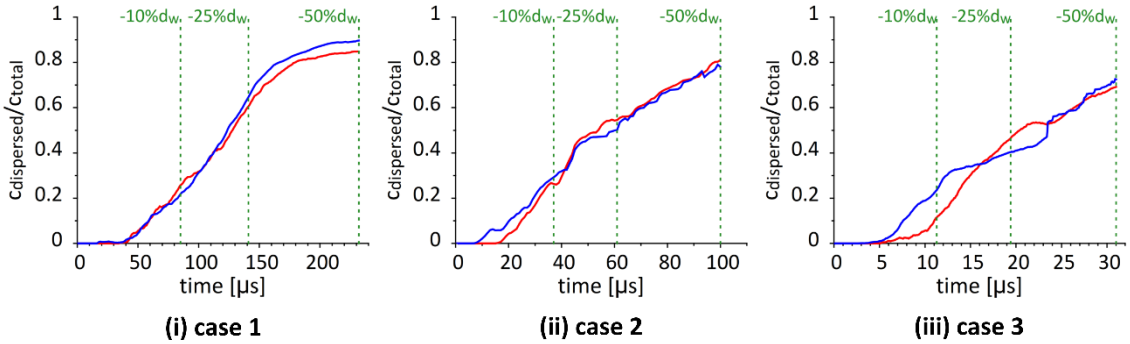


**Figure 3.13** Volume concentration of the dispersed region over the total volume of the water phase for a mesh resolution of 100 (red solid line) and 200 (blue solid line) cells per initial droplet diameter. The green vertical lines correspond to a decrease for the width of the deforming droplet by 10%, 25% and 50%.

**3.A4)** A quantitative validation for the mist dynamics and the sizes of the underlying secondary droplets is restricted by the visualization capabilities inside the dense mist. In the experiments of Theofanous [5] and Theofanous et al. [4], the utilized camera resolution of 5μm/pixel does not allow for the quantification of smaller droplet sizes, which are illustrated as a dilute cloud of undefined and shapeless structures. Thus, the extraction of any information regarding the droplet sizes inside the dense mist is not feasible in the available experimental visualizations. To the best of the authors' knowledge, size distributions for the produced fragments after the droplet aerobreakup are available in up-to-date literature, but only in experimental studies of moderate droplet fragmentation cases [135], [136], [137], [8], [138] in the transition zone between the RTP and SIE regimes. In these cases, the fragments form as a part of a distinguishable liquid trace behind the deforming droplet and not as individual small structures inside a dense and hazy cloud; thus, the visualization of the underlying structures is significantly more pronounced, and a quantitative analysis of the produced fragments is achievable with the use of advanced visualization techniques.

# 4 LASER-INDUCED DROPLET FRAGMENTATION

In the present chapter, the rim fragmentation of a millimetre-sized methyl-ethyl-ketone (MEK) droplet imposed by the impact of different millijoule nanosecond laser beams, that correspond to droplet propulsion velocity values between 1.76m/s and 5.09m/s, is examined. The numerical investigation is conducted within a physically consistent and computationally efficient multiscale framework, using the Σ-Y two-fluid model with dynamic local topology detection. Overall, the macroscopic droplet expansion and the obtained deforming shape show good agreement with the experimental observations. The influence of the laser beam energy on the droplet deformation and the evolution of the detached fragments from the rim is demonstrated. The physical mechanisms that determine the droplet expansion, including the expansion velocity and expansion rate, along with the effect of the surrounding air flow on the detached fragments, are addressed. Despite the visualization limitations inside the polydisperse cloud of fragments in the experimental results at higher laser energy, the evolution of fragments during the fragmentation process is quantified for the first time, and size distributions are obtained within the multiscale framework.

---

*To be published as:

G. Nykteri and M. Gavaises, “Numerical modelling of droplet rim fragmentation by laser-pulse impact using a multiscale two-fluid approach”.

## 4.1 Introduction

The droplet response to a laser-pulse impact is a polyparametric phenomenon, which remains of primary significance in varied state-of-the-art applications of both industrial and medical interest, including, among others, the extreme ultraviolet (EUV) light emission in lithography machines [163], [164], [165], [166], the micromachining in the fabrication of photonic devices [167], [168], [169] and the laser ablation of biological tissues [170], [171], [172], [173]. The absorption of the laser energy by the liquid droplet results in rapid and explosive phase-change phenomena, such as cavitation [174], [175], vaporization [176], [177], [178], and plasma formation [179], [180], observed in both transparent and liquid metal droplets. As a consequence of the developed droplet dynamics after the laser-pulse impact, the droplet moves, deforms, and fragments into different patterns, dependent on the intensity of the applied laser beam energy and the material of the liquid droplet.

Several experimental studies in the literature investigate the laser-imposed fragmentation of a liquid droplet under different experimental configurations, which as a result, lead to different post-impact mechanisms. In the early literature, Kafalas & Herrmann [176] and Kafalas & Ferdinand [177] examined the explosive vaporization of single micron-sized water droplets imposed by a pulsed $CO_2$-laser with an energy of approximately 0.5J per pulse. Later, Pinnick et al. [181] extended the explosive vaporisation study for different liquids, e.g. for ethanol and diesel droplets, and observed similar fragmentation patterns with the water experiments for a pulsed $CO_2$ laser and comparable energy. Similar explosive response was also observed for micron-sized liquid metal droplets in the experiments of Basko et al. [182] and Grigoryev et al. [183]; in this case, the picosecond laser pulse results in the development of a plasma state inside the droplet under significantly high thermodynamic conditions, which triggers a violent fragmentation. More recently, Gonzalez Avila & Ohl [174] and Zeng et al. [184] studied a different explosive fragmentation mode, which is developing as an outward widespread jetting from the droplet surface. Specifically, the laser impact onto a millimetre-sized water droplet with a cavitation bubble in the centre imposes a laser-induced cavitation and bubble oscillations that penetrate the droplet surface; different fragmentation regimes were identified based on the dynamic pressure and the energy of the expanding bubble. In an attempt to control the deposition of the laser energy inside the droplet, Klein et al. [185], [186], [6] proposed the use of opaque liquid droplets, which restrict the energy absorption in a thin superficial layer on the illuminated side of the droplet. Specifically, Acid-Red-1 and Oil-Red-O solutions were utilized for water and methyl-ethyl-

ketone (MEK) droplets, respectively, in order to investigate the droplet response to a broad range of laser energy between 1mJ and 420mJ. Additionally, the similarities between the physical principles that govern the laser-induced droplet fragmentation and the fragmentation due to the mechanical impact of a droplet onto a solid surface [8] were highlighted; the impulsive acceleration of the droplet due to the laser impact can be correlated with the respective droplet acceleration before impacting the solid. Recently, Rao et al. [187] demonstrated the influence of the laser focus and energy on the resulting fragmentation of an array of micron-sized water and diesel droplets and identified a new fragmentation pattern. Overall, the available experimental studies in the literature provide a thorough analysis of the droplet dynamics and the physical mechanisms that govern the subsequent fragmentation. However, due to the chaotic and multiscale character of the fragmentation process, very few quantitative data are available regarding the produced fragments, for instance in the high resolution experimental visualizations of Klein et al. [6] and Rao et al. [187], which mainly concern moderate fragmentation regimes.

The hydrodynamics response of a liquid droplet to a laser-pulse impact is driven by the imposed recoil pressure on the droplet surface, as discussed in previous analytical and numerical studies in the literature. The smooth particle hydrodynamics (SPH) method is commonly adopted for the investigation of liquid tin droplets, which are subject to high energy picosecond laser beams. As depicted in the works of Grigoryev et al. [183] and Koukouvinis et al. [188], the SPH method can accurately predict the recoil pressure establishment and propagation inside the droplet, shortly after the laser-pulse impact, the formation of dominant cavitation regions, and the early-time explosive fragmentation, using a given particles population. Concerning the commonly utilized Eulerian methods in droplet fragmentation simulations due to mechanical impact [18], [87], [189], Zeng et al. [184] employed the Volume of Fluids (VOF) method to study the cavitation-induced liquid jetting of a water droplet with a gas bubble in the centre at initial conditions, impacted by a millijoule laser pulse. The coherent droplet interface and the formation of multiple outward liquid jets were accurately captured with the sharp interface method; however, the small-scaled fragments remain unresolved with the VOF method, which can result in significant loss of information in more violent fragmentation regimes with dominant polydisperse fragments. Gelderblom et al. [190] proposed the boundary integral (BI) method for the simulation of the laser-induced droplet deformation. The BI simulations precisely capture the droplet lateral expansion and width deformation under different conditions; nevertheless, the effects of the surrounding air and the subsequent fragmentation of the elongated liquid sheet were excluded from the numerical modelling. Additionally, Gelderblom et al. [190] and Reijers et

al. [191] presented an analytical solution for the developed flow fields inside the droplet, during the early-time response of the droplet to the laser-pulse impact. The analytical studies provided a further insight into the obtained recoil pressure and the resulting droplet dynamics that finally initiate the droplet deformation; however, the analysis is restricted to the early times before the droplet deformation becomes significant.

Following the numerical challenges imposed by the unrevealed laser-induced droplet fragmentation mechanisms, there is a gap in the up-to-date literature regarding a comprehensive numerical analysis that can capture both the early-time droplet dynamics, evolving shortly after the laser-pulse impact and the later-time droplet fragmentation with consideration of all the produced multiscale fragments. The present study proposes the developed multiscale two-fluid approach, introduced in §2.2, in order to investigate the multiscale character of the later-time droplet fragmentation. The numerical methodology has been previously validated against droplet fragmentation cases, driven by the high-speed mechanical impact on a solid surface in §2.3.3. In the present numerical simulations, the multiscale two-fluid approach employs a sharp interface method for the deforming and laterally expanding liquid droplet and a physically consistent sub-grid scale modelling for the produced small-scaled fragments, due to the rim breakup. The novelty of the present simulations lies on the thorough quantitative analysis of both the early-time and the later-time droplet dynamics with a viable computational cost. Specifically, significant information regarding the liquid droplet expansion into an elongated liquid sheet is revealed, concerning the droplet radial expansion velocity and expansion rate. Additionally, the influence of the applied laser beam energy is demonstrated and shows good agreement with both the experimental observations of Klein et al. [6] and theory. Finally, for the first time in the up-to-date literature, an overview of the evolution of the produced fragments' population is presented. The fragments dynamics, including the development of a cloud of fragments in the course of the fragmentation process and the interaction between the detached fragments and the surrounding air under the impact of different beams, are highlighted and size distributions are obtained.

All the details of the numerical configuration for the conducted laser-induced droplet fragmentation simulations are presented in §4.2, including the problem formulation as described in the experimental studies of Klein et al. [185], [186], [6] and the early- and later-time dynamics simulations. Following, in §4.3, the numerical investigations for the rim fragmentation of a liquid droplet, imposed by different intensity laser beams are discussed and compared with the experimental observations of Klein et al. [6] for the same examined conditions.

## 4.2 Numerical Modelling

The fragmentation of a millimetre-sized methyl-ethyl-ketone (MEK) droplet imposed by the impact of a millijoule nanosecond laser pulse is investigated in the present study using numerical simulations. The MEK droplet with an initial radius of $R_0$=0.9mm, density $\rho$=805kg/m³, kinematic viscosity $\nu=0.53\times10^{-6}$ m²/s and surface tension $\gamma$=0.025N/m lies in a nitrogen environment at ambient conditions (p=1atm, T=20ºC). The laser-induced droplet dynamics concern two main stages, namely the early-time droplet response to the laser pulse and the later-time droplet deformation and fragmentation. The early-time droplet dynamics are discussed in §4.2.1 based on the experimental investigations of Klein et al. [185], [186], [6] and a physically consistent numerical modelling is presented in §4.2.2, following the analytical model of Gelderblom et al. [190]; the obtained pressure and velocity fields inside the droplet are subsequently utilized for the initialization of the conducted numerical simulations that capture the later-time phenomena. The numerical simulations of the later-time droplet deformation and fragmentation are performed using the multiscale two-fluid approach, presented in §4.2.3. Details of the simulation set-up are summarized in §4.2.4.

### 4.2.1 Problem Formulation

The numerical modelling of the laser-induced droplet fragmentation is based on the problem formulation and the fundamental principles of the early-time droplet dynamics, as introduced in the experimental studies of Klein et al. [185], [186], [6]. Specifically, in the experiments of [6], the utilized MEK droplets are dyed with Oil-Red-O in order to control the deposition of the laser energy inside the droplet. Therefore, the laser energy is absorbed in a very thin superficial layer with thickness $\delta<<R_0$, which corresponds to the penetration depth of the laser beam into the dyed droplet. After the impact of the millijoule nanosecond laser pulse onto the dyed droplet, local boiling is observed on the superficial layer that results in the emission of a very small vapour mass in the surrounding air. During the vaporization and ejection of the tiny liquid mass, the resulting recoil pressure on the droplet surface accelerates the droplet, until it finally reaches a constant propulsion velocity. The momentum conservation between the vapour mist emission due to the local boiling on the superficial layer and the resulting droplet propulsion is expressed as:

$$mu = \rho R_0^3 U \tag{4.1}$$

where m is the vaporized liquid mass on the superficial layer, u the velocity of the expelled vapour mass, $\rho$ the liquid density, $R_0$ the initial droplet radius and U the droplet propulsion velocity. The

vaporized liquid mass is strongly dependent on the laser energy, as discussed in detail in the study of Klein et al. [185]. Thus, the propulsion velocity scales linearly with the absorbed laser energy on the superficial layer, as follows:

$$U \sim \frac{E_{abs}-E_{th}}{\rho R_0^3 \Delta \mathrm{H}} u \tag{4.2}$$

where $E_{abs}$ is the absorbed laser energy, $E_{th}$ is the minimum energy required to heat the superficial layer to the boiling point and $\Delta H$ represents the latent heat of vaporization of the liquid.

The primary parameter that determines the laser-induced droplet fragmentation, by establishing the propulsion velocity and thus, the expansion rate of the droplet, is the Weber number of the propelled droplet, defined as:

$$We = \frac{\rho \mathrm{R}_0 U^2}{\gamma} \tag{4.3}$$

where $\rho$ is the liquid density, $R_0$ the initial droplet radius, U the droplet propulsion velocity and $\gamma$ the surface tension coefficient.

A schematic illustration of the timescales involved in the laser-induced droplet fragmentation problem is depicted in Figure 4.1. Overall, the early-time droplet dynamics are characterized by the laser pulse that impacts the dyed droplet's illuminated side for a duration of 5ns, followed by the local boiling of the superficial layer and the vapour recoil that initiates the droplet propulsion until a constant velocity is achieved after approximately 10μs, as observed in the experiments. During the vapour expulsion time $\tau_e$, the droplet does not deform yet and the tiny fraction of ejected vapour mass from the superficial layer does not have a macroscopic influence on the droplet spherical shape. At later times, the deformation of the droplet surface dominates on the inertial timescale, defined as $\tau_i = \mathrm{R}_0/U \sim 0.1ms$. Eventually, the droplet lateral expansion is restricted by the surface tension and the extended fragmentation on the capillary timescale, calculated as $\tau_c = \sqrt{\rho R_0^3/\gamma} = 4.8ms$. The distinct separation of the characteristic timescales during the early- and later-time droplet dynamics provides a significant flexibility in the numerical modelling of the individual stages, as discussed below.

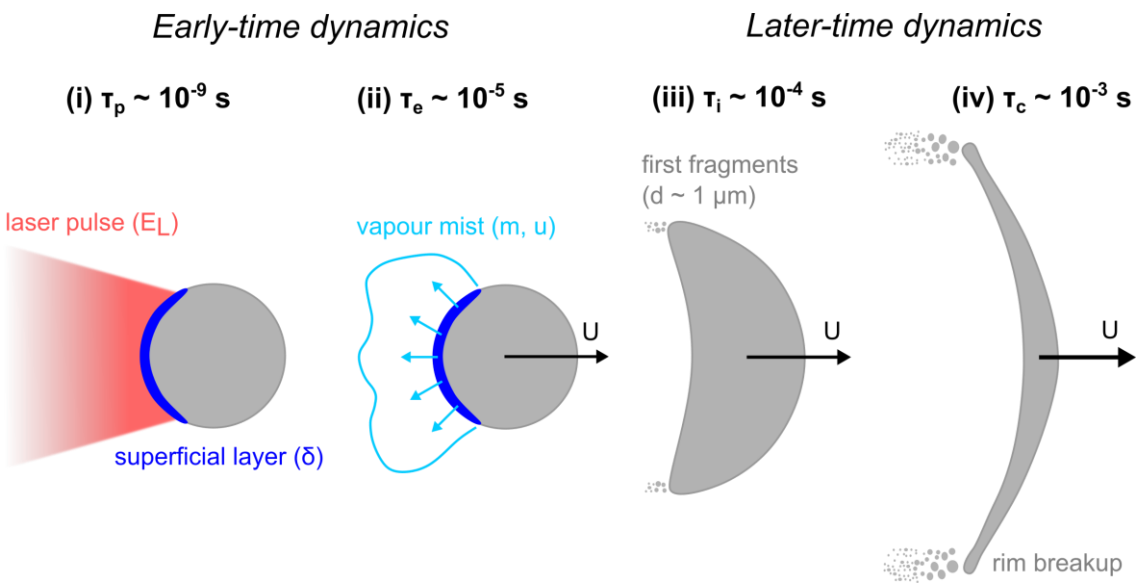


**Figure 4.1** Separation of timescales in the laser-induced droplet rim fragmentation problem. (i) A nanosecond laser pulse impacts onto the left side of the dyed droplet. (ii) The vaporized liquid mass on the superficial layer is ejected backwards. As a result, the droplet accelerates until it reaches a constant propulsion velocity at the vapour expulsion time $\tau_e$. (iii) The droplet propels and deforms at the inertial time $\tau_i$. (iv) The surface tension and the extended fragmentation restrict the droplet lateral expansion at the capillary time $\tau_c$.

## 4.2.2 Early-Time Dynamics and Initial Fields

The separation of timescales in the laser-induced droplet fragmentation problem allows to isolate the modelling of the early-time droplet dynamics from the later-time droplet deformation and fragmentation without introducing physical or numerical restrictions. Gelderblom et al. [190] provided a unified analytical model for all early-time phenomena, starting from the laser-pulse impact onto the droplet for a duration $\tau_p$, until the droplet propulsion with constant velocity at time $\tau_e$, illustrated in Figure 4.1(i-ii). The model is based on the pressure impulse theory, described by Cooker & Peregrine [192] and Antkowiak et al. [193] and concerns a pressure pulse with magnitude $p_e$ applied on the droplet surface for a duration $\tau_e$. Accordingly, the absolute impulse scale $p_e\tau_e$ imposes the droplet propulsion. The momentum conservation at time $\tau_e$ is expressed, as follows:

$$\int_0^{\tau_e} \int_A \; p_e e_z \cdot dA \, dt = \frac{4}{3}\pi\rho R_0^3 U \tag{4.4}$$

where $\tau_e$ is the vapour expulsion time, A the droplet surface area, $p_e$ the magnitude of the pressure pulse, $\rho$ the liquid density, $R_0$ the initial droplet radius, U the droplet propulsion velocity.

The pressure pulse applied on the droplet surface changes the flow inside the droplet, which initially lies stagnant at ambient conditions. The developed pressure and velocity fields inside the droplet are found to be well established at time $\tau_e$. As derived from the assumptions of Gelderblom et al. [190] for an inviscid, irrotational and incompressible flow, the pressure field inside the droplet at time $\tau_e$ is obtained from the solution of the Laplace equation:

$$\Delta p = 0 \tag{4.5}$$

for the non-dimensional pressure field $p/p_e$. Subsequently, the velocity field inside the droplet at time $\tau_e$ is calculated from the momentum equation, as:

$$u = -\frac{\tau_e}{\rho}\nabla p \tag{4.6}$$

for the non-dimensional velocity field $pR_0u/p_e\tau_e$.

The pressure boundary condition of equation (4.5) refers to the original pressure pulse that is applied on the droplet surface and considers the dependence of the pulse shape on the angle θ, such that:

$$p(r = 1, \theta) = f(\theta) \tag{4.7}$$

where the non-dimensional pressure pulse f(θ) is proportional to the actual laser pulse that impacts onto the droplet surface in the conducted experiments of Klein et al. [185], [186], [6]. Therefore, Gelderblom et al. [190] suggested a Gaussian-shaped pressure pulse to remain consistent with the typically used Gaussian laser-beam profiles in the experiments. The Gaussian-shaped pressure pulse is formulated as:

$$f(\theta) = ce^{-\frac{\theta^2}{2\sigma^2}} \tag{4.8}$$

where σ is the pulse width. In the experiments of Klein et al. [185], a laser-beam profile with σ= π/6 is used. For σ=π/6, the parameter c is calculated as $c = \frac{2\sqrt{2}}{\sigma\pi^{\frac{3}{2}}e^{-2\sigma^2}\left(2erfi[\sqrt{2}\sigma]-erfi\left[\frac{i\pi+2\sigma^2}{\sqrt{2}\sigma}\right]-erfi\left[\frac{-i\pi+2\sigma^2}{\sqrt{2}\sigma}\right]\right)} =$ 0.825.

In the present numerical study, the previously presented analytical model for the early-time droplet dynamics is adapted so as to be incorporated in the CFD framework. Specifically, the MEK droplet is simulated as a 5° spherical wedge with one cell thickness in the azimuthal direction, using pimpleFoam, a transient incompressible solver in OpenFOAM®. As suggested in the analytical model, for times $t \leq \tau_e$, a pressure pulse is applied on the surface of the initially

stagnant MEK droplet at ambient conditions. Correspondingly, the pressure pulse is set as the pressure boundary condition on the spherical wedge domain, given in dimensional form as:

$$p(\theta) = p_e f(\theta) + p_{atm} \tag{4.9}$$

Details of the numerical configuration for the simulation of the early-time droplet dynamics are illustrated in Figure 4.2(i).

At time $t=\tau_e$, the established pressure and velocity fields inside the droplet are calculated from the numerical simulations, as illustrated qualitatively in Figure 4.2(ii). Later, the obtained flow fields are utilized for the initialization of the droplet in the conducted numerical simulations that initiate at time $t>\tau_e$ and capture the later-time phenomena, as demonstrated in §4.2.4.

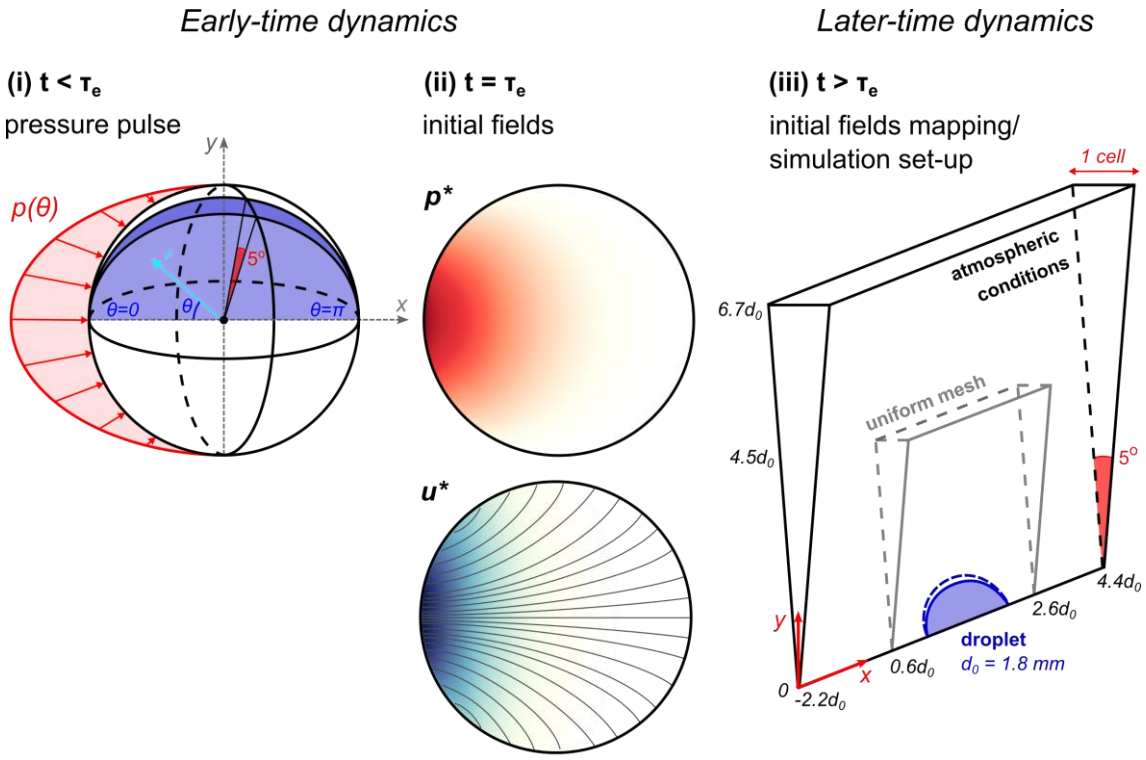


**Figure 4.2** Problem configuration and simulation set-up. (i) For $t < \tau_e$, the axisymmetric pressure pulse $p(\theta)$ is applied on the droplet surface. (ii) At $t = \tau e$, the initial pressure and velocity fields inside the droplet are obtained. (iii) The initial fields are mapped into the wedge geometry. For $t > \tau_e$, the droplet fragmentation is simulated using the multiscale two-fluid approach.

### 4.2.3 Later-Time Dynamics and Numerical Method

The later-time phenomena, illustrated in Figure 4.1(iii-iv), are governed by the deformation of the droplet into an elongated liquid sheet and the subsequent fragmentation of the droplet rim. The detached fragments form a polydisperse cloud of secondary droplets with diameters at least two orders of magnitude smaller than the initial droplet. Therefore, in the course of the phenomenon, a flow field with dominant multiscale structures is developed, which imposes additional complexities in a full-scale numerical analysis with a viable computational cost.

In the present numerical study, the developed Σ-Y two-fluid model with dynamic local topology is utilized for the laser-induced droplet rim fragmentation simulations. The multiscale two-fluid approach provides a physically consistent and numerically stable multiscale framework for the investigation of all the scales involved in the laser-induced droplet fragmentation problem with a viable computational cost. A fundamental principle of the multiscale framework is the detection of different flow regimes based on advanced on-the-fly topological criteria and the application of the appropriate modelling approach for local interfaces based on the dimensions of the underlying structures. In particular, the interface of the expanding but still coherent liquid sheet is fully resolved using the VOF sharp interface method [45], [46]. On the contrary, the produced fragments, which are smaller than the local mesh resolution, are modelled within a diffuse interface approach. In this case, an additional transport equation for the interface surface area density Σ [53], [55] is incorporated to model the unresolved sub-grid scale phenomena and provides an estimation for the dimensions of the unresolved sub-grid scale droplets. The governing equations of the multiscale two fluid approach, along with details of the implementation in OpenFOAM®, are presented in §2.2.

### 4.2.4 Later-Time Simulation Initialization and Set-up

The numerical simulations of the later-time droplet deformation and fragmentation initiate at time $t>\tau_e$ with ambient atmospheric conditions, while the flow field inside the droplet is initialized based on the modelling of the early-time phenomena in §4.2.2. The computational domain consists of a $5^o$ wedge geometry with one cell thickness in the azimuthal direction and a mesh with a resolution of 200 cells per original droplet diameter around the area of interest is applied. Details of the initial configuration for the simulations of the later-time phenomena are illustrated in Figure 4.2(iii). Different Weber numbers in the range of 90 to 750 are examined with

corresponding droplet propulsion velocities between 1.76m/s and 5.09m/s. The simulation results are compared with the experimental observations of Klein et al. [6] for the same conditions.

Regarding the numerical simulation set-up, the spatial discretization is based on second-order accurate discretization schemes. Time stepping is performed adaptively during the simulation to respect the selected limit for the convective Courant–Friedrichs–Lewy (CFL) condition of 0.2. The thermodynamic closure of the system is achieved by implementing the stiffened gas equation of state, proposed by Ivings et al. [94], for the liquid phase and the ideal gas equation of the state for the gaseous phase. Concerning the turbulence modelling, an LES approximation is implemented with the one-equation SGS model of Lahey [93]. However, the utilized computational domain imposes limitations regarding the accurate capturing of the turbulent state, which corresponds to fully 3D-developed phenomena. The simulations are initialized without turbulence in the flow field, since the droplet acceleration at early-times involves low velocities and Reynolds numbers around $10^3$. Therefore, in the absence of developed turbulence at the initial conditions, the LES approximation can be applied in the present geometry of one cell thickness in the azimuthal direction without significant modelling restrictions.

A crucial parameter for an accurate simulation of the later-time droplet deformation and fragmentation is the initialization of the pressure and velocity fields inside the droplet at time $t=\tau_e$, as obtained from the early-time simulations of §4.2.2. For a given Weber number, the droplet propulsion velocity is obtained from equation (4.3) and subsequently, the absolute impulse scale $p_e\tau_e$ can be calculated from equation (4.4), as follows:

$$p_e\tau_e = \frac{\rho R_0 U}{3} \tag{4.10}$$

Different combinations of recoil pressure $p_e$ and vapour expulsion time $\tau_e$ values determine different initialization sets ($p_e$, $\tau_e$) for the same propulsion velocity. However, the droplet expansion rate is defined by the absolute impulse scale and is not influenced by the individual $p_e$, $\tau_e$ values. Therefore, any obtained initialization set with $\tau_e \ll \tau_i$ provides a valid modelling of the early-time phenomena for a specified propulsion velocity. For instance, in Figure 4.3, three different initialization sets ($p_e$, $\tau_e$) are examined to simulate the deformation and the early-time fragmentation of a MEK droplet with Weber number 90. Despite the different initialization, all the three cases show good qualitative agreement with respect to the droplet lateral expansion, the subsequent fragmentation, and the production of a gradually increasing cloud of fragments. The independence of the droplet expansion rate on the individual $p_e$, $\tau_e$ values can be generalized for any Weber number, as depicted in Figure 4.4 for the deformation of a MEK droplet at Weber

numbers 90, 170, 330, 460 and 750 and three different initialization sets for each examined propulsion velocity. Overall, the droplet deformation, concerning both radius expansion and width reduction, remains almost unaffected by the different initialization of the problem. Additionally, Figure 4.4 indicates the relation between the Weber number and the expansion rate of the droplet, showing a significantly faster evolution of the droplet deformation with increasing Weber number.

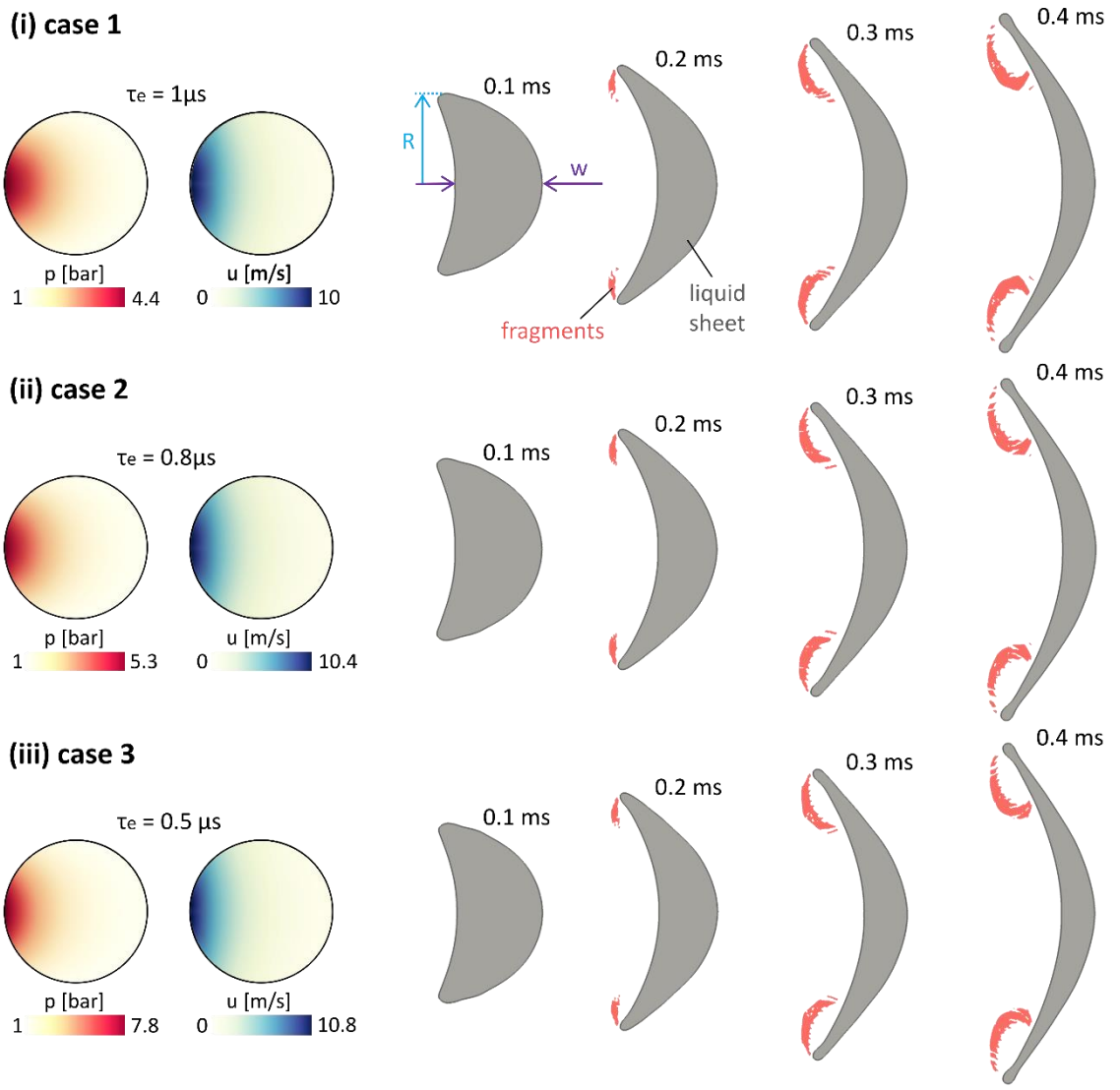


**Figure 4.3** Laser-induced droplet deformation and early-stage rim fragmentation at We=90 . Qualitative comparison of the droplet shape evolution for three different initialization sets, i.e. (i) $\tau_e$=1μs, $p_e$=4.26bar, (ii) $\tau_e$=0.8μs, $p_e$=5.32bar (iii) $\tau_e$=0.8μs, $p_e$=8.51bar, for the same propulsion velocity U=1.76m/s, as calculated from equation (4.10).

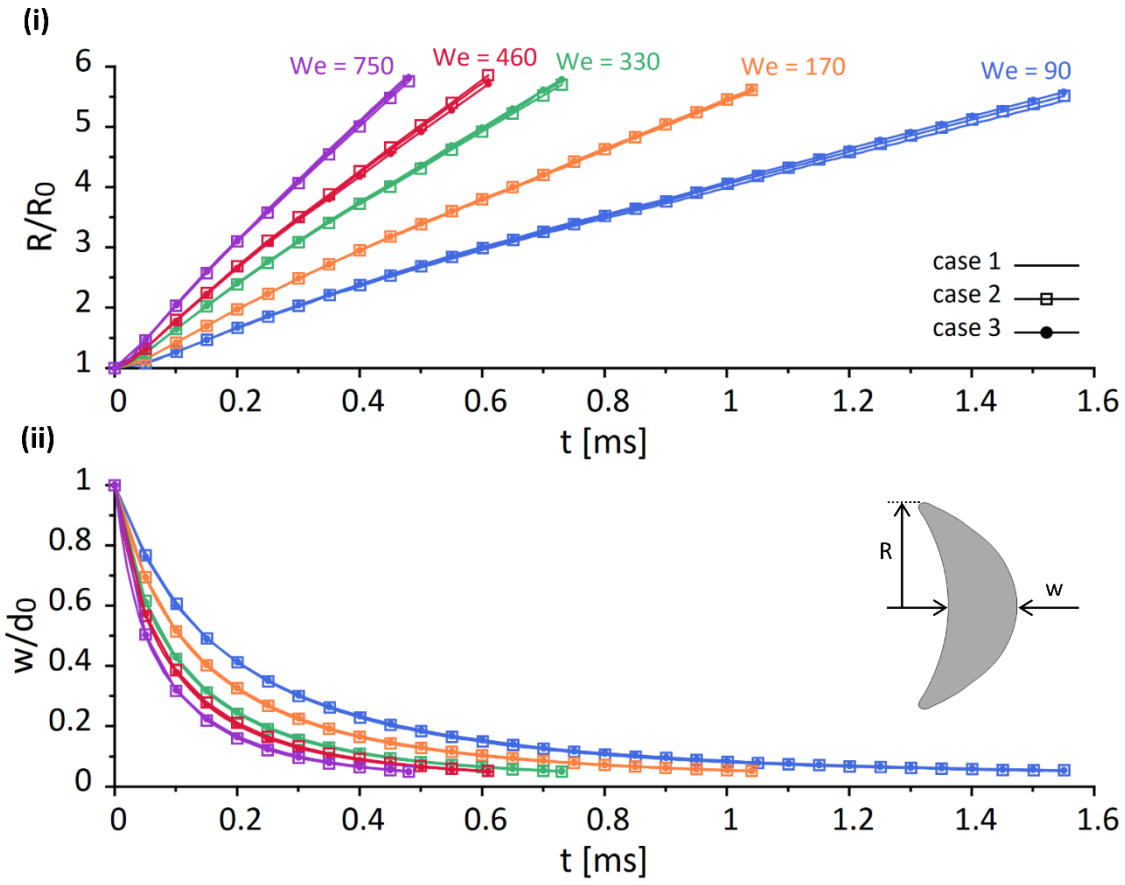


**Figure 4.4** Evolution of the laser-induced droplet deformation at We = 90, 170, 330, 460, 750. (i) Droplet radius expansion and (ii) droplet width reduction for three different initialization sets for each examined condition, i.e., different individual $p_e$, $\tau_e$ values for the same propulsion velocity, as calculated from equation (4.10).

## 4.3 Results and Discussion

The laser-induced rim fragmentation for a MEK droplet at We=330 is presented in Figures 4.5 and 4.6, comparing the simulation results with the experimental observations of Klein et al. [6]. Following the impact of the millijoule nanosecond laser pulse, the droplet has evolved into a thin liquid sheet surrounded by a cloud of fragments, already at t=0.27ms in Figure 4.5(i). Subsequently, the liquid sheet expands further in the lateral direction and at the same time, the extensive rim breakup enhances the cloud of fragments with additional polydisperse droplets. The expanding liquid sheet is captured by the sharp interface formulation of the multiscale framework, while the detached fragments are subject to the sub-grid scale modelling, as illustrated in Figure 4.5(ii). Within the cloud of fragments droplets with diameters between 0.09μm and 9μm are detected; the upper limit is correlated with the smallest structures that can be resolved with the

sharp interface method for a local mesh resolution of 200 cells per initial diameter and the lower limit corresponds to the spatial resolution of the utilized camera in the experiments. Overall, the numerically captured expanding sheet follows the deforming shape and the curvature observed in the experiments, while the modelled fragments are detected close to the liquid sheet during the early stages of fragmentation and move further backwards at later times. Moreover, the radial dependence of the sheet thickness, which is demonstrated in the experimental results in front view in Figure 4.6(i), is well predicted by the numerical simulations. Specifically, the maximum thickness is found in the centre of the liquid sheet and the minimum thickness is observed close to the rim. In consistence with the experimental observations of Klein et al. [6], the rim is captured as a slightly thicker border. At later times, a more uniform thickness is predicted along the expanding sheet length, as displayed qualitatively in the liquid sheet isosurfaces in Figure 4.5(ii) and extracted from the indicative calculations of the local thickness in Figure 4.6(ii). Additional simulations are conducted using the same early-time simulations for the initialization of the problem and the VOF solver in OpenFOAM®. The VOF method results, presented in Figures 4.5(iii) and 4.6(iii), show a good agreement with the respective results obtained with the multiscale two-fluid approach, regarding the capturing of the liquid sheet deformation; nevertheless, the VOF method excludes the sub-grid scale information for the produced fragments.

Focusing on the predictions of the multiscale two-fluid approach for each examined time instance presented in Figures 4.5 and 4.6, at time t=0.27ms, which corresponds to the inertial time $\tau_i$ with dominant droplet deformation, the numerical results meet the experimental observations and accurately predict the macroscopic liquid sheet expansion. At the same time, a cloud of fragments, that recirculate behind the expanding sheet, is captured, with the largest droplets observed close to the rim. Later, at time t=0.54ms, the liquid sheet thickness is reduced to about 7% of the initial droplet diameter. The numerical results satisfactorily follow the deforming shape of the thin liquid sheet and the lateral expansion, while smaller fragments are captured downstream. However, an early breakup is observed close to the rim, where the local thickness of the liquid sheet is considerably decreased; a sheet breakup is not observed in the experimental results at that time. The multiscale two-fluid approach predicts a similar early sheet breakup even with a finer mesh of a 250 cells per initial droplet diameter, as depicted in Figure 4.6(ii). In the VOF method results in Figure 4.6(iii), the early sheet breakup is still present but developed in a smaller extent.

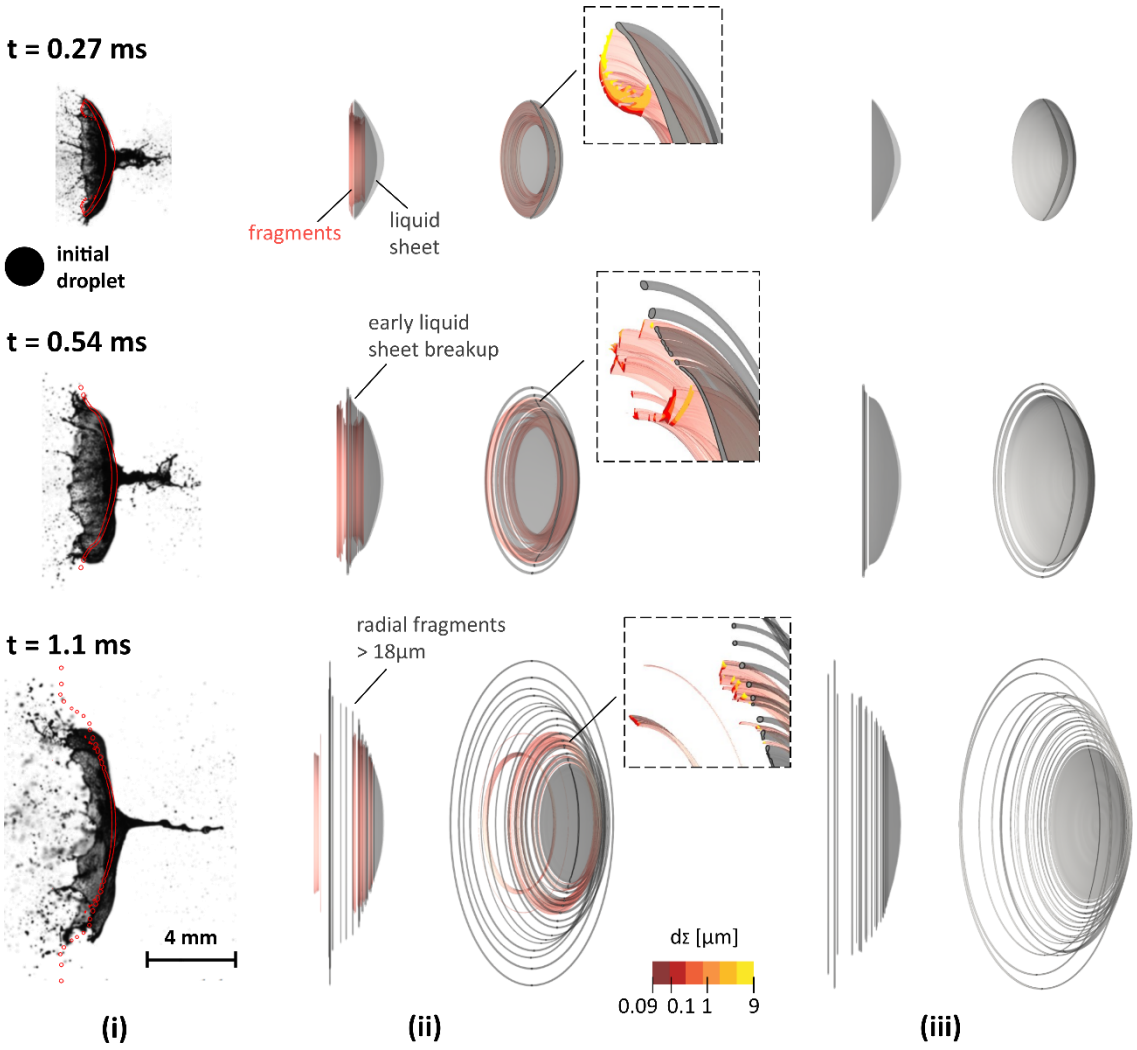


**Figure 4.5** Laser-induced droplet rim fragmentation at We=330. (i) Comparison between the experimental visualizations of Klein et al. [6] in sideview and the isoline of the liquid volume fraction at $10^{-3}$, obtained with the multiscale two-fluid approach. (ii) 3D reconstructed results in sideview and 30° angle, using the multiscale two-fluid approach. The expanding liquid sheet is captured by the sharp interface formulation (in grey the isosurface for liquid volume fraction at 0.5) and the detached fragments are captured by the diffuse interface formulation (in red the isosurface for fragments larger than 0.09µm). Zoomed-in view for the dimensions of the produced fragments after the rim breakup. (iii) 3D reconstructed results in sideview and 30° angle, using the VOF method. Iso-surface of the liquid volume faction at 0.5.

Therefore, the early sheet breakup is a numerical limitation, observed with both numerical methods. As depicted in the simulation results, the utilized moderate mesh resolution is insufficient to accurately capture the significantly decreased sheet thickness around the rim. Additionally, the more pronounced early sheet breakup using the multiscale two-fluid approach is related to the modelling of slip velocity effects; the relative velocity between the very thin liquid

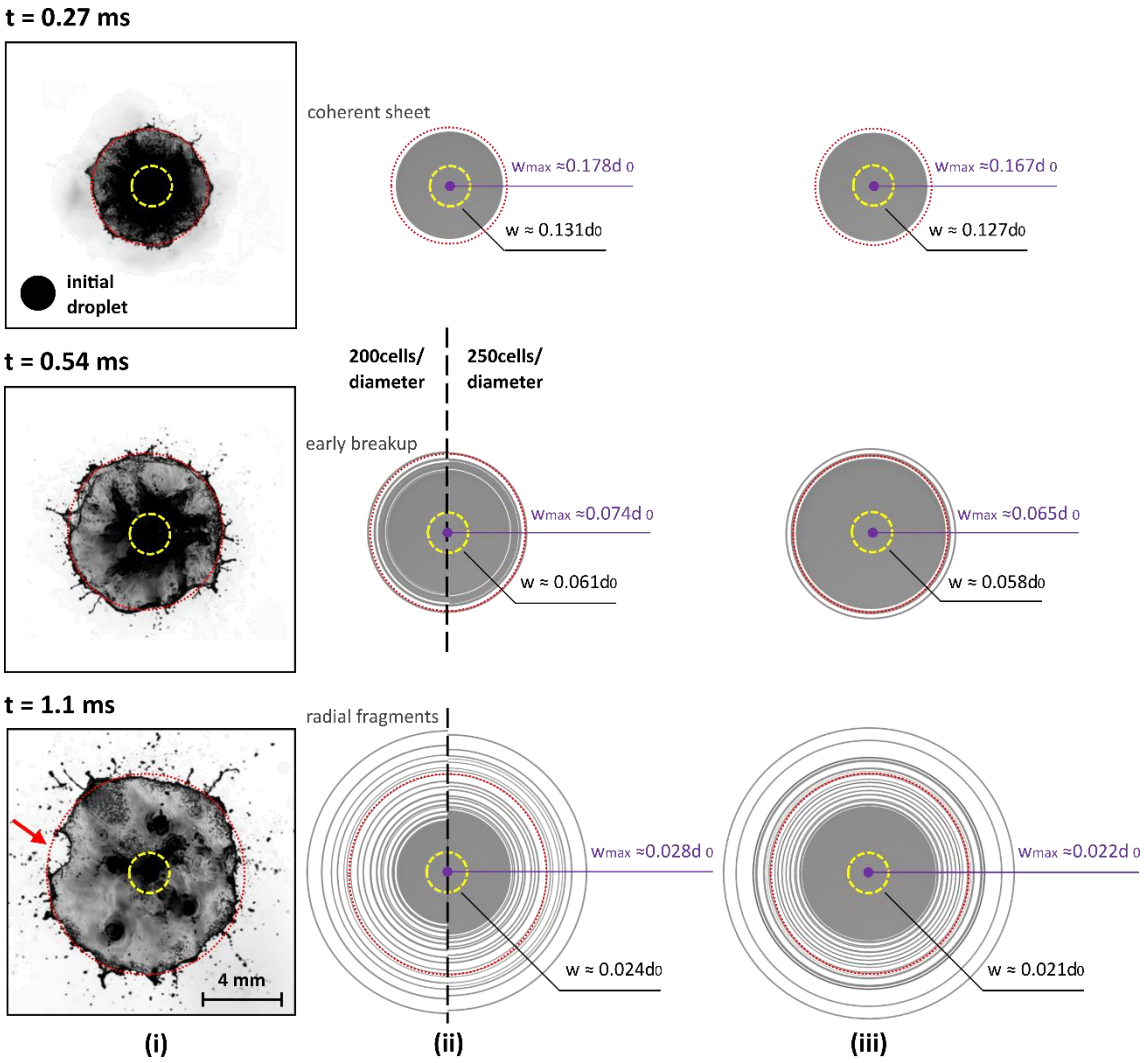


**Figure 4.6** Laser-induced droplet rim fragmentation at We=330. (i) Experimental visualizations of Klein et al. [6] in front view. (ii) 3D reconstructed results in front view, using the multiscale two-fluid approach. The expanding liquid sheet, captured by the sharp interface formulation, is illustrated as the iso-surface of the liquid volume faction at 0.5 with a mesh resolution of 200 (left) and 250 (right) cells per initial droplet diameter. (iii) 3D reconstructed results in front view, using the VOF method. Iso-surface of the liquid volume faction at 0.5 with a mesh resolution of 200 cells per initial droplet diameter. The red circle defines the borders of the liquid sheet rim in the experimental results. The calculated thickness of the thin liquid sheet on the central line (in purple) and on the initial droplet radius (in yellow) is illustrated on top of the simulation results.

sheet and the surrounding air locally exceeds the value of 20 m/s around the rim, i.e. is approximately 6 times higher than the droplet propulsion velocity, and leads to the early breakup. Following, at time t=1.1ms, the significantly reduced thickness of the liquid sheet reaches the limits of the computational model. The length of the numerically captured coherent sheet is limited, while a trace of radial fragments follows the shape of the coherent elongated sheet, which

is shown in the experimental visualizations. The successive detachment of radial fragments from the sheet rim is a numerical artefact, which is previously recognized in the boundary integral (BI) simulations of Gelderblom et al. [190] during advanced stages of the fragmentation process.

Instead, at the same times, the experimental results demonstrate the nucleation of holes on the liquid sheet as the major fragmentation mechanism. As illustrated in Figure 4.6(i), the first holes are already detected along the rim at t=1.1ms and thus, the assumption for an axisymmetric flow field is disrupted. Accordingly, the current numerical investigations focus on the droplet deformation and the rim fragmentation before the sheet breakup becomes significant, i.e., until the thickness of the expanding sheet is reduced to approximately 10% of the initial droplet diameter. Finally, the jetting, which is shown in the experimental results to initiate from the centre of the deforming droplet, is carrying a very small liquid mass and is not related to the pressure pulse that governs the droplet expansion, as analysed by Klein et al. [6]. Therefore, the investigation of jetting phenomenon remains beyond the scope of the present study.

The effect of Weber number on the MEK droplet deformation and fragmentation is examined in Figures 4.7-4.10; the range of values examined are 90, 170, 330 and 750 and are presented for time-instances that correspond to a liquid sheet with thickness 50%, 20% and 10% of the initial droplet diameter. Since the Weber number reflects the droplet expansion rate, which is set by the droplet propulsion, the examined width deformations are observed at significantly different times for each case. At the initial conditions, the strong impact of the Weber number is already pronounced, resulting to significantly increased initial pressure and velocity magnitudes at higher Weber numbers. Specifically, for We=90, the initial pressure and velocity fields inside the droplet, as calculated from the early-time simulations in order to reach a propulsion velocity of 1.76m/s, have a maximum value of 4.4bar and 10m/s, respectively. On the contrary, at We=750, the stronger pressure pulse, applied on the droplet during the early-time simulations, imposes initial pressure and velocity fields with the same profile but significantly increased maximum values up to 50.1bar and 31m/s, respectively. In the course of the phenomenon, the atmospheric pressure inside the droplet is rapidly recovered in a few microseconds and thus, a pressure distribution close to atmospheric conditions is stabilized, before significant deformation is observed. Therefore, the droplet expansion is primarily governed by the radial component of the velocity ($u_{sheet}(y)$), which shows maximum values on the expanding rim. At later stages, the radial velocity on the rim gradually decreases over time, as a result of the slightly restricted droplet expansion due to the dominance of the rim fragmentation.

Focusing on the early times of the droplet deformation, due to the strong initial pressure kick at We=750, the formation of a low-pressure region inside the droplet is observed, which is related to the creation of cavitation bubbles. As highlighted in Figure 4.10 at 0.05ms, the developed low-pressure region is significantly small compared to the total mass of the deforming droplet and thus, it does not affect the macroscopic droplet expansion. Therefore, a cavitation model has not been implemented in the multiscale framework for the examined conditions. Instead, a very small volume fraction of air of the order of $10^{-6}$, which corresponds to a typical nucleation volume fraction [159], is introduced in the initial droplet volume fraction. Under this assumption, the small gaseous volumes inside the droplet will expand after the significant pressure drop, producing expansion similar to those that would occur with cavitation. Subsequently, when the low-pressure region reaches the backside of the propelled droplet interface, the gaseous volumes collapse. Due to the minor breakup on the local interface, very few nanoscale droplets are captured by the numerical model at 0.17ms; these droplets do not influence the total fragments' population.

Overall, the numerical results in Figures 4.7-4.10 demonstrate that an increasing Weber number imposes a faster deformation of the initial spherical droplet into an elongated liquid sheet and an earlier breakup of the sheet rim. Additionally, the effect of the Weber number on the shape of the deforming liquid sheet with respect to the lateral expansion and the radial distribution of the thickness is observed. Specifically, during the early stages of deformation, the droplet shows an almost identical shape in the four examined cases for the same thickness reduction by 50%; the examined deformation is observed at different times for each case in accordance with the Weber number dependent expansion rates. However, at later times, when already a thin liquid sheet is formed, a higher Weber number leads to an increased lateral expansion and thus, a more uniform thickness distribution for the same width deformation on the central line. Indicatively, for a liquid sheet thickness 20% of the initial droplet diameter, the lateral sheet expansion is increased by approximately 7% at We=330 and by 13% at We=750, compared to the predicted expansion at We=90 for the same thickness.

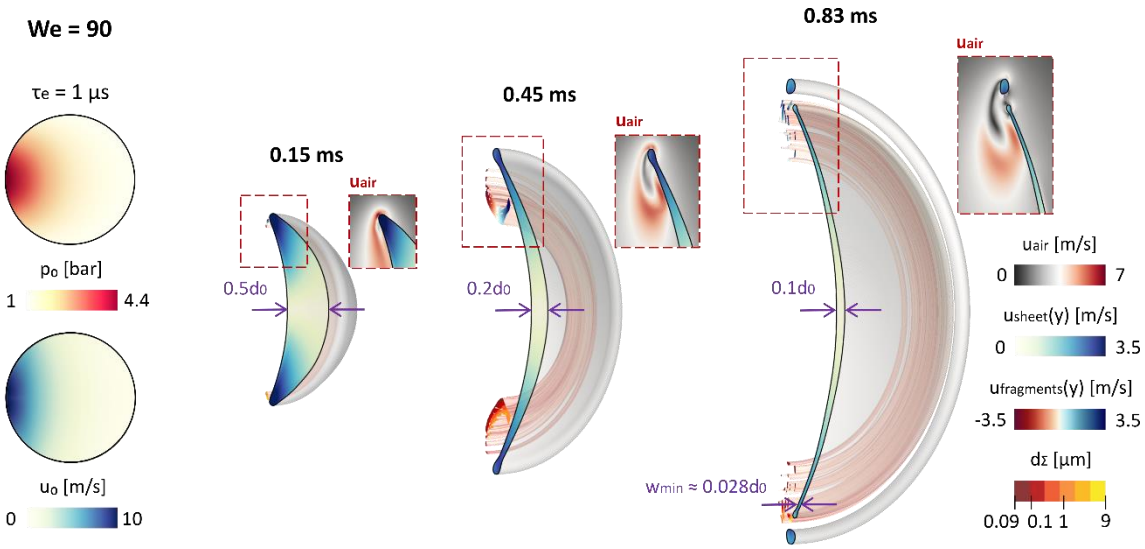


**Figure 4.7** Laser-induced droplet rim fragmentation at We=90. Initial pressure and velocity fields inside the droplet, obtained for U=1.76m/s and $\tau_e$=1μs. Liquid sheet expansion velocity in the lateral direction, radial velocity (top) and dimensions (bottom) of the detached fragments for three time-instances that correspond to a liquid sheet with thickness 50%, 20% and 10% of the initial droplet diameter. The air velocity field around the rim and the developed vortex are depicted on the side panels. The minimum captured thickness is illustrated at 0.83ms.

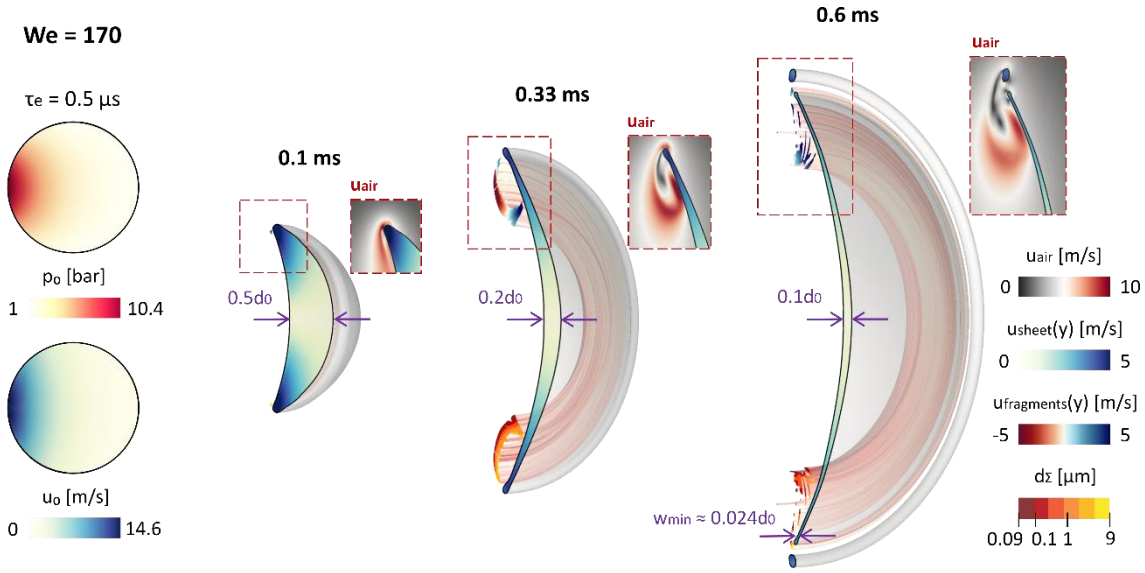


**Figure 4.8** Laser-induced droplet rim fragmentation at We=170. Initial pressure and velocity fields inside the droplet, obtained for U=2.42m/s and $\tau_e$=0.5μs. Liquid sheet expansion velocity in the lateral direction, radial velocity (top) and dimensions (bottom) of the detached fragments for three time-instances that correspond to a liquid sheet with thickness 50%, 20% and 10% of the initial droplet diameter The air velocity field around the rim and the developed vortex are depicted on the side panels. The minimum captured thickness is illustrated at 0.6ms.

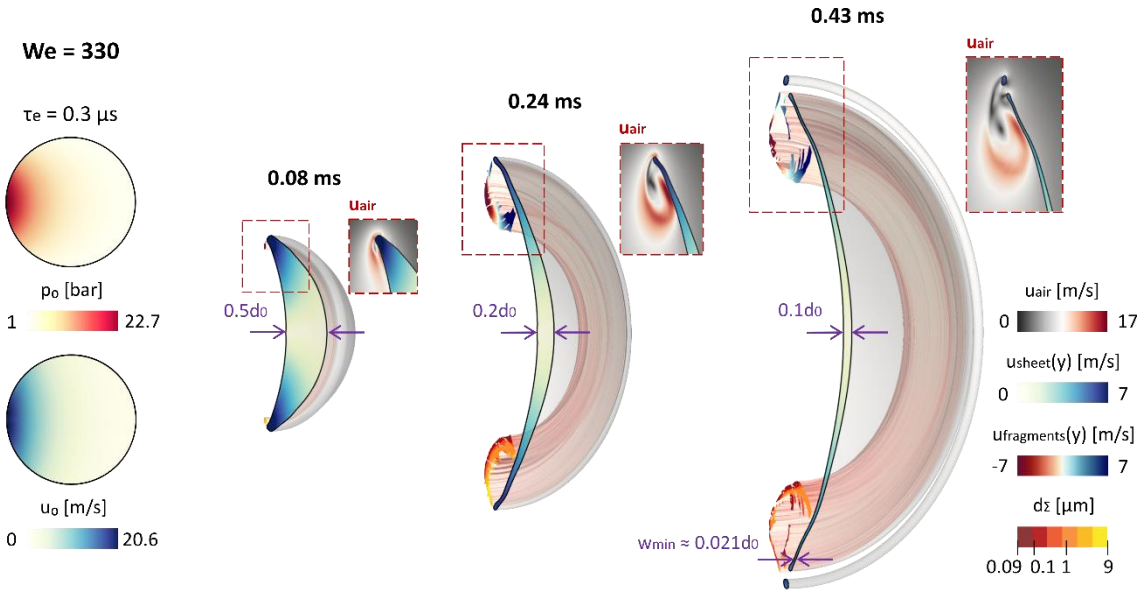


**Figure 4.9** Laser-induced droplet rim fragmentation at We=330. Initial pressure and velocity fields inside the droplet, obtained for U=3.37m/s and $\tau_e$=0.3μs. Liquid sheet expansion velocity in the lateral direction, radial velocity (top) and dimensions (bottom) of the detached fragments for three time-instances that correspond to a liquid sheet with thickness 50%, 20% and 10% of the initial droplet diameter. The air velocity field around the rim and the developed vortex are depicted on the side panels. The minimum captured thickness is illustrated at 0.43ms.

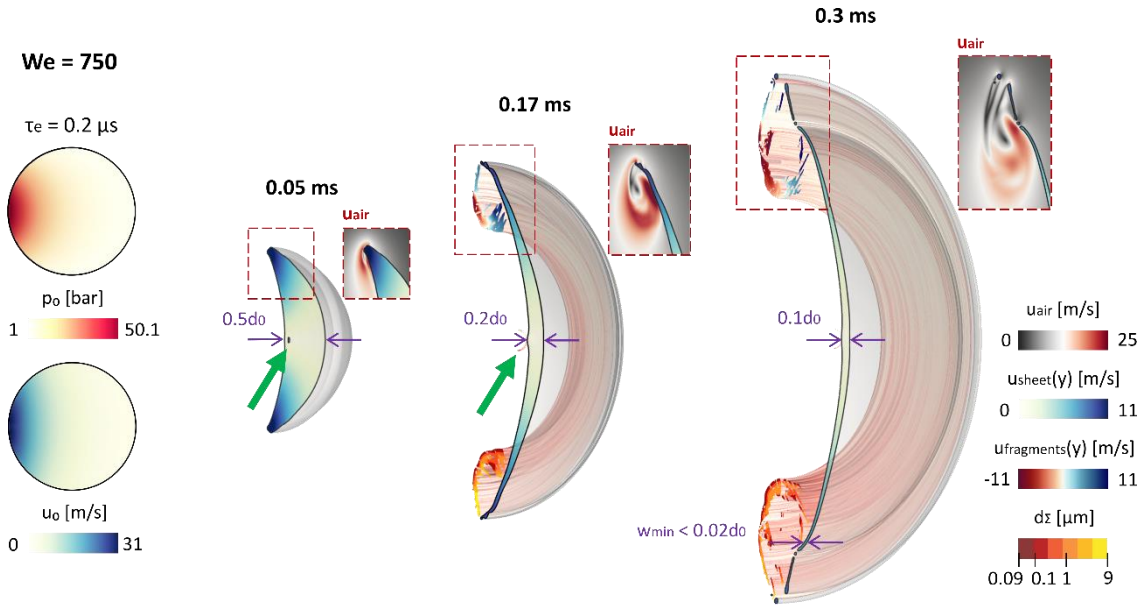


**Figure 4.10** Laser-induced droplet rim fragmentation at We=750. Initial pressure and velocity fields inside the droplet, obtained for U=5.09m/s and $\tau_e$=0.2μs. Liquid sheet expansion velocity in the lateral direction, radial velocity (top) and dimensions (bottom) of the detached fragments for three time-instances that correspond to a liquid sheet with thickness 50%, 20% and 10% of the initial droplet diameter. The air velocity field around the rim and the developed vortex are depicted on the side panels. The minimum captured thickness is illustrated at 0.3ms. The arrows point to the minor low-pressure region and the marginal amount of created droplets after collapse.

Alongside the liquid sheet lateral expansion, the rim fragmentation becomes more significant over time with more fragments to be produced at higher Weber numbers, as observed in Figures 4.7-4.10. On average, the largest fragments with diameters above 5μm are detected close to the rim. Subsequently, the sizes of the newly detached fragments evolve further inside the developed cloud of polydisperse droplets, following the local aerodynamic conditions and the modelled sub-grid scale droplets interactions. The new fragments are detached from the rim with radial velocities ($u_{fragments}(y)$) comparable with the radial velocity of the rim at the time of breakup, as previously discussed in the experimental study of Klein et al. [6]. Afterwards, the fragments are subject to a recirculation behind the liquid sheet, driven by the moving vortex that is created as a result of the interaction between the propelled and expanding liquid sheet and the surrounding air. The air vorticity is becoming less significant at the later stages of rim fragmentation; however, it still influences the increasing number of fragments produced at higher Weber numbers, as shown at 0.43ms and 0.3ms in Figures 4.9 and 4.10, respectively.

A quantitative comparison between the experimental observations of Klein et al. [6], the analytical model of Villermaux & Bossa [7] and the simulation results using the VOF method and the multiscale two-fluid approach is presented in Figure 4.11, examining the droplet radial expansion under different Weber numbers. In the numerical simulations, the droplet expansion is considered, until a thin liquid sheet with maximum thickness at 10% of the initial droplet diameter is formed. On the whole, the numerical results capture the strong dependence of the droplet expansion rate on the Weber number and satisfactorily follow the experimental observations. A better agreement between the numerical and the experimental results is obtained at the later stages of the droplet expansion process, as similarly observed for the analytical solution. Specifically, the VOF method results precisely follow the predictions of both the analytical model and the experiments, during the advanced stages of the droplet expansion. With respect to the capability of the multiscale two-fluid approach to accurately capture the droplet deformation and radial expansion, the obtained results illustrate on average a small delay of maximum 5% compared to the calculations with the VOF method. The slightly delayed expansion, observed with the two different numerical methods, can be related to the sub-grid scale modelling, which is performed within the multiscale two-fluid approach and accounts for the produced fragments due to the rim breakup. Therefore, under the multiscale framework, a part of the deformation energy that would be utilized for the droplet radial expansion is now employed for the development of fragments. However, as depicted in Figure 4.12, the volume concentration of the modelled fragments over the total volume of the liquid phase increases significantly at higher Weber numbers. Thus, the

production of fragments is not negligible in the course of the droplet expansion and the resulting rim fragmentation. At lower Weber numbers, the concentration of fragments relatively stabilizes during the rim fragmentation evolution, while with an increasing Weber number, the fragments population is continuously enhanced over time and even exceeds 40% of the total liquid volume at the later stages of rim fragmentation for the highest examined Weber number of 750. In the VOF simulations, the information of the dominant sub-grid scale fragments is not considered, since it concerns structures smaller than the resolved resolution. Instead, the VOF method creates non-physical large-scaled structures, larger than the computational cell size, in order to conserve the mass in the flow field. Therefore, with increasing Weber numbers, the multiscale two-fluid approach provides a more accurate and physical consistent prediction of the polydisperse droplet fragmentation in contrast to the numerical deficiencies of the VOF method under those demanding conditions.

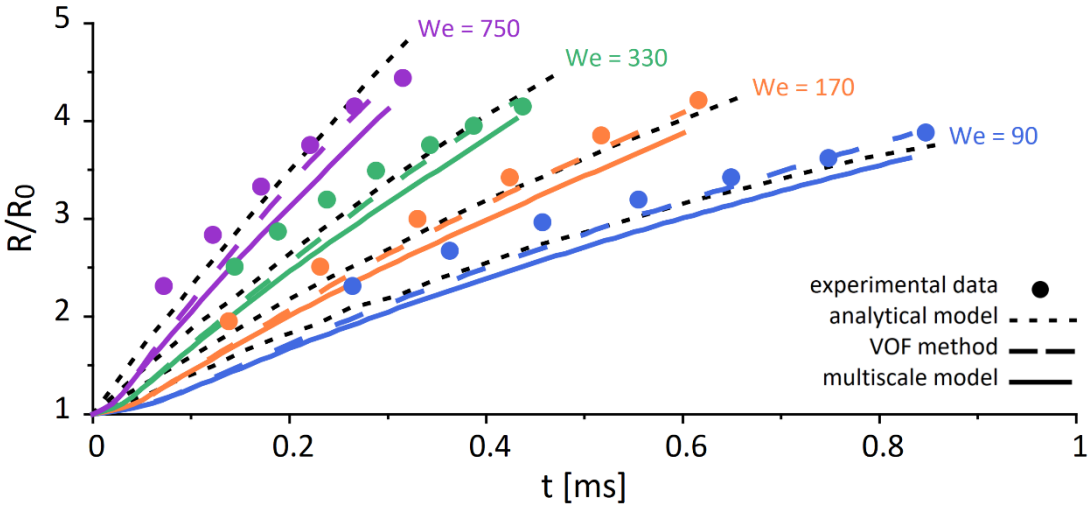


**Figure 4.11** Expansion of the liquid sheet radius, as a result of the laser-induced droplet deformation at We = 90, 170, 330, 750. Comparisons between the experimental observations of Klein et al. [6], the analytical model of Villermaux & Bossa [7], and the simulation results using the VOF method and the multiscale two-fluid approach until a liquid sheet with thickness 10% of the initial droplet diameter is formed.

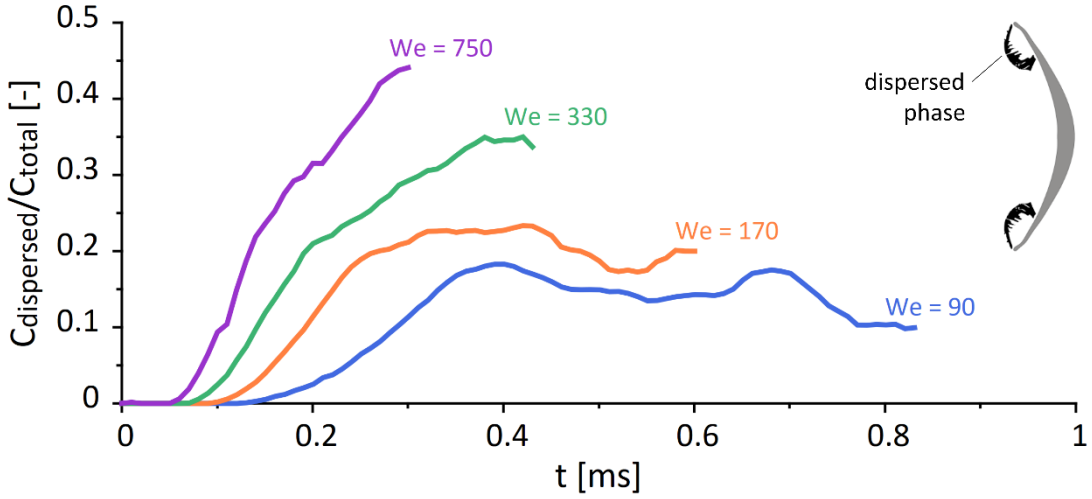


**Figure 4.12** Volume concentration of the dispersed region over the total volume of the liquid phase for the laser-induced droplet fragmentation at We = 90, 170, 330, 750.

An overview of the evolution of the produced fragments inside the polydisperse cloud is depicted in the size distributions in Figures 4.13-4.16 for Weber numbers 90, 170, 330 and 750. During the early stages of the laser-induced droplet rim fragmentation, only large-scaled fragments above 1μm are detected in the volume concentration of the droplet sizes in Figures 4.13(i)-4.16(i) for each examined Weber number; those correspond to the first detached fragments from the rim. Subsequently, more fragments are detached from the rim that enhance the droplets population, while at the same time, the previously formed fragments interact with each other and develop further inside the polydisperse cloud. The modelled sub-grid scale interactions, namely the flow turbulence, the droplet collision and coalescence and the secondary breakup effects, are driven by the developed flow vorticity. Specifically, the moving vortex, which is forming behind the expanding liquid sheet, enhances the local mixing and the slip effects between the small-scaled fragments and the surrounding air and leads to further breakup of the fragments inside the cloud. Additionally, during the evolution of fragmentation, the rim breakup mechanism significantly weakens at lower Weber numbers, as depicted qualitatively in Figures 4.7-4.10; thus, a gradual creation of smaller new fragments is observed with decreasing Weber numbers. Consequently, at the later stages of fragmentation, smaller-scaled fragments below 1 μm dominate the fragments population and become even more significant at lower Weber numbers. For a liquid sheet with thickness 35% of the initial droplet diameter, the probability density functions (PDF) of the fragments sizes in Figures 4.13(ii)-4.16(ii) highlight the predominant presence of sizes between 0.09 μm and 1 μm for each case. However, with an increasing Weber number, the PDFs includes more fragments with diameter above 5 μm; this observation comes in agreement with the more

violent rim breakup, taking place at higher Weber numbers. Eventually, at the final time of the examined rim fragmentation with a corresponding maximum liquid sheet thickness 10% of the initial droplet diameter, small droplets with diameters below 0.5 μm dominate the distributions and significantly less droplets above 1 μm are captured with decreasing Weber number, as depicted in Figures 4.13(iii)-4.16(iii). In coherence with the simulation results, the experimental visualizations of Klein et al. [6] define a minimum ligament size of a few tens of nanometres and depict the dominance of smaller sizes at the final size distribution in the case of a Weber number 90.

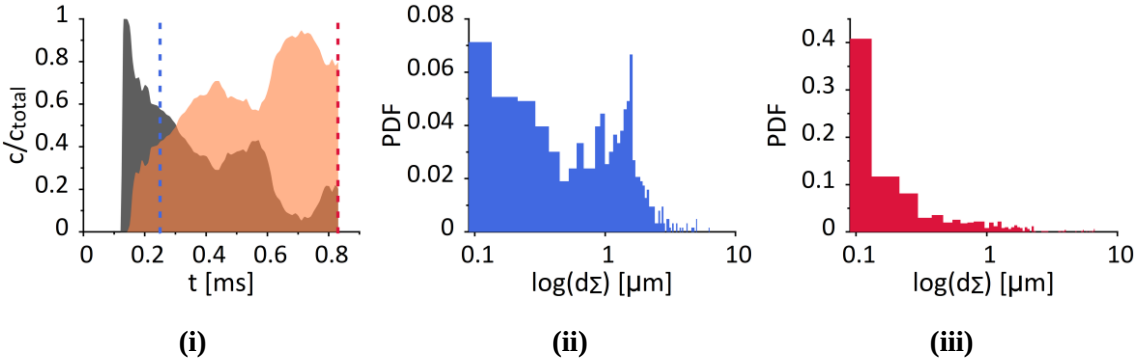


**Figure 4.13** Droplets distribution inside the cloud of fragments at We=90. (i) Volume concentration of the fragments with diameters above 1 μm (in grey) and below 1 μm (in orange) over the total volume of the dispersed region. Probability density function of the fragments sizes for liquid sheet thickness (ii) 35% and (iii) 10% of the initial droplet diameter.

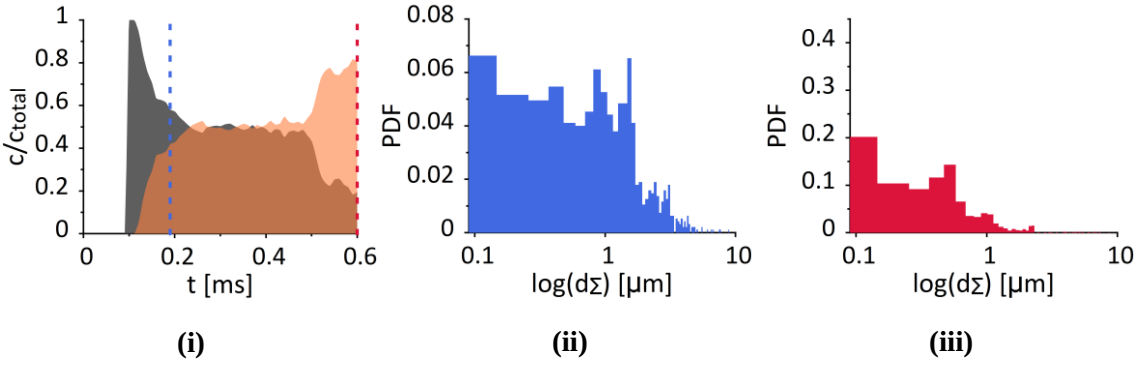


**Figure 4.14** Droplets distribution inside the cloud of fragments at We=170. (i) Volume concentration of the fragments with diameters above 1 μm (in grey) and below 1 μm (in orange) over the total volume of the dispersed region. Probability density function of the fragments sizes for liquid sheet thickness (ii) 35% and (iii) 10% of the initial droplet diameter.

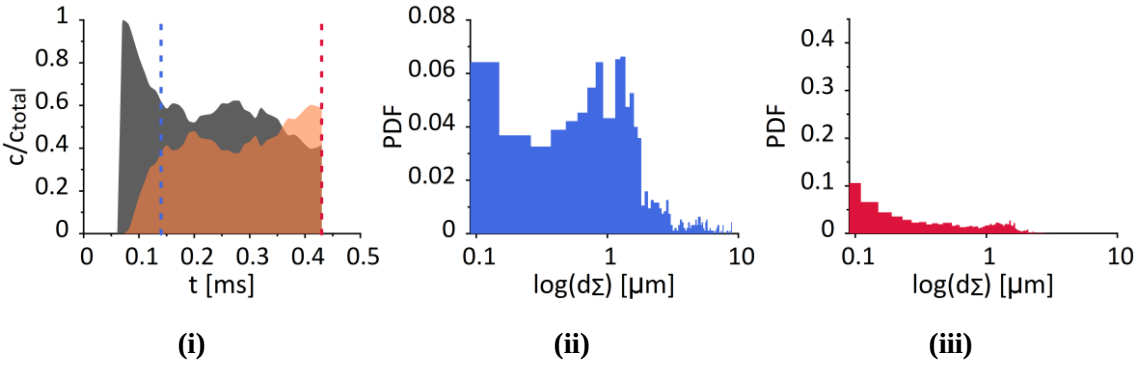


**Figure 4.15** Droplets distribution inside the cloud of fragments at We=330. (i) Volume concentration of the fragments with diameters above 1 µm (in grey) and below 1 µm (in orange) over the total volume of the dispersed region. Probability density function of the fragments sizes for liquid sheet thickness (ii) 35% and (iii) 10% of the initial droplet diameter.

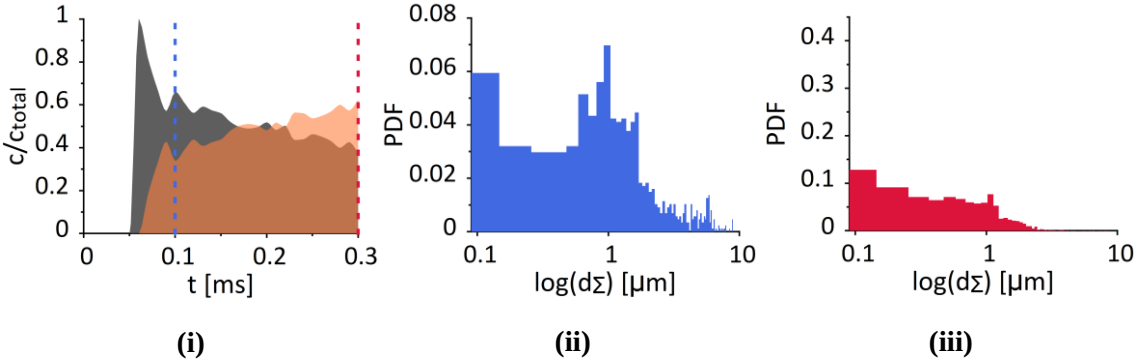


**Figure 4.16** Droplets distribution inside the cloud of fragments at We=750. (i) Volume concentration of the fragments with diameters above 1 µm (in grey) and below 1 µm (in orange) over the total volume of the dispersed region. Probability density function of the fragments sizes for liquid sheet thickness (ii) 35% and (iii) 10% of the initial droplet diameter.

## 4.4 Summary

The laser-induced droplet rim fragmentation for a millimetre-sized MEK droplet has been investigated in the present numerical study, examining a range of Weber numbers between 90 and 750 for the propelled droplet. The problem is characterized by the early-time droplet dynamics, imposed by the millijoule nanosecond laser-pulse impact and the subsequent response of the droplet until it reaches a constant propulsion velocity, and the later-time droplet dynamics, governed by the droplet deformation into an elongated liquid sheet and the resulting rim breakup. The early-time droplet dynamics were simulated within the CFD framework based on the analytical model of Gelderblom et al. [190] and the developed flow fields inside the droplet were obtained. Subsequently, the later-time droplet dynamics were simulated using the multiscale two-fluid approach, which allowed for the consideration of all the scales involved with a viable computational cost. Specifically, the radial expansion of the developed liquid sheet was resolved by the local mesh resolution, using the VOF sharp interface method, while the produced fragments due to the rim breakup were modelled under the diffuse interface approach with consideration of the significant sub-grid scale phenomena inside the cloud of fragments. The simulation results showed a good agreement with the experimental observations of Klein et al. [6] with respect to the shape and the expansion of the elongated liquid sheet and the development of a polydisperse cloud of fragments, until the nucleation of holes on the liquid sheet surface becomes significant and thus, the assumption of an axisymmetric problem is disrupted.

The numerical simulations demonstrated the influence of the Weber number on the initial flow fields inside the droplet and the subsequent droplet deformation and fragmentation, capturing a higher expansion rate, a more uniform liquid sheet thickness and a more extended cloud of fragments at the later stages of fragmentation with increasing Weber numbers. Quantitative information for the radial velocity fields, which are responsible for the droplet expansion, were provided, showing maximum values on the rim. Additionally, during the liquid sheet expansion, the formation of a moving vortex behind the rim was identified, as a result of the interaction between the expanding liquid sheet and the surrounding air; thus, the vortical flow creates a recirculation region for the produced fragments. Finally, an overview of the evolution of the fragments' population, during the droplet rim fragmentation and the sizes distributions at characteristic times of the phenomenon were presented. Overall, larger-scale fragments were detached from the rim at the early stages of fragmentation, while smaller fragments below 1μm

dominated at the later stages, as a result of the further breakup of the secondary droplets inside the cloud of fragments and the gradual decline of the rim breakup mechanism over time.

# 5 CONCLUSIONS AND RECOMMENDATIONS FOR FUTURE WORK

On the present thesis, a compressible Σ-Y two-fluid model with dynamic interface sharpening based on local topological criteria has been developed and implemented in OpenFOAM®. The novel numerical methodology accounts for both compressibility and slip velocity effects. A numerically stable algorithm based on flow topological criteria determines the segregated and dispersed flow regions and applies a sharp and a diffuse interface formulation, respectively. The ability of the fully-Eulerian pressure-based solver to capture intense compressible flows has been validated against a shock tube case. Additionally, the numerical coupling of the two-fluid model with an interface sharpening method has been examined and validated against a benchmark case of a rising bubble.

Firstly, the multiscale framework was utilized for the simulation of a high-speed droplet impact with Weber number above $10^5$ and validated against new experimental data. The model functionality to operate between two different formulations based on the examined flow regime was demonstrated and the transition criteria of the topology algorithm were evaluated against typical criteria in the literature that define the initiation of breakup. The developed model accurately captured the macroscopic fragmentation of the droplet and the shock waves development inside the coherent droplet and the surrounding air after impact. For the first time, the fragments produced due to the high-speed impact were quantified based on the sub-grid scale modelling and information which are not available from the experimental observation were obtained.

Secondly, the aerodynamic breakup of a water-like droplet under the SIE regime, imposed by three different shock waves with Mach numbers 1.21, 1.46 and 2.64, was investigated using the developed multiscale two-fluid approach. During the early stages of aerobreakup, the numerical results accurately captured the macroscopic droplet deformation, the dominant wakes behind the

droplet and the stripping action from the droplet surface, as observed in the experiments. Two stripping mechanisms were identified to act on the coherent droplet surface. The main stripping mechanism is responsible for the formation of the primary stream of fragments, detached from the droplet equator and the droplet flattened backside, while the secondary stripping mechanism is present on the droplet frontside and becomes more significant at supersonic post-shock conditions. During the later stages of fragmentation, the evolution of the secondary droplets inside the dense mist was quantified and analysed based on the modelled sub-grid scale mechanisms. The influence of the incident shock Mach number on the mist developed was demonstrated, resulting to a narrower mist with more large-scaled structures with higher Mach numbers.

Finally, the laser-induced droplet rim fragmentation for a millimetre-sized MEK droplet was investigated with the multiscale two-fluid approach, examining a range of Weber numbers between 90 and 750 for the propelled droplet. Both the early-and later-time response of the MEK droplet to the laser pulse were captured by the model with the macroscopic droplet deformation and rim breakup to show good agreement with the experimental observations. The numerical simulations demonstrated the influence of the laser energy on the initial flow fields inside the droplet and the subsequent droplet deformation and fragmentation, capturing a higher expansion rate, a more uniform liquid sheet thickness and a more extended cloud of fragments at the later stages of fragmentation with increasing laser energy. An overview of the evolution of the fragments in the course of the rim breakup was presented based on the sub-grid scale modelling and size distributions were obtained; this information cannot be easily extracted from the experimental data due to the formation of a polydisperse cloud of micron-scale fragments.

Overall, the developed multiscale two-fluid approach consists of a useful numerical tool for both engineering and more fundamental applications with a multiscale character, providing physically consistent simulations with a viable computational cost. Therefore, the developed model can be the foundation of a complex framework of case-dependent sub-grid scale models. Specifically, the validation and calibration of the utilized sub-grid scale models and the implementation of additional models for unconsidered sub-grid scale mechanisms can provide an extended database of models that will be activated based on the examined flow conditions. Within this framework, complex flow fields that concern different materials and dominant sub-grid scale interactions, such as the fluidized beds applications [194], [195], can be accurately predicted.

Additionally, the implementation of cavitation and vaporization models within the developed multiscale framework can allow for a full-scale analysis of flow fields with dominant phase change phenomena, which is not available in the literature due to the prohibitive computational

cost. Specifically, the simulation of a liquid spray atomization [17], [18], starting from the in-nozzle flow and up to the secondary atomization regime and thus, accounting for the in-nozzle cavitation, the secondary droplets vaporization and all the scales involved, would be feasible. Similarly, in medical applications, a full-scale simulation of aerosols [196] with the consideration of the produced micron-droplets at the exit of the inhaler, the vaporization and downstream droplets interactions could be obtained using the sub-gid scale modelling. The implementation of more advanced equations of state in the form of tabulated data [197] or the PC-SAFT [198] equation of state would be useful for the simulations of flow fields with significant thermodynamics, including cavitation-driven processes, i.e. primary spray atomization with in-nozzle cavitation [199] and laser-induced droplet fragmentation with significantly high laser beam energy [6], supercritical sprays [200], and fragmentation of droplets other than water, i.e., ouzo droplets [201].

Finally, a valuable addition to the model would be the implementation and coupling of an adaptive mesh refinement (AMR) method within the VOF formation in order to be able to capture the examined interfaces with an increased resolution and perform computationally demanding 3D simulations. With this implementation, the currently presented simulations of a high-speed droplet impact and a droplet aerobreakup could be performed in a 3D computational domain with a viable computational cost in order to investigate the effect of the fully developed turbulence and the non-axisymmetric features of droplet fragmentation. With respect to the laser-induced droplet fragmentation case, the AMR method would allow for a locally increased resolution on the deforming liquid sheet and thus, the simulation of the process until later stages and the prediction of the non-axisymmetric hole nucleation on the sheet surface would be feasible.

# 6 PUBLICATIONS

### Peer-Reviewed Journal Publications (newest first)

- G. Nykteri and M. Gavaises, "Droplet Aerobreakup under the Shear-Induced Entrainment Regime Using a Multiscale Two-Fluid Approach", *Physical Review Fluids,* vol. 6, p. 084304, 2021.

- G. Nykteri, P. Koukouvinis, R. S. Gonzalez Avila, C.-D. Ohl, and M. Gavaises, "A Σ-Y two-fluid model with dynamic local topology detection : Application to high-speed droplet impact," *Journal of Computational. Physics*, vol. 408, p. 109225, 2020.

### Pending Journal Publications

- G. Nykteri and M. Gavaises, "Numerical modelling of droplet rim fragmentation by laser-pulse impact using a multiscale two-fluid approach", awaiting publication.

### Conference Proceedings (newest first)

- G. Nykteri, P. Koukouvinis, R. S. Gonzalez Avila, C.-D. Ohl, and M. Gavaises, "Numerical investigation of high-speed droplet impact using a multiscale two- fluid approach," in *ILASS Europe 2019, 29th European Conference on Liquid Atomization and Spray Systems*, 2019.

- G. Nykteri, P. Koukouvinis, and M. Gavaises, "A compressible Σ-Y two-fluid atomization model with dynamic interface sharpening based on flow topology detection," in *ICLASS 2018, 14th international conference on liquid atomization & spray systems*, 2018.

# 7 BIBLIOGRAPHY

[1] R. Saurel, F. Petitpas, and R. Abgrall, *Modelling Phase Transition in Metastable Liquids: Application to Cavitating and Flashing Flows*, Vol. 607 (2008).

[2] S. Hysing, S. Turek, D. Kuzmin, N. Parolini, E. Burman, S. Ganesan, and L. Tobiska, *Quantitative Benchmark Computations of Two-Dimensional Bubble Dynamics*, Int. J. Numer. Methods Fluids **60**, 1259 (2009).

[3] L. Štrubelj, I. Tiselj, and B. Mavko, *Simulations of Free Surface Flows with Implementation of Surface Tension and Interface Sharpening in the Two-Fluid Model*, Int. J. Heat Fluid Flow **30**, 741 (2009).

[4] T. G. Theofanous, V. V. Mitkin, C. L. Ng, C. H. Chang, X. Deng, and S. Sushchikh, *The Physics of Aerobreakup. II. Viscous Liquids*, Phys. Fluids **24**, 022104 (2012).

[5] T. G. Theofanous, *Aerobreakup of Newtonian and Viscoelastic Liquids*, Annu. Rev. Fluid Mech. **43**, 661 (2011).

[6] A. L. Klein, D. Kurilovich, H. Lhuissier, O. O. Versolato, D. Lohse, E. Villermaux, and H. Gelderblom, *Drop Fragmentation by Laser-Pulse Impact*, J. Fluid Mech. **893**, (2020).

[7] E. Villermaux and B. Bossa, *Drop Fragmentation on Impact*, J. Fluid Mech. **668**, 412 (2011).

[8] E. Villermaux, *Fragmentation*, Ann. Rev. Fluid Mech. **39**, 419 (2007).

[9] A. L. N. Moreira, A. S. Moita, and M. R. Panão, *Advances and Challenges in Explaining Fuel Spray Impingement: How Much of Single Droplet Impact Research Is Useful?*, Prog. Energy Combust. Sci. **36**, 554 (2010).

[10] N. Liu, Z. Wang, M. Sun, H. Wang, and B. Wang, *Numerical Simulation of Liquid Droplet Breakup in Supersonic Flows*, Acta Astronaut. **145**, 116 (2018).

[11] C. Wagner and N. Harned, *EUV Lithography: Lithography Gets Extreme*, Nat. Photonics **4**, 24 (2010).

[12] J. Benschop, V. Banine, S. Lok, and E. Loopstra, *Extreme Ultraviolet Lithography: Status*

*and Prospects*, J. Vac. Sci. Technol. B Microelectron. Nanom. Struct. **26**, 2204 (2008).

[13] A. L. Klein, Laser Impact on Flying Drops, University of Twente, 2017.

[14] ExxonMobil. The Outlook for Energy: A View to 2040, 2019.

[15] Heavy Duty Diesel Emissions Guide, Europe, USA and Japan, Johnson Matthey, 2012.

[16] R. Nicolas, *Euro 6 Regulation for Automotive Explained*, https://www.car-engineer.com/euro-6-regulation-automotive-explained/.

[17] M. Gorokhovski and M. Herrmann, *Modeling Primary Atomization*, Annual Review of Fluid Mechanics.

[18] D. R. Guildenbecher, C. Lopez-Rivera, and P. E. Sojka, *Secondary Atomization*, Exp. Fluids **46**, 371 (2009).

[19] J. Oefelein, G. Lacaze, R. Dahms, A. Ruiz, and A. Misdariis, *Effects of Real-Fluid Thermodynamics on High-Pressure Fuel Injection Processes*, SAE Int. J. Engines **7**, 2014 (2014).

[20] M. Birouk and L. Nebojsa, *Liquid Jet Break-up in Quiescent Atmosphere: A Review*, At. Sprays **19**, 501 (2009).

[21] M. Minniti, A. Ziaee, D. Curran, J. Porter, T. Parker, and D. Dunn-Rankin, *Ultra-Short Pulse Off-Axis Digital Holography Imaging under Realistic Diesel Spray Conditions*, ICLASS 2018, 14th Int. Conf. Liq. At. Spray Syst. (2018).

[22] E. T. Curran, W. H. Heiser, and D. T. Pratt, *Fluid Phenomena in Scramjet Combustion Systems*, Annu. Rev. Fluid Mech. **28**, 323 (1996).

[23] S. Nakaya, Y. Hikichi, Y. Nakazawa, K. Sakaki, M. Choi, M. Tsue, M. Kono, and S. Tomioka, *Ignition and Supersonic Combustion Behavior of Liquid Ethanol in a Scramjet Model Combustor with Cavity Flame Holder*, Proc. Combust. Inst. **35**, 2091 (2015).

[24] J. C. Meng and T. Colonius, *Numerical Simulation of the Aerobreakup of a Water Droplet*, J. Fluid Mech. **835**, 1108 (2018).

[25] G. E. Moore, *Progress in Digital Integrated Electronics [Technical Literaiture, Copyright 1975 IEEE. Reprinted, with Permission. Technical Digest. International Electron Devices Meeting, IEEE, 1975, Pp. 11-13.]*, IEEE Solid-State Circuits Soc. Newsl. **11**, 36 (2009).

[26] N. Mojarad, J. Gobrecht, Y. E.-S. reports, and undefined 2015, *Beyond EUV Lithography:*

*A Comparative Study of Efficient Photoresists' Performance*, Nature.Com (n.d.).

[27] N. I. Kolev, *Multiphase Flow Dynamics 2. Thermal and Mechanical Interactions*, 3rd ed. (Springer-Verlag Berlin Heidelberg, 2007).

[28] K. Schügerl and K.-H. Bellgardt, *Bioreaction Engineering: Modeling and Control.*, 1st ed. (Springer-Verlag Berlin Heidelberg, 2000).

[29] D. H. Sharp, *An Overview of Rayleigh-Taylor Instability*, in *International Conference on "Fronts, Interfaces and Patterns"* (1983).

[30] M. Ishii and T. Hibiki, *Thermo-Fluid Dynamics of Two-Phase Flow*, 2nd ed. (Springer-Verlag New York, 2011).

[31] J. Dukowicz, *A Particle-Fluid Numerical Model for Liquid Sprays*, J. Comput. Phys. **35**, 229 (1980).

[32] A. Berlemont, P. Desjonqueres, and G. Gouesbet, *Particle Lagrangian Simulation in Turbulent Flows*, Int. J. Multiph. Flow **16**, 19 (1990).

[33] M. Boileau, T. J. Poinsot, M. Cazalens, E. Riber, B. Cuenot, L. Y. M. Gicquel, and S. Pascaud, *Investigation of Two-Fluid Methods for Large Eddy Simulation of Spray Combustion in Gas Turbines*, Flow, Turbul. Combust. **80**, 291 (2008).

[34] M. A. Gorokhovski and V. L. Saveliev, *Analyses of Kolmogorov's Model of Breakup and Its Application into Lagrangian Computation of Liquid Sprays under Air-Blast Atomization*, Phys. Fluids **15**, 184 (2003).

[35] D. A. Drew, *Mathematical Modeling of Two-Phase Flow.*, Vol. 50 (1983).

[36] P. Koukouvinis, M. Gavaises, J. Li, and L. Wang, *Large Eddy Simulation of Diesel Injector Including Cavitation Effects and Correlation to Erosion Damage*, Fuel **175**, 26 (2016).

[37] Y. Pei, S. Som, E. Pomraning, P. K. Senecal, S. A. Skeen, J. Manin, and L. M. Pickett, *Large Eddy Simulation of a Reacting Spray Flame with Multiple Realizations under Compression Ignition Engine Conditions.*, Combust. Flame **162**, 4442 (2015).

[38] M. Ishii and K. Mishima, *Two-Fluid Model and Hydrodynamic Constitutive Relations*, Nucl. Eng. Des. **82**, 107 (1984).

[39] H. Rusche, Computational Fluid Dynamics of Dispersed Two-Phase Flows at High Phase

Fractions, 2002.

[40] D. Rossinelli, B. Hejazialhosseini, P. Hadjidoukas, C. Bekas, A. Curioni, A. Bertsch, S. Futral, S. J. Schmidt, N. A. Adams, and P. Koumoutsakos, *11 PFLOP/s Simulations of Cloud Cavitation Collapse*, in *Proceedings of the International Conference on High Performance Computing, Networking, Storage and Analysis* (2013), pp. 1–13.

[41] M. Gorokhovski and M. Herrmann, *Modeling Primary Atomization*, Annu. Rev. Fluid Mech. **40**, 343 (2008).

[42] M. Herrmann, *Detailed Numerical Simulations of the Primary Atomization of a Turbulent Liquid Jet in Crossflow*, J. Eng. Gas Turbines Power **132**, 061506 (2010).

[43] J. Shinjo and A. Umemura, *Simulation of Liquid Jet Primary Breakup: Dynamics of Ligament and Droplet Formation*, Int. J. Multiph. Flow **36**, 513 (2010).

[44] J. Shinjo and A. Umemura, *Surface Instability and Primary Atomization Characteristics of Straight Liquid Jet Sprays*, Int. J. Multiph. Flow **37**, 1294 (2011).

[45] C. W. Hirt and B. D. Nichols, *Volume of Fluid (VOF) Method for the Dynamics of Free Boundaries*, J. Comput. Phys. **39**, 201 (1981).

[46] R. Scardovelli and S. Zaleski, *Direct Numerical Simulation of Free-Surface and Interfacial Flow*, Annu. Rev. Fluid Mech. **31**, 567 (1999).

[47] S. Osher and R. Fedkiw, *Level Set Methods and Dynamic Implicit Surfaces*, Vol. 153 (Springer Science & Business Media, 2006).

[48] J. A. Sethian, *A Fast Marching Level Set Method for Monotonically Advancing Fronts.*, Proc. Natl. Acad. Sci. **93**, 1591 (1996).

[49] R. P. Fedkiw, T. Aslam, B. Merriman, and S. Osher, *A Non-Oscillatory Eulerian Approach to Interfaces in Multimaterial Flows (the Ghost Fluid Method)*, J. Comput. Phys. **152**, 457 (1999).

[50] S. O. Unverdi and G. Tryggvason, *A Front-Tracking Method for Viscous, Incompressible, Multi-Fluid Flows*, J. Comput. Phys. **100**, 25 (1992).

[51] G. Tryggvason, B. Bunner, A. Esmaeeli, D. Juric, N. Al-Rawahi, W. Tauber, J. Han, S. Nas, and Y.-J. Jan, *A Front-Tracking Method for the Computations of Multiphase Flow*, J. Comput. Phys. **169**, 708 (2002).

[52] A. Vallet, A. A. Burluka, and R. Borghi, *Development of a Eulerian Model for the "Atomization" of a Liquid Jet*, At. Sprays **11**, (2001).

[53] A. Vallet and R. Borghi, *Modelisation Eulerienne de l'atomisation d'un Jet Liquide*, Comptes Rendus l'Académie Des Sci. IIB-Mechanics-Physics-Astronomy **327**, 1015 (1999).

[54] F. E. Marble and J. E. Broadwell, *The Coherent Flame Model of the Turbulent Chemical Reactions*, Acta Astronaut. **4**, 291 (1977).

[55] R. Lebas, T. Menard, P. A. Beau, A. Berlemont, and F. X. Demoulin, *Numerical Simulation of Primary Break-up and Atomization: DNS and Modelling Study*, Int. J. Multiph. Flow **35**, 247 (2009).

[56] A. Andreini, C. Bianchini, S. Puggelli, and F. X. Demoulin, *Development of a Turbulent Liquid Flux Model for Eulerian-Eulerian Multiphase Flow Simulations*, Int. J. Multiph. Flow **81**, 88 (2016).

[57] J. Anez, A. Ahmed, N. Hecht, B. Duret, J. Reveillon, and F. X. Demoulin, *Eulerian–Lagrangian Spray Atomization Model Coupled with Interface Capturing Method for Diesel Injectors*, Int. J. Multiph. Flow (2018).

[58] D. L. Marchisio, J. T. Pikturna, R. O. Fox, R. D. Vigil, and A. A. Barresi, *Quadrature Method of Moments for Population-Balance Equations*, AIChE J. **49**, 1266 (2003).

[59] S. Navarro-Martinez, *Large Eddy Simulation of Spray Atomization with a Probability Density Function Method*, Int. J. Multiph. Flow **63**, 11 (2014).

[60] AVL, *FIRE V2013 Manuals* (Graz, Austria, AVL LIST GmbH, 2013).

[61] M. Vujanović, Z. Petranović, W. Edelbauer, J. Baleta, and N. Duić, *Numerical Modelling of Diesel Spray Using the Eulerian Multiphase Approach*, Energy Convers. Manag. **104**, 160 (2015).

[62] K. E. Wardle and H. G. Weller, *Hybrid Multiphase CFD Solver for Coupled Dispersed/Segregated Flows in Liquid-Liquid Extraction*, Int. J. Chem. Eng. **2013**, (2013).

[63] O. Y. Shonibare and K. E. Wardle, *Numerical Investigation of Vertical Plunging Jet Using a Hybrid Multifluid-VOF Multiphase CFD Solver*, Int. J. Chem. Eng. **2015**, (2015).

[64] S. G. Kandlikar and A. V. Bapat, *Evaluation of Jet Impingement, Spray and Microchannel Chip Cooling Options for High Heat Flux Removal*, Heat Transf. Eng. **28**, 911 (2007).

[65] K. L. Pan, K. C. Tseng, and C. H. Wang, *Breakup of a Droplet at High Velocity Impacting a Solid Surface*, Exp. Fluids **48**, 143 (2010).

[66] C. W. Visser, Y. Tagawa, C. Sun, and D. Lohse, *Microdroplet Impact at Very High Velocity*, Soft Matter **8**, 10732 (2012).

[67] C. Antonini, A. Amirfazli, and M. Marengo, *Drop Impact and Wettability: From Hydrophilic to Superhydrophobic Surfaces*, Phys. Fluids **24**, (2012).

[68] I. V. Roisman, A. Lembach, and C. Tropea, *Drop Splashing Induced by Target Roughness and Porosity: The Size Plays No Role*, Adv. Colloid Interface Sci. **222**, 615 (2015).

[69] G. Liang and I. Mudawar, *Review of Drop Impact on Heated Walls*, Int. J. Heat Mass Transf. **106**, 103 (2017).

[70] M. Rein, *Phenomena of Liquid Drop Impact on Solid and Liquid Surfaces*, Fluid Dyn. Res. **12**, 61 (1993).

[71] A. L. Yarin, *DROP IMPACT DYNAMICS: Splashing, Spreading, Receding, Bouncing…*, Annu. Rev. Fluid Mech. **38**, 159 (2006).

[72] C. Josserand and S. T. Thoroddsen, *Drop Impact on a Solid Surface*, Annu. Rev. Fluid Mech. **48**, 365 (2016).

[73] T. Ma, L. Feng, H. Wang, H. Liu, and M. Yao, *A Numerical Study of Spray/Wall Impingement Based on Droplet Impact Phenomenon*, Int. J. Heat Mass Transf. **112**, 401 (2017).

[74] V. Bertola, *An Impact Regime Map for Water Drops Impacting on Heated Surfaces*, Int. J. Heat Mass Transf. **85**, 430 (2015).

[75] A. L. Yarin and D. A. Weiss, *Impact of Drops on Solid Surfaces: Self-Similar Capillary Waves, and Splashing as a New Type of Kinematic Discontinuity*, J. Fluid Mech. **283**, 141 (1995).

[76] K. Range and F. Feuillebois, *Influence of Surface Roughness on Liquid Drop Impact*, J. Colloid Interface Sci. **203**, 16 (1998).

[77] C. Mundo, M. Sommerfeld, and C. Tropea, *Droplet-Wall Collisions: Experimental Studies of the Deformation and Breakup Process*, Int. J. Multiph. Flow **21**, 151 (1995).

[78] G. E. Cossali, M. Santini, and M. Marengo, *Single-Drop Empirical Models for Spray*

*Impact on Solid Walls: A Review*, At. Sprays **15**, 699 (2005).

[79] A. M. Worthington, *XXVIII. On the Forms Assumed by Drops of Liquids Falling Vertically on a Horizontal Plate*, Proc. R. Soc. London **25**, 261 (1877).

[80] S. T. Thoroddsen, T. G. Etoh, and K. Takehara, *High-Speed Imaging of Drops and Bubbles*, Annu. Rev. Fluid Mech. **40**, 257 (2008).

[81] L. Xu, W. W. Zhang, and S. R. Nagel, *Drop Splashing on a Dry Smooth Surface*, Phys. Rev. Lett. **94**, 1 (2005).

[82] C. W. Visser, P. E. Frommhold, S. Wildeman, R. Mettin, D. Lohse, and C. Sun, *Dynamics of High-Speed Micro-Drop Impact: Numerical Simulations and Experiments at Frame-to-Frame Times below 100 Ns*, Soft Matter **11**, 1708 (2015).

[83] S. T. Thoroddsen, K. Takehara, and T. G. Etoh, *Micro-Splashing by Drop Impacts*, J. Fluid Mech. **706**, 560 (2012).

[84] J. E. Field, J. P. Dear, and J. E. Ogren, *The Effects of Target Compliance on Liquid Drop Impact*, J. Appl. Phys. **65**, 533 (1989).

[85] I. Malgarinos, N. Nikolopoulos, M. Marengo, C. Antonini, and M. Gavaises, *VOF Simulations of the Contact Angle Dynamics during the Drop Spreading: Standard Models and a New Wetting Force Model*, Adv. Colloid Interface Sci. **212**, 1 (2014).

[86] Y. Guo, Y. Lian, and M. Sussman, *Investigation of Drop Impact on Dry and Wet Surfaces with Consideration of Surrounding Air*, Phys. Fluids **28**, (2016).

[87] Z. Wu and Y. Cao, *Dynamics of Initial Drop Splashing on a Dry Smooth Surface*, PLoS One **12**, 1 (2017).

[88] K. K. Haller, Y. Ventikos, D. Poulikakos, and P. Monkewitz, *Computational Study of High-Speed Liquid Droplet Impact*, J. Appl. Phys. **92**, 2821 (2002).

[89] Y. Y. Niu and H. W. Wang, *Simulations of the Shock Waves and Cavitation Bubbles during a Three-Dimensional High-Speed Droplet Impingement Based on a Two-Fluid Model*, Comput. Fluids **134**–**135**, 196 (2016).

[90] N. Kyriazis, P. Koukouvinis, and M. Gavaises, *Modelling Cavitation during Drop Impact on Solid Surfaces*, Adv. Colloid Interface Sci. **260**, 46 (2018).

[91] W. Wu, G. Xiang, and B. Wang, *On High-Speed Impingement of Cylindrical Droplets*

*upon Solid Wall Considering Cavitation Effects*, J. Fluid Mech. **857**, 851 (2018).

[92] J. Boussinesq, *Essai Sur La Théorie Des Eaux Courantes*, Mémoires Présentés Par Divers Savants à l'Académie Des Sci. **23**, 1 (1877).

[93] R. T. Lahey, *The Simulation of Multidimensional Multiphase Flows*, Nucl. Eng. Des. **235**, 1043 (2005).

[94] M. J. Ivings, D. M. Causon, and E. F. Toro, *On Riemann Solvers for Compressible Liquids*, Int. J. Numer. Methods Fluids **28**, 395 (1998).

[95] S. A. Beig, B. Aboulhasanzadeh, and E. Johnsen, *Temperatures Produced by Inertially Collapsing Bubbles near Rigid Surfaces*, J. Fluid Mech. **852**, 105 (2018).

[96] S. S. Deshpande, L. Anumolu, and M. F. Trujillo, *Evaluating the Performance of the Two-Phase Flow Solver InterFoam*, Comput. Sci. Discov. **5**, 014016 (2012).

[97] M. Jadidi, M. Tembely, S. Moghtadernejad, and A. Dolatabadi, *Coupled Level Set and Volume of Fluid Method in OpenFoam with Application to Compressible Two-Phase Flow*, in *22nd Annual Conference of the CFD Society of Canada* (2014).

[98] J. Chesnel, J. Reveillon, T. Menard, and F. X. Demoulin, *Large Eddy Simulation of Liquid Jet Atomization*, At. Sprays **21**, 711 (2011).

[99] G. Černe, S. Petelin, and I. Tiselj, *Coupling of the Interface Tracking and the Two-Fluid Models for the Simulation of Incompressible Two-Phase Flow*, J. Comput. Phys. **171**, 776 (2001).

[100] L. Strubelj and I. Tiselj, *Two-Fluid Model with Interface Sharpening*, Int. J. Numer. Methods Eng. **85**, 575 (2011).

[101] J. U. Brackbill, D. B. Kothe, and C. Zemach, *A Continuum Method for Modeling Surface Tension*, J. Comput. Phys. **100**, 335 (1992).

[102] H. Marschall, Technische Universität München Lehrstuhl I Für Technische Chemie Towards the Numerical Simulation of Multi-Scale Two-Phase Flows, 2011.

[103] L. Schiller and A. Z. Naumann, *Über Die Grundlegenden Berechnungen Bei Der Schwerkraftaufbereitung*, Ver. Deut. Ing. **77**, 318 (1933).

[104] M. Ishii and N. Zuber, *Drag Coefficient and Relative Velocity in Bubbly, Droplet or Particulate Flows*, AIChE J. **25**, 843 (1979).

[105] A. Tomiyama and N. Shimada, *A Numerical Method for Bubbly Flow Simulation Based on a Multi-Fluid Model*, J. Press. Vessel Technol. **123**, 510 (2001).

[106] G. I. Kelbaliyev, *Drag Coefficients of Variously Shaped Solid Particles, Drops, and Bubbles*, Theor. Found. Chem. Eng. **45**, 248 (2011).

[107] F.-X. Demoulin, P.-A. Beau, G. Blokkeel, A. Mura, and R. Borghi, *A New Model for Turbulent Flows with Large Density Fluctuations: Application to Liquid Atomization*, At. Sprays **17(4)**, 315 (2007).

[108] J. M. García-Oliver, J. M. Pastor, A. Pandal, N. Trask, E. Baldwin, and D. P. Schmidt, *Diesel Spray CFD Simulations Based on the Σ-Y Eulerian Atomization Modely*, At. Sprays **23**, 71 (2013).

[109] R. Clift, J. Grace, and M. Weber, *Bubbles, Drops, and Particles* (Courier Corporation, 2005).

[110] D. Bhaga and M. E. Weber, *Bubbles in Viscous Liquids: Shapes, Wakes and Velocities*, J. Fluid Mech. **105**, 61 (1981).

[111] A. Tomiyama, G. P. Celata, S. Hosokawa, and S. Yoshida, *Terminal Velocity of Single Bubbles in Surface Tension Force Dominant Regime*, Int. J. Multiph. Flow **28**, 1497 (2002).

[112] R. D. Reitz and R. Diwakar, *Effect of Drop Breakup on Fuel Sprays*, SAE Trans. 218 (1986).

[113] E. Abo-Serie, C. Arcoumanis, and M. Gavaises., *Spray Characterisation of Swirl Pressure Atomizers for G-DI Engines: Phase Doppler Measurements.*, in *Proceedings of ILASS-Europe, Darmstadt, Germany* (2000), pp. 11–13.

[114] A. E. S. E. T. Alajmi, N. M. Adam, A. A. Hairuddin, and L. C. Abdullah, *Fuel Atomization in Gas Turbines: A Review of Novel Technology*, Int. J. Energy Res. **43**, 3166 (2019).

[115] M. A. Benjamin, R. J. Jensen, and M. Arienti, *Review of Atomization: Current Knowledge and Future Requirements for Propulsion Combustors*, At. Sprays **20**, 485 (2010).

[116] R. N. Dahms and J. C. Oefelein, *Atomization and Dense-Fluid Breakup Regimes in Liquid Rocket Engines*, J. Propuls. Power **31**, 1221 (2015).

[117] B. E. Gelfand, *Droplet Breakup Phenomena in Flows with Velocity Lag*, Prog. Energy Combust. Sci. **22**, 201 (1996).

[118] O. Gohardani, *Impact of Erosion Testing Aspects on Current and Future Flight Conditions*, Prog. Aerosp. Sci. **47**, 280 (2011).

[119] J. O. Hinze, *Fundamentals of the Hydrodynamic Mechanism of Splitting in Dispersion Processes*, AIChE J. **1**, 289 (1955).

[120] M. Pilch and C. A. Erdman, *Use of Breakup Time Data and Velocity History Data to Predict the Maximum Size of Stable Fragments for Acceleration-Induced Breakup of a Liquid Drop*, Int. J. Multiph. Flow **13**, 741 (1987).

[121] G. M. Faeth, L.-P. Hsiang, and P.-K. Wu, *Structure and Break-up Properties of Sprays*, Int. J. Multiph. Flow **21**, 99 (1995).

[122] D. Stefanitsis, G. Strotos, N. Nikolopoulos, E. Kakaras, and M. Gavaises, *Improved Droplet Breakup Models for Spray Applications*, Int. J. Heat Fluid Flow **76**, 274 (2019).

[123] D. Stefanitsis, G. Strotos, N. Nikolopoulos, and M. Gavaises, *Numerical Investigation of the Aerodynamic Breakup of a Parallel Moving Droplet Cluster*, Int. J. Multiph. Flow **121**, 103123 (2019).

[124] D. Stefanitsis, I. Malgarinos, G. Strotos, N. Nikolopoulos, E. Kakaras, and M. Gavaises, *Numerical Investigation of the Aerodynamic Breakup of Droplets in Tandem*, Int. J. Multiph. Flow **113**, 289 (2019).

[125] T. G. Theofanous, G. J. Li, and T. N. Dinh, *Aerobreakup in Rarefied Supersonic Gas Flows*, J. Fluids Eng. **126**, 516 (2004).

[126] O. G. Engel, *Fragmentation of Waterdrops in the Zone behind an Air Shock*, J. Res. Natl. Bur. Stand. (1934). **60**, 245 (1958).

[127] J. A. Nicnolls and A. A. Ranger, *Aerodynamic Shattering of Liquid Drops*, AIAA J. **7**, 285 (1969).

[128] A. Wierzba and K. Takayama, *Experimental Investigation of the Aerodynamic Breakup of Liquid Drops*, AIAA J. **26**, 1329 (1988).

[129] T. Yoshida and K. Takayama, *Interaction of Liquid Droplets with Planar Shock Waves*, J. Fluids Eng. Trans. ASME **112**, 481 (1990).

[130] T. G. Theofanous and J. G. Li, *On the Physics of Aerobreakup*, Phys. Fluids **20**, 052103 (2008).

[131] T. G. Theofanous, V. V. Mitkin, and C. L. Ng, *The Physics of Aerobreakup. III. Viscoelastic Liquids*, Phys. Fluids **25**, 032101 (2013).

[132] V. V. Mitkin and T. G. Theofanous, *The Physics of Aerobreakup. IV. Strain-Thickening Liquids*, Phys. Fluids **29**, 122101 (2017).

[133] Z. Wang, T. Hopfes, M. Giglmaier, and N. A. Adams, *Effect of Mach Number on Droplet Aerobreakup in Shear Stripping Regime*, Exp. Fluids **61**, 1 (2020).

[134] D. Hébert, J.-L. Rullier, J.-M. Chevalier, I. Bertron, E. Lescoute, F. Virot, and H. El-Rabii, *Investigation of Mechanisms Leading to Water Drop Breakup at Mach 4.4 and Weber Numbers above 105*, SN Appl. Sci. **2**, 1 (2020).

[135] L. P. Hsiang and G. M. Faeth, *Near-Limit Drop Deformation and Secondary Breakup*, Int. J. Multiph. Flow **18**, 635 (1992).

[136] L. P. Hsiang and G. M. Faeth, *Drop Properties after Secondary Breakup*, Int. J. Multiph. Flow **19**, 721 (1993).

[137] L. P. Hsiang and G. M. Faeth, *Droplet Deformation Due To Shock Wave and Steady Disturbances*, Int. J. Multiph. Flow **21**, 545 (1995).

[138] Z. Xu, T. Wang, and Z. Che, *Droplet Deformation and Breakup in Shear Flow of Air*, Phys. Fluids **32**, 052109 (2020).

[139] H. Chen, *Two-Dimensional Simulation of Stripping Breakup of a Water Droplet*, AIAA J. **46**, 1135 (2008).

[140] R. Saurel and R. Abgrall, *Simple Method for Compressible Multifluid Flows*, SIAM J. Sci. Comput. **21**, 1115 (1999).

[141] D. Igra and K. Takayama, *A Study of Shock Wave Loading on a Cylindrical Water Column*, Rep. Inst. Fluid Sci. Tohoku Univ. **13**, 19 (2001).

[142] G. Allaire, S. Clerc, and S. Kokh, *A Five-Equation Model for the Simulation of Interfaces between Compressible Fluids*, J. Comput. Phys. **181**, 577 (2002).

[143] J. C. Meng and T. Colonius, *Numerical Simulations of the Early Stages of High-Speed Droplet Breakup*, Shock Waves **25**, 399 (2015).

[144] S. Sembian, M. Liverts, N. Tillmark, and N. Apazidis, *Plane Shock Wave Interaction with a Cylindrical Water Column*, Phys. Fluids **28**, 056102 (2016).

[145] H. Yang and J. Peng, *Numerical Study of the Shear-Thinning Effect on the Interaction between a Normal Shock Wave and a Cylindrical Liquid Column*, Phys. Fluids **31**, 043101 (2019).

[146] J. W. J. Kaiser, J. M. Winter, S. Adami, and N. A. Adams, *Investigation of Interface Deformation Dynamics during High-Weber Number Cylindrical Droplet Breakup*, Int. J. Multiph. Flow **132**, 103409 (2020).

[147] D. Igra and K. Takayama, *Numerical Simulation of Shock Wave Interaction with a Water Column*, Shock Waves **11**, 219 (2001).

[148] D. Igra and K. Takayama, *Investigation of Aerodynamic Breakup of a Cylindrical Water Droplet*, At. Sprays **11**, 167 (2001).

[149] D. Stefanitsis, P. Koukouvinis, N. Nikolopoulos, and M. Gavaises, *Numerical Investigation of the Aerodynamic Droplet Breakup at Mach Numbers Greater Than 1*, J. Energy Eng. **147**, 04020077 (2021).

[150] J. W. J. Kaiser, D. Appel, F. Fritz, S. Adami, and N. A. Adams, *A Multiresolution Local-Timestepping Scheme for Particle–Laden Multiphase Flow Simulations Using a Level-Set and Point-Particle Approach*, Comput. Methods Appl. Mech. Eng. **384**, 113966 (2021).

[151] C. H. Chang, X. Deng, and T. G. Theofanous, *Direct Numerical Simulation of Interfacial Instabilities: A Consistent, Conservative, All-Speed, Sharp-Interface Method*, J. Comput. Phys. **242**, 946 (2013).

[152] B. Dorschner, L. Biasiori-Poulanges, K. Schmidmayer, H. El-Rabii, and T. Colonius, *On the Formation and Recurrent Shedding of Ligaments in Droplet Aerobreakup*, J. Fluid Mech. **904**, (2020).

[153] M. Jalaal and K. Mehravaran, *Fragmentation of Falling Liquid Droplets in Bag Breakup Mode*, Int. J. Multiph. Flow **47**, 115 (2012).

[154] M. Jain, R. S. Prakash, G. Tomar, and R. V. Ravikrishna, *Secondary Breakup of a Drop at Moderate Weber Numbers*, Proc. R. Soc. A Math. Phys. Eng. Sci. **471**, 20140930 (2015).

[155] G. Nykteri, P. Koukouvinis, R. S. Gonzalez Avila, C.-D. Ohl, and M. Gavaises, *A Σ-Y Two-Fluid Model with Dynamic Local Topology Detection : Application to High-Speed Droplet Impact*, J. Comput. Phys. **408**, 109225 (2020).

[156] N. Bremond and E. Villermaux, *Bursting Thin Liquid Films*, J. Fluid Mech. **524**, 121 (2005).

[157] X. K. Cao, Z. G. Sun, W. F. Li, H. F. Liu, and Z. H. Yu, *A New Breakup Regime of Liquid Drops Identified in a Continuous and Uniform Air Jet Flow*, Phys. Fluids **19**, 057103 (2007).

[158] D. Stefanitsis, I. Malgarinos, G. Strotos, N. Nikolopoulos, E. Kakaras, and M. Gavaises, *Numerical Investigation of the Aerodynamic Breakup of Diesel and Heavy Fuel Oil Droplets*, Int. J. Heat Fluid Flow **68**, 203 (2017).

[159] S. Karthika, T. K. Radhakrishnan, and P. Kalaichelvi, *A Review of Classical and Nonclassical Nucleation Theories*, Cryst. Growth Des. **16**, 6663 (2016).

[160] W. E. Ranz and W. R. Marshall, *Evaporation from Drops - Part 1*, Chemical Engineering Progress.

[161] B. Duret, J. Reveillon, T. Menard, and F. X. Demoulin, *Improving Primary Atomization Modeling through DNS of Two-Phase Flows*, Int. J. Multiph. Flow **55**, 130 (2013).

[162] T. F. Leung, C. P. Groth, and J. Hu, *Evaluation of an Eulerian-Lagrangian Spray Atomization (ELSA) Model for Nozzle Flow: Modeling of Coupling Between Dense and Disperse Regions*, in *47th AIAA Thermophysics Conference* (2017), p. 4352.

[163] S. Fujioka, M. Shimomura, Y. Shimada, S. Maeda, H. Sakaguchi, Y. Nakai, T. Aota, H. Nishimura, N. Ozaki, A. Sunahara, K. Nishihara, N. Miyanaga, Y. Izawa, and K. Mima, *Pure-Tin Microdroplets Irradiated with Double Laser Pulses for Efficient and Minimum-Mass Extreme-Ultraviolet Light Source Production*, Appl. Phys. Lett. **92**, 241502 (2008).

[164] H. Mizoguchi, T. Abe, Y. Watanabe, T. Ishihara, T. Ohta, T. Hori, T. Yanagida, H. Nagano, T. Yabu, S. Nagai, G. Soumagne, A. Kurosu, K. M. Nowak, T. Suganuma, M. Moriya, K. Kakizaki, A. Sumitani, H. Kameda, H. Nakarai, and J. Fujimoto, *100W 1st Generation Laser-Produced Plasma Light Source System for HVM EUV Lithography*, in *Extreme Ultraviolet (EUV) Lithography II. International Society for Optics and Photonics*, Vol. 7969 (2011), p. 796908.

[165] V. Y. Banine, K. N. Koshelev, and G. H. P. M. Swinkels, *Physical Processes in EUV Sources for Microlithography*, J. Phys. D. Appl. Phys. **44**, 253001 (2011).

[166] A. Pirati, J. van Schoot, K. Troost, R. van Ballegoij, P. Krabbendam, J. Stoeldraijer, E.

Loopstra, J. Benschop, J. Finders, H. Meiling, E. van Setten, N. Mika, J. Dredonx, U. Stamm, B. Kneer, B. Thuering, W. Kaiser, T. Heil, and S. Migura, *The Future of EUV Lithography: Enabling Moore's Law in the next Decade*, in *Extreme Ultraviolet (EUV) Lithography VIII*, Vol. 10143 (2017), p. 101430G.

[167] N. Bloembergen, *Brief History of Laser-Induced Breakdown*, in *Laser-Induced Damage in Optical Materials: 1998*, Vol. 3578 (International Society for Optics and Photonics, 1999), pp. 198–200.

[168] E. M. Gattass, Rafael R., *Femtosecond Laser Micromachining in Transparent Materials*, Nat. Photonics **2**, 219 (2008).

[169] G. Della Valle, R. Osellame, and P. Laporta, *Micromachining of Photonic Devices by Femtosecond Laser Pulses*, J. Opt. A Pure Appl. Opt. **11**, (2009).

[170] M. M. Krasnov, *Laser-Phakopuncture in the Treatment of Soft Cataracts*, Br. J. Ophthalmol. **59**, 96 (1975).

[171] J. T. Walsh, *Pulsed Laser Angioplasty: A Paradigm for Tissue Ablation*, in *Optical-Thermal Response of Laser-Irradiated Tissue* (1995), pp. 865–902.

[172] A. Vogel and V. Venugopalan, *Mechanisms of Pulsed Laser Ablation of Biological Tissues*, Chem. Rev. **103**, 577 (2003).

[173] I. Apitz and A. Vogel, *Material Ejection in Nanosecond Er:YAG Laser Ablation of Water, Liver, and Skin*, Appl. Phys. A Mater. Sci. Process. **81**, 329 (2005).

[174] S. R. G. Avila and C. D. Ohl, *Fragmentation of Acoustically Levitating Droplets by Laser-Induced Cavitation Bubbles*, J. Fluid Mech. **805**, 551 (2016).

[175] M. S. Krivokorytov, Q. Zeng, B. V. Lakatosh, A. Y. Vinokhodov, Y. Y. Sidelnikov, V. O. Kompanets, V. M. Krivtsun, K. N. Koshelev, C. D. Ohl, and V. V. Medvedev, *Shaping and Controlled Fragmentation of Liquid Metal Droplets through Cavitation*, Sci. Rep. **8**, 1 (2018).

[176] P. Kafalas and J. Herrmann, *Dynamics and Energetics of the Explosive Vaporization of Fog Droplets by a 106-Mm Laser Pulse*, Appl. Opt. **12**, 772 (1973).

[177] P. Kafalas and A. P. Ferdinand, *Fog Droplet Vaporization and Fragmentation by a 106-Mm Laser Pulse*, Appl. Opt. **12**, 29 (1973).

[178] V. Prasad Sandireddy, K. Prasad Koirala, G. Duscher, and R. Kalyanaraman, *Explosive*

*Vaporization of Metallic Nanostructures on a Surface by Nanosecond Laser Heating under Fluids*, J. Appl. Phys. **129**, 064901 (2021).

[179] J.-Z. Zhang, J. K. Lam, C. F. Wood, B.-T. Chu, and R. K. Chang, *Explosive Vaporization of a Large Transparent Droplet Irradiated by a High Intensity Laser*, Appl. Opt. **26**, 4731 (1987).

[180] D. Kurilovich, A. L. Klein, F. Torretti, A. Lassise, R. Hoekstra, W. Ubachs, H. Gelderblom, and O. O. Versolato, *Plasma Propulsion of a Metallic Microdroplet and Its Deformation upon Laser Impact*, Phys. Rev. Appl. **6**, (2016).

[181] R. G. Pinnick, A. Biswas, R. L. Armstrong, S. G. Jennings, J. D. Pendleton, and G. Fernández, *Micron-Sized Droplets Irradiated with a Pulsed CO_2 Laser: Measurement of Explosion and Breakdown Thresholds*, Appl. Opt. **29**, 918 (1990).

[182] M. M. Basko, M. S. Krivokorytov, A. Yu Vinokhodov, Y. V. Sidelnikov, V. M. Krivtsun, V. V. Medvedev, D. A. Kim, V. O. Kompanets, A. A. Lash, and K. N. Koshelev, *Fragmentation Dynamics of Liquid-Metal Droplets under Ultra-Short Laser Pulses*, Laser Phys. Lett. **14**, 36001 (2017).

[183] S. Y. Grigoryev, B. V. Lakatosh, M. S. Krivokorytov, V. V. Zhakhovsky, S. A. Dyachkov, D. K. Ilnitsky, K. P. Migdal, N. A. Inogamov, A. Y. Vinokhodov, V. O. Kompanets, Y. V. Sidelnikov, V. M. Krivtsun, K. N. Koshelev, and V. V. Medvedev, *Expansion and Fragmentation of a Liquid-Metal Droplet by a Short Laser Pulse*, Phys. Rev. Appl. **10**, 064009 (2018).

[184] Q. Zeng, S. R. Gonzalez-Avila, S. Ten Voorde, and C.-D. Ohl, *Jetting of Viscous Droplets from Cavitation-Induced Rayleigh–Taylor Instability*, J. Fluid Mech. **846**, 916 (2018).

[185] A. L. Klein, W. Bouwhuis, C. W. Visser, H. Lhuissier, C. Sun, J. H. Snoeijer, E. Villermaux, D. Lohse, and H. Gelderblom, *Drop Shaping by Laser-Pulse Impact*, Phys. Rev. Appl. **3**, 1 (2015).

[186] A. L. Klein, D. Lohse, M. Versluis, and H. Gelderblom, *Apparatus to Control and Visualize the Impact of a High-Energy Laser Pulse on a Liquid Target*, Rev. Sci. Instrum. **88**, (2017).

[187] D. C. K. Rao, A. P. Singh, and S. Basu, *Laser Pulse-Droplet Interaction Enables the Deformation and Fragmentation of Droplet Array*, (2021).

[188] P. Koukouvinis, N. Kyriazis, and M. Gavaises, *Smoothed Particle Hydrodynamics Simulation of a Laser Pulse Impact onto a Liquid Metal Droplet*, PLoS One **13**, 1 (2018).

[189] G. Tretola and K. Vogiatzaki, *Numerical Treatment of the Interface in Two Phase Flows Using a Compressible Framework in OpenFOAM: Demonstration on a High Velocity Droplet Impact Case*, Fluids **6**, 78 (2021).

[190] H. Gelderblom, H. Lhuissier, A. L. Klein, W. Bouwhuis, D. Lohse, E. Villermaux, and J. H. Snoeijer, *Drop Deformation by Laser-Pulse Impact*, J. Fluid Mech. **794**, 676 (2016).

[191] S. A. Reijers, J. H. Snoeijer, and H. Gelderblom, *Droplet Deformation by Short Laser-Induced Pressure Pulses*, J. Fluid Mech. **828**, 374 (2017).

[192] M. J. Cooker and D. H. Peregrine, *Pressure-Impulse Theory for Liquid Impact Problems*, J. Fluid Mech. **297**, 193 (1995).

[193] A. Antkowiak, N. Bremond, S. Le Dizès, and E. Villermaux, *Short-Term Dynamics of a Density Interface Following an Impact*, J. Fluid Mech. **577**, 241 (2007).

[194] T. B. Anderson and R. Jackson, *Fluid Mechanical Description of Fluidized Beds: Equations of Motion*, Ind. Eng. Chem. Fundam. **6**, 527 (1967).

[195] N. G. Deen, M. Van Sint Annaland, M. A. Van der Hoef, and J. A. M. Kuipers, *Review of Discrete Particle Modeling of Fluidized Beds*, Chem. Eng. Sci. **62**, 28 (2007).

[196] A. R. Clark, *Medical Aerosol Inhalers: Past, Present, and Future*, Aerosol Sci. Technol. **22**, 374 (1995).

[197] N. Kyriazis, P. Koukouvinis, and M. Gavaises, *Numerical Investigation of Bubble Dynamics Using Tabulated Data*, Int. J. Multiph. Flow **93**, 158 (2017).

[198] A. Vidal, P. Koukouvinis, and M. Gavaises, *Vapor-Liquid Equilibrium Calculations at Specified Composition, Density and Temperature with the Perturbed Chain Statistical Associating Fluid Theory (PC-SAFT) Equation of State*, Fluid Phase Equilib. **521**, (2020).

[199] M. G. Mithun, P. Koukouvinis, and M. Gavaises, *Numerical Simulation of Cavitation and Atomization Using a Fully Compressible Three-Phase Model*, Phys. Rev. Fluids **3**, 064304 (2018).

[200] P. Koukouvinis, C. Rodriguez, J. Hwang, I. Karathanassis, M. Gavaises, and L. Pickett, *Machine Learning and Transcritical Sprays: A Demonstration Study of Their Potential in ECN Spray-A*, Int. J. Engine Res. (2021).

[201] C. Diddens, H. Tan, P. Lv, M. Versluis, J. G. M. Kuerten, X. Zhang, and D. Lohse, *Evaporating Pure, Binary and Ternary Droplets: Thermal Effects and Axial Symmetry Breaking*, J. Fluid Mech. **823**, 470 (2017).